Synthesis and Functionalization of Second Harmonic Generation Nanocrystals and Their Application in Biological Imaging

Thesis by

Jelena Culic-Viskota

In Partial Fulfillment of the Requirements

for the Degree of

Doctor of Philosophy

California Institute of Technology

Pasadena, California

2012

(Defended May 9, 2012)

To my parents, Vera and Lovre,

and my sister Jasna for their undying love and support.

Acknowledgments

I would like to thank my advisers: Dr.Mark E. Davis, Dr.Scott E. Fraser and Dr.Richard C. Flagan for their support and guidance during my time at Caltech. I am very grateful for all the assistance I received when I needed advice and for the understanding they have had for me. I am very honored to have worked in the Davis and Fraser labs and to have gained new skills and learned how to approach and solve problems more effectively. I owe my deepest gratitude to Dr.Periklis Pantazis for introducing me to Second Harmonic Generation and for his advice and help through the years. It was a pleasure to learn from Dr.Pantazis and be influenced by his enthusiasm and passion for science.

I am indebted to many of my colleagues for their assistance and support: Yashodan Bhawe, Chris Alabi, Devin Wiley, Leonard Medrano, and Han Han in the Davis lab for advice and sharing their reagents with me, and most of all William (Bill) Dempsey in the Fraser lab. Bill has worked tirelessly on analyzing the samples for SHG signal, was responsible for their biological application in zebrafish and for SHG data processing and generating many of the images and movies in this dissertation. I am indebted to him for his kindness, his assistance, and support. It was a true pleasure to work with him on this collaborative effort and a joy to get to know him on a more personal level. I would also like to thank Dr.Karn Sorasaenee and Carl Blumenfeld for their collaboration with the corrole functionalization of barium titanate. Dr. Sorasaenee and Carl provided me with the corroles, and I am very pleased to have had the opportunity to work with them. I am very thankful to Carol Garland for teaching me everything I know about TEM and for being a wonderful

and supportive mentor over the years, and for her understanding and willingness to meet me half-way on more than one occasion. I am thankful to Frank Troung and Dr.Janek Szychowski in Dr.Tirell's lab for their advice regarding click chemistry and the provision of the chemicals needed. I have been very fortunate to work with amazing people and scientists, and their unselfish generosity will always keep Caltech in my fondest memories.

In addition, I am also very grateful for all the amazing friends and colleagues that I have made at Caltech. These last five years would not have been nearly as educational or fun without your friendship. I am especially thankful to Rosemary Rodhe, Rosalyn Sayaman, and Tammy Campbell. Your love and support has been instrumental for me in my times of need, and I am grateful to have you as my closest friends. I would like to thank Vedran Coralic, Dubravka Pezic, Slobodan Mitrovic, and Ivan Vlahinich for making home feel a little bit closer. In addition, I want to thank all of my salsa friends who have shared my passion for dancing and the dance stage: Indira Wu, David Young, Dan Bower and Danielle Bower, Paulo Younse, Jasper Chan, and Vanessa Heckman. I would also like to thank many of my friends who have served with me on the Graduate Student Council. It has been a wonderful experience working with you to serve the needs of Caltech students and Caltech community at large.

I would also like to thank Martha Hepworth, Kathy Bubash, and Karen Baumgartner for their help and speedy resolution to any problem I have had over the years. I owe my deepest gratitude to Suresh Guptha, who has on many occasions saved my laptop, and without his help this dissertation would not have even been possible to write. I would also like to extend many thanks to the wonderful staff at the Caltech Health Center, especially Alice and Divina, for being always supportive and helpful with problems ranging from sinusitis to chicken pox.

But most of all, I would like to express my deepest gratitude to my parents, Vera and Lovre, and my sister Jasna. They have always been supportive of me and my efforts. Without their love and understanding, the roads I have taken over the years would not be nearly as pleasant.

Abstract

The discovery and use of fluorescent proteins has been of extreme importance in biological imaging of cells, tissues, and organs. In order to address some of the limitations of fluorescent tags, second harmonic generation can be used. Second harmonic generating nanoprobes allow nontoxic, long-term imaging that, with proper functionalization, can be utilized for biological imaging applications. As a proof of principle, commercial tetragonal barium titanate nanoparticles were functionalized to expose surface amine groups, which could be further modified for a plethora of biological applications. Barium titanate nanoparticles were functionalized for selective targeting of tissue sections, biorthogonal linkages and for nonspecific long-term imaging using biocompatible polymers enabling the study of cells as they differentiate during zebrafish development. Since the commercial barium titanate nanoparticles do not have a narrow size distribution, which limits the application of such nanoprobes, synthesis of monodisperse nanocrystals was attempted.

Zinc oxide nanocrystals were synthesized by solvothermal methods involving the base hydrolysis of zinc salts in the presence of capping ligands. Different synthesis procedures were investigated based on the properties of the prepared nanoparticles. To prevent nanoparticle aggregation and to achieve good dispersion, a capping agent was chosen that provides a tightly bound shell around the nanoparticles. It was observed that the polymerization of PEG molecules with the organic ligands bound to the surface of zinc oxide provided the most adequate coating for the desired size control and dispersion of the nanocrystals. Exploration of the experimental conditions enabled production of variable size hexagonal zinc oxide nanocrystals, which can be

used both as SHG probes and as quantum dots.

Contents

List of Figures

Chapter 1

Introduction

1.1 Biological Imaging Challenges

In order to gain a better understanding of the organization of biological structures and mechanisms that govern them at cellular and subcellular levels, we resort to microscopy. Ideally, we need to visualize the biological specimen in its native physiological state which can be done by *in vivo* imaging. To image an object in the microscope, illumination radiation interacts with the specimen in order to generate contrast and produce two-dimensional images. The various imaging technologies differ in five main aspects: resolution, penetration depth, energy expended for image generation (ionizing vs. nonionizing), availability of injectable, biocompatible molecular probes, and the detection threshold for a given technology [1, 2]. Among the variety of noninvasive imaging approaches, biological sample imaging, both *in vivo* and *in vitro*, has relied on light microscopy with fluorescence microscopy emerging as one of the most powerful imaging techniques [3].

In fluorescence microscopy, fluorescent probes are used for the purpose of contrast enhancement. One of the major benefits of fluorescence imaging is the availability of a large variety of imaging contrast agents, some of which are endogenous (e.g., keratin, elastin, retinol, etc.) while others are exogenous (e.g., fluorescein, rhodamin, AlexaFluor dyes, quantum dots, etc.). The plethora of biocompatible, commercially available fluorescent probes enables tuning of the penetration depth, and signal in-

tensity, as well as the method of introduction into the organism. Some fluorescent probes are genetically encodable (e.g., green fluorescent protein (GFP) and its varieties, etc.), while others need to be injected into or uptaken by the organism (e.g., inorganic dyes, quantum dots, etc.). In addition to aiding visualization, functional fluorescent probes provide dynamic information regarding localization and quantity of target molecules [4]. This enables *in vivo* fluorescence imaging to have many application, one of which is in the cancer detection: utilized in identification of tumor boundaries (aiding the efficiency of cancer treatment), assessment of blood and lymph vessels, and monitoring treatment progress [5]. It can also aid in the understanding of an organisms' development through different stages and in detection of any malformations during that time. Fluorescent probes can also be used as sensors to measure the concentration of calcium, hydrogen, and other ions and molecules along with the detection of membrane voltages [6, 7].

However, *in vivo* imaging of biological samples is technically a very challenging task due to mainly two reasons. Thick and opaque tissue samples tend to absorb and scatter photons and generate strong autofluorescence, which decreases the signal-to-noise ratio (SNR) and makes it difficult to detect and quantify the desired signal. Secondly, imaging in biological environments requires the imaging agent to be stable, biocompatible, and to accumulate with specificity at the desired target position [8].

One way to address the fundamental barriers of tissue imaging, mainly absorption and scattering of photons by the tissue, is to utilize low energy near infrared (NIR) light sources. As photons travel through the tissue and interact with it, their trajectories will depend on the tissue absorptivity and its scattering properties [9, 1]. The total light absorption will be proportional to the absorption coefficients and the molar concentration of all the components of the tissue. As photons are absorbed, there is a possibility that they would be emitted as fluorescent light in a process called autofluorescence. Unwanted autofluorescence lowers the SNR and can be avoided with the use of filters or careful selection of excitation wavelength. In most tissues the major absorbers are water and hemoglobin [10], with the lowest absorptions observed in the 650-900 nm region (see figure 1.1) [3, 1]. Therefore, photon absorption can be

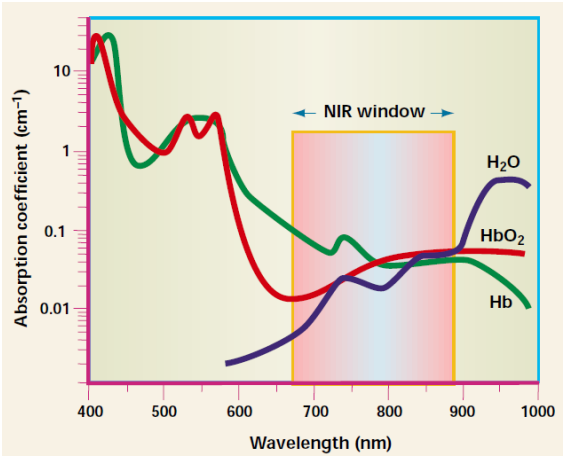

Figure 1.1: Absorbance of most common tissue absorbers, hemoglobin (Hb), oxygenated hemoglobin (HbO_2) and water, as a function of excitation wavelength. Selecting excitation wavelengths in the NIR range is beneficial, as the absorption of tissue is at a minimum from 650 to 900 nm [1]. The deepest penetration inside the tissue with minimal effects on the organism can be achieved utilizing NIR light and as such is desirable for biological imaging purposes. (The source of this image is [1].)

minimized utilizing low-energy light sources within the NIR region; leading to longer tissue penetration depth, on the order of centimeters [1].

In addition to photon absorption, photon scattering disrupts tissue imaging. The size of the tissue or cellular components with respect to the wavelength of light, and the refractive index difference between the scattering particle and the medium determine the scattering properties [11]. In the NIR region, cellular components have dimensions similar to the incoming wavelength of light, and their refractive indices are similar, thus NIR light will be mostly forward-directed, enabling deeper tissue penetration [2, 11].

Therefore, useful *in vivo* imaging probes should interact with low energy NIR light to ensure deeper penetration length, as well as minimal deleterious effects on both the imaging probe and the surrounding organism. In addition, the probe itself should be stable in the cellular environment and elicit no immunological response by the organism. To ensure that the probe is biocompatible and also has the appropriate functionality, the imaging probe can be coated with ligands that impart the desired effects. In the following sections, the most commonly used imaging probes will be

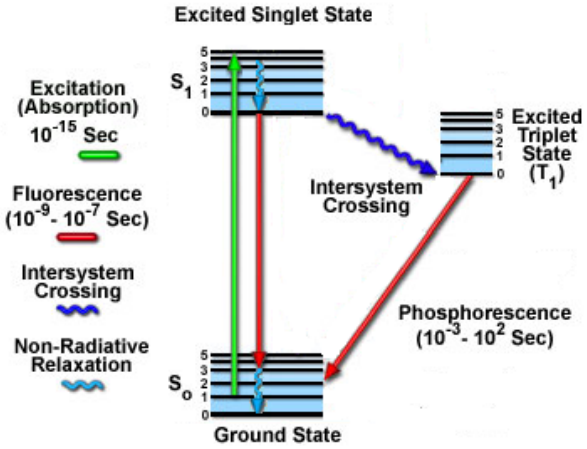

Figure 1.2: Jablonski energy diagram illustrating the electronic states of a molecule and the transitions between them. During fluorescence, the fluorophore absorbs photons exciting the electrons to an excited singlet state, and during the relaxation process to the ground state, there is a lower energy emission of photons due to nonradiative relaxation. Sometimes the electrons transit to the triplet excited state and emit photons in a process called phosphorescence.

described in more detail, starting with fluorescent probes.

1.2 Fluorescent Probes

Fluorescent probes (fluorophores) are compounds that exhibit fluorescence, which is a form of luminescence where the absorption of photons by the fluorophore excites its electrons into a higher energy state (excited state), followed by a nearly immediate emission of light (on the timescale of 10^{-8} s) [12]. For a transition to occur, the absorbed energy must be equivalent to the difference between the electronic ground state and the excited state. The amount of energy absorbed is characteristic for every fluorophore and is called the excitation wavelength. During the relaxation of the excited molecule back to the ground state, the emitted light has less energy than the absorbed light, as some energy is lost to nonradiative relaxation (see figure 1.2).

The amount of energy emitted is also characteristic to the fluorescent probe and is called the emission wavelength. The difference in the wavelengths of the excited and the emitted light is called the Stoke's shift. A large Stoke's shift enables easier separation of the excitation and emission bands, and it determines the efficiency of

the emission signal collection. Brightness of the emitted signal also enables easier signal collection, and it is a product of the quantum yield (Φ) and the absorption coefficient (ε) characteristic to the fluorophore. Quantum yield is the ratio of fluorescence emission to the total excitation and it enables the maximum intensity of the fluorophore to be calculated.

Another important feature of a fluorescent probe is its lifetime. Fluorescent lifetime is an intrinsic property of the fluorophore and is defined as the length of time between the photon absorption and the subsequent photon emission (on the order of nanoseconds). Ideally, the fluorescent probe used for imaging has a high quantum yield, large absorption coefficient, and large Stoke's shift with narrow emission spectra in order to easily filter the desired fluorescent signal from the background and increase SNR.

There are fundamentally two modes of excitation of a fluorescent probe: one-photon excitation, requiring typically higher energy photons (200-500 nm range) or two-photon excitation, utilizing lower energy photons (NIR range). Two-photon excitation is a nonlinear process where two photons are simultaneously absorbed by the fluorophore (see figure 1.3a), and the probability of two-photon absorption (2PA) by a fluorescent molecule has a squared dependence on the excitation light intensity. For a spatially uniform specimen undergoing one-photon excitation, fluorescent signals are generated equally from each z-section above and below the focal plane [13]. In contrast, using two-photon excitation the fluorescence signal is confined to a femtoliter focal volume where the photon flux is maximal [13] as seen in figure 1.3b. Fluorescence excited outside the focal point volume is negligible in two-photon excitation mode, as it falls off rapidly away from the focal volume. This property of two-photon excitation enables generation of three-dimensional (3D) images without the use of pinholes, by repeated scanning of the sample along the z-axis. In addition, since a pulsed NIR laser source is used for two-photon excited fluorescence, it reduces photodamage to the living specimen and enables deeper penetration, as mentioned before (section 1.1). However, the biggest advantage of two-photon excitation is that it enables high-sensitivity imaging by eliminating contamination from the fluorescent

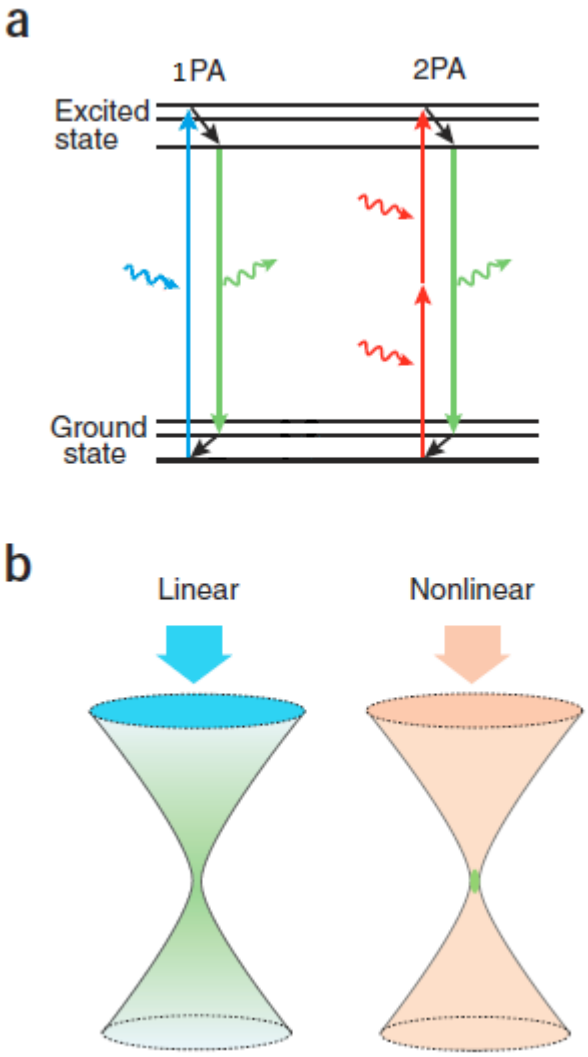

Figure 1.3: (a) Jablonski energy diagram, illustrating one-photon absorption (1PA), and two-photon absorption (2PA) with subsequent emission of photons. Energy of the emitted light (green) is lower than the energy of the excitation light (blue, red) due to the nonradiative relaxation (black). (b) Spatial confinement of signal generation with linear and nonlinear excitation. Visible ("blueish") light is usually used for excitation in one-photon excited fluorescence, whereas near-infrared ("redish") light is used in two-photon excited fluorescence. Fluorescent light (green) in one-photon microscopy is equally generated from the whole volume, whereas nonlinear signal production in 2PA is localized to the focal volume [11]. (The image is a modified version from a figure in [11].)

light outside the focal plane [13].

Regardless of the mode of excitation, most commonly used fluorescent probes can be divided into three categories: organic dyes, biological fluorophores, and quantum dots. Organic fluorophores are some of the most commonly used fluorescent probes and have first been applied in living cell imaging in the early 1900s [12]. They are synthetic dyes whose optical properties are a function of their structure and can be attributed to either an optical transition localized over the whole fluorophore (general resonant transition) or to intramolecular charge transfer transitions [14]. A wide variety of organic fluorophores have been synthesized and are small, cheap, and commercially available dyes with different functionalizations ready for bioconjugation to desired biological targets using established protocols [14, 15]. In general resonant transition, fluorescent probes have narrow absorption and asymmetric emission bands, high absorption coefficients and moderate to high quantum yields in the visible range, but small, solvent insensitive Stoke's shifts. On the other hand, charge transfer transition fluorescent probes have well-separated broad absorption and emission bands, but small absorption coefficients and quantum yields. Unfortunately, most of the organic dyes in the NIR range have lower fluorescence lifetime (1 ns vs. 5 ns in visible range), limited photostability, poor thermal stability and lower quantum yields (up to 25%), as is the case with the only NIR fluorophore approved for clinical use, indocyanine green (ICG) [14, 7].

Biological fluorophores are fluorescent proteins that take advantage of the same photophysics as organic dyes but are produced by cells via a cascade of DNA encoded processes leading ultimately to fluorophore formation [7]. Similar to synthetic dyes, there is a variety of fluorescent proteins that are commercially available, differing by their spectral properties [16]. In comparison, fluorescent proteins have the advantage of being genetically encodable in the organism and have the potential to be expressed at specific locations and times during the organism's development. This allows for minimal disruption of the organism, while enabling good visualization of target structures. Only a handful of fluorescent proteins are excited by NIR light, and in general they have low quantum yields in the NIR range [17, 18, 16].

The choice of organic dyes over fluorescent proteins is dependent on the imaging needs of a particular study. Both can be selectively excited and have high sensitivity enabling detection of a small number of targets. In addition, they can be used for spectral multiplexing, utilizing different fluorophores that exhibit different emission wavelengths when excited by a single light source. However, due to the nature of the excitation and emission spectra, the number and characteristics of the fluorophores used for spectral multiplexing are limited [14]. This is mainly because the narrow excitation spectra, which requires excitation by light of a specific wavelength, as well as the broad emission spectra, result in the spectra of different dyes having overlap to a large extent. This limits the number of fluorescent probes that may be used to tag different biological molecules and be spectrally resolved simultaneously. In addition, other limitations that fluorescent probes exhibit are dye saturation, bleaching and blinking.

Dye saturation is a phenomenon which occurs when the illumination of the excitation light is so intense that at any time point, a significant fraction of the fluorophores are excited to the higher energy state. As the emission of the photon is delayed by the fluorescent lifetime of the fluorophore, the effective number of the fluorescent probes that are excitable is effectively decreased [19, 20].

Dye bleaching encompasses all the processes that cause the fluorescent signal to fade permanently and are due to the permanent photon-induced chemical damage to the fluorophore [20]. There are a variety of ways that bleaching can take place, with the most common method being associated with the relatively long-lived triplet state (figure 1.2). When the excited fluorophore transits from the singlet to the triplet excited state and interacts with present molecular oxygen, it can transfer some of its energy, exciting the oxygen to its singlet excited state (forming an reactive oxygen species—a free radical). Free radicals can permanently destroy the fluorophore by bleaching it. In addition, the free radicals can interact with other organic molecules present in the cells or tissue, forming phototoxic by-products [6, 20].

Blinking (or fluorescence intermittency) is a phenomenon when a fluorophore alternates between bright ("on") to dark ("off") states under continuous illumination.

Dye saturation and blinking decrease the SNR as the effective concentration of fluorophores at any point in time is decreased, while fluorophore bleaching limits the imaging time and such fluorophores are not suitable for long-term imaging [20, 21].

1.3 Quantum Dots

In order to address the shortcomings of organic dyes and biological fluorophores, quantum dots (QDs) are used [3, 22]. They were first utilized as biological probes in 1998 [23] and are now the most frequently used nanocrystal labels in bio-analysis and medical diagnostics [14]. Quantum dots are colloidal semiconductor nanocrystals ranging in size from 1 to 10 nm and consisting of hundreds to thousands of atoms [14, 24]. Their small size is consistent with the size of macromolecules and cell structures and is therefore of interest in biological imaging. Quantum dots generate fluorescence when photons strike the semiconductor material, exciting the electron from the valence band into the conduction band, leaving a hole in the valence band. The hole and the excited electron recombine, emitting a photon with the energy equal to that of the exciton (hole-electron pair). Since the energetic barrier between the valence and the conduction band increases as the quantum dot gets smaller in size (due to the quantum confinement effect), so does the energy of the emitted photons. Therefore a variety of emission wavelengths are exhibited by the same material dependent on the size of the QDs as seen in figure 1.4.

In general, quantum dots, photophysical properties are dependent on their size, composition, dispersity and surface chemistry [14]. In addition to the size and composition (as shown in figure 1.4), the emission wavelength of QDs is determined by their polydispersity. As quantum dots are a collection of nanocrystals with slight variations in size and shape, the emission spectrum is the sum of all of the individual nanocrystal emission spectra, with the width of the emission spectra dependent on the quantum dots polydispersity. In general, QDs have narrow emission with full width at half maximum of 20-35 nm [25]. Quantum dots absorb light of all wave-

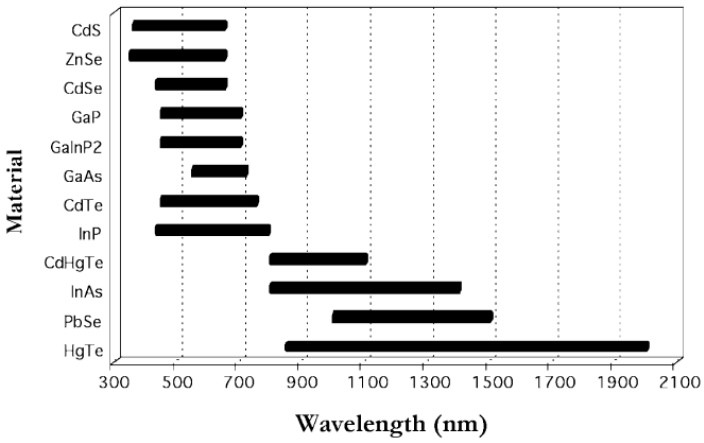

Figure 1.4: Range of quantum dot emission wavelengths is dependent on the material composition and the size [25]. Each of the bands represent the total range of narrow emissions that a QD of a particular composition can be tuned to emit, with careful size control. The wide range of emission wavelengths for different QDs enables spectral multiplexing, and the detection and separation of emitted signals is made easier due to the narrow emission bands for most quantum dots. (The source of the image is [25].)

lengths lower than the emission wavelength with varying degrees of efficiency. This broad excitation, coupled with their narrow and symmetric emission spectra allow the same light source to be used to obtain and distinguish between a variety of signals from different sized QDs- allowing for easier spectral multiplexing with a single light source. In addition, their longer fluorescence lifetime, on the order of tens of nanoseconds, can be utilized in background autofluorescence exclusion [7]. One of the most prominent features of quantum dots are their high quantum yields, even in the NIR range (up to 70%), and high molar absorption coefficients (on the order of 4 times greater than those for organic fluorescent probes) leading to very high brightness and increased SNR [14], enabling their use in *in vivo* imaging with greater penetration depths as compared to organic fluorescent probes. In addition, quantum dots have very good photo- and thermal stability as they can be kept under intense illumination up to hours without loss of signal brightness [24] and due to their large two-photon cross section they can be used in two-photon excited microscopy [25]. The stability of quantum dots is influenced by the core surface passivation [14]: through shell and ligand coatings.

Ligand coating of QDs is of extreme importance in biological solutions as it helps stabilization, solubilization in desired solvent, and provides desired biocompatible functionality for either targeting desired structures or reduction of nonspecific adsorption [24]. Quantum dots can be divided into four different groups based on their properties: core, core-shell, water soluble and bioconjugated QDs. Core QDs are composed only of the semiconductor nanocrystals ("core") that determines the optical properties of the quantum dot. Core QDs are hydrophobic and have limited stability and low quantum yields due to the surface defects in the crystal structure that act as temporary ''traps'' for the electron or hole, preventing their radiative recombination [26, 27]. Core-shell quantum dots have a passivating shell of inorganic material that imparts these hydrophobic QDs greater photochemical stability and preserves their brightness [25, 27]. Water soluble quantum dots are polymer-coated core-shell QDs that enable the material to be dispersed in polar solvents, while the bioconjugated quantum dots are coated with ligands or polymers of interest for biological systems, like polyethylene glycol (PEG). The diverse functionality of quantum dots coupled with their enhanced photophysical properties enables them to be the probes of choice for the study of intracellular processes at the single-molecule level, high-resolution cellular imaging, long-term *in vivo* observation of cell trafficking, tumor targeting, and diagnostics [26, 28, 29].

However, quantum dots have similar limitations as do organic fluorescent probes. Even though, their inorganic shells provides greater photostability and resistance to photobleaching, the alternations between trapped an untrapped events result in intermittent fluorescence, which limits single-molecule level imaging. There have been advances made to address the quantum dot blinking, but they come at the expense of broader emission spectra [30, 20]. Since quantum dots absorb photons, their signal is saturable and SNR limiting. The most prominent limitation of quantum dots is their inherent toxicity due to the chemical composition of QDs [31], where heavy metals leach from the usually porous inorganic shell coating and remain a concern for chronic toxicity [31, 32]. Research on the toxicity of quantum dots is still underway, with some promising reported formulations of quantum dots designed for rapid renal clearance

that could minimize *in vivo* toxicity [33]. Ultimately, toxicity concerns would be best addressed with the development of nanocrystals that avoid the use of toxic metals and functionalization methods that enable rapid clearance from the organism.

1.4 Second Harmonic Generation Probes

Another powerful tool in biological imaging is the use of second harmonic generation (SHG), which addresses some of the limitations inherent to fluorescent materials. Second harmonic generation is a nonlinear process that relies on light scattering for contrast generation, as opposed to fluorescence which relies on light absorption. The theoretical groundwork explaining the process of two photon quantum transition was first postulated by Maria Göppert-Mayer in 1931 [34]. It took 30 years until Franken had made the first observation of SHG in a quartz crystal irradiated with a ruby laser [35], and the first biological application in imaging of collagen in rat-tail tendon was in 1986 [36]. SHG is a process where two identical photons of light interact with a noncentrosymmetric material (SHG probe), occupying briefly a virtual energy state and combining to produce a photon of exactly double the energy of incident photons (half the incident wavelength) before returning to the ground state, exhibiting anti-Stokes shift. To enable sufficient SHG signal production, the illumination of a highly ordered, noncentrosymmetric material by means of an intense, focused, and pulsed two-photon (2P) laser source is required. The optical response of the interaction of the SHG probe with the photons is specified by the induced polarization P(ω) as a power series expansion of the electric field strength E(ω):

$$P(\omega) = \chi^{(1)}E(\omega) + \chi^{(2)}E(\omega)^2 + \chi^{(3)}E(\omega)^3 + ...$$

where the coefficient $\chi^{(n)}$ is the n^{th} order susceptibility of the material. First-order susceptibility, $\chi^{(1)}$, corresponds to the linear optical responses of adsorption, scattering and reflection, $\chi^{(2)}$ and $\chi^{(3)}$ correspond respectively to second and third harmonic

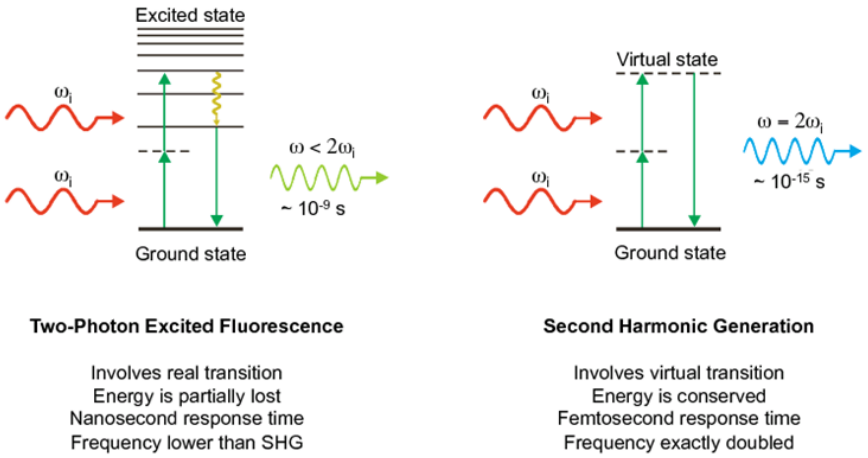

Figure 1.5: Energy diagrams describing the two-photon excited fluorescence and second harmonic generation processes respectively [21]. Both processes are dependent on the interaction of two photons with the material at the same time, but differ in the manner of the transition. SHG involves a virtual transition where the material is shortly excited to a virtual state, followed by a scatter of the combined photons of exactly double the input energy, effectively conserving the energy for radiative relaxation. In two-photon excited fluorescence, the transition involves excitation of the fluorophore electrons to an excited singlet state, followed by the emission of photons with the frequency lower than the sum of the input frequencies due to partial energy loss to nonradiative relaxation. (The source of this image is [21].)

generation. Only materials that have no inversion symmetry have a nonvanishing second-order susceptibility, $\chi^{(2)}$, the magnitude of which contributes to the brightness of the optical response. Therefore, SHG probes with large $\chi^{(2)}$, such as barium titanate, zinc oxide and silicon carbide [21], make good exogenous imaging probes producing bright SHG signal even at lower illumination intensities. SHG imaging has also been applied in the investigation of endogenous biological structures that are ordered noncentrosymmetrically such as collagen, microtubules, mitotic spindles, cellulose and actomyosin [36, 37, 21]. However, ideally the use of single tags to generate signal, as opposed to large biomolecular assemblies, is generally more applicable in imaging of tissues and cells and especially for single molecule detection.

The SHG process is similar to two-photon excited fluorescence (figure 1.5) as both require that two photons interact with the material at the same time. Therefore,

second harmonic generation has the same benefits of utilizing NIR light, which allows for deeper tissue penetration, and that the imaging is confined only to the focal volume where the light intensity is sufficiently high to generate signal with minimal photo- or thermal damage. However, unlike two-photon excited fluorescence, where some of the energy is partially lost to nonradiative processes, during the SHG process all the energy is conserved as the transition is virtual, which leads to enhanced photophysical properties. Namely, the SHG process does not suffer from dye saturation, bleaching and blinking problems as is the case with fluorescent probes, making SHG probes excellent tools for long-term imaging with enhanced and consistent SNR as compared to QDs or fluorescent probes. In addition, the femtosecond response time of the SHG process enables fast and sensitive detection. The narrow band of the SHG signal, with a full width half maximum on the order of 5 nm, enables easier separation and distinction between a multitude of signals, effectively increasing the SNR. Even though any SHG probe can be excited by a whole range of wavelengths of light, they all exhibit distinct intensity profiles, enabling spectral multiplexing by comparison of relative intensities [21] as demonstrated by Pantazis et al., in figure 1.6. The difference in the intensity profiles stems from the resonance enhancement of the material, when the input wavelength matches the difference between the excited and ground state of absorption for the material [20].

The exogenous SHG probes, similar to quantum dots, are not genetically encodable in the biological organism and have to be introduced into the system via injection or cellular uptake. Specific targeting of desired regions in the tissue or cell can be achieved by surface functionalization of SHG probes as demonstrated previously [21, 38, 39]. Unlike QDs, SHG probes have been shown to be nontoxic and noninterfering with the normal early development of zebrafish embryos when injected in during the most sensitive single cell stage [21]. The long-term stability of SHG probes, coupled with the square dependence of the SHG signal on the illumination intensity, enables detection of even the weakest probes by increasing the laser power. However, as the size of the SHG material decreases to the level comparable with the biological macromolecules, so does the SHG signal sensitivity. For such small

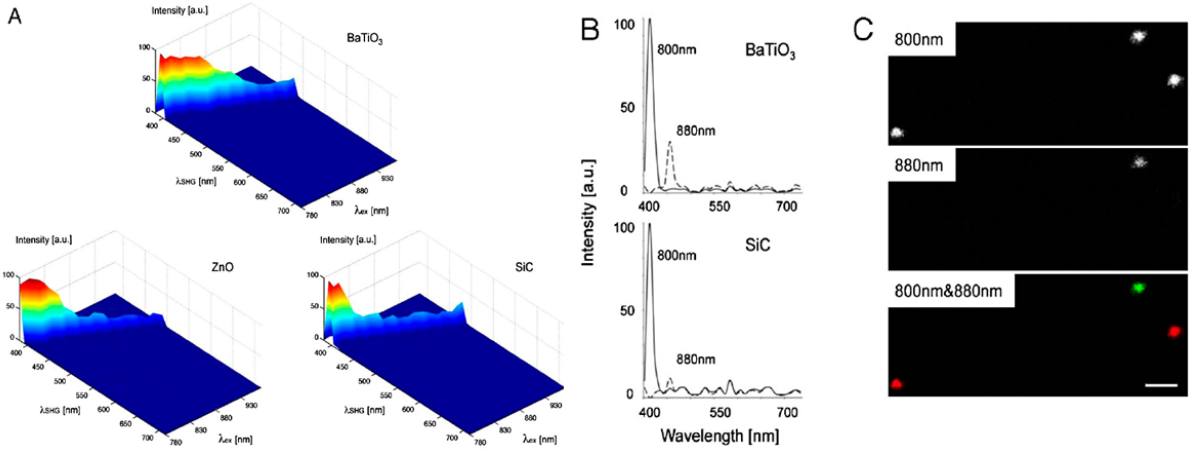

Figure 1.6: SHG intensity profiles of different exogenous SHG materials enable spectral multiplexing of SHG probes. (A) Displayed are the 3D normalized SHG signal data profiles of barium titanate ($BaTiO_3$), zinc oxide (ZnO), and silicon carbide (SiC) nanocrystals (signal ranging from 380 to 720 nm) generated by conventional two-photon excitation (excitation ranging from 760 to 970 nm). Note that the SHG signal peaks are always half the wavelength of the incident excitation wavelength. The difference in the intensity profiles stems from the resonance enhancement of the material when the input wavelength matches the difference between the excited and ground state of absorption for the material. Color code: dark blue corresponds to zero intensity and dark red corresponds to maximal intensity. (B and C) Multi-SHG imaging modality. (B) Displayed are the normalized SHG signal spectra of $BaTiO_3$ (upper) and SiC (lower) nanocrystals generated by tuning the excitation wavelength to 800 nm (solid line) and 880 nm (dashed line). (C) Single confocal sections showing comparable SHG signal intensities of immobilized $BaTiO_3$ and SiC nanocrystals in parallel. The noncentrosymmetric nanomaterials were sequentially excited with 800 nm (top) and 880 nm (middle), respectively. Whereas the SHG signal of SiC nanocrystals is only readily detectable at 800 nm, the SHG signal of $BaTiO_3$ nanocrystal is visible at both excitation wavelengths. Comparison of relative intensities is sufficient to distinguish different SHG nanoprobe materials (bottom, false-colored picture: SiC nanocrystals in red, $BaTiO_3$ nanocrystal in green). Scale bar: 500 nm. (The source of this image is [21].)

SHG probes, enhancements of the signal will likely be necessary to achieve detectable SHG, possibly by manipulating the resonance enhancement of the probe with specific surface coatings (e.g., with Au [40]).

In summary, the choice of an imaging probe and the process used by that probe is dependent on the experimental needs for a particular application, and the few presented here are by no means an exhaustive list. SHG probes, quantum dots and fluorescent probes differ in their photophysical properties, but are complementary to each other, offering interesting opportunities for multimodal spectral imaging. Ideally, for biological imaging applications the probe should be biocompatible, stable long-term, nontoxic and a strong signal emitter, which will allow for easier signal detection and separation from the background noise. The ability of NIR light to interact with a probe enables deeper penetration with minimal deleterious effects on the surrounding tissue. These probes can be used in a variety of applications and can be specifically targeted to structures of interest by different probe functionalizations.

1.5 Functionalization of Imaging Probes

In order for the inorganic imaging probes, such as quantum dots and SHG probes, to be utilized for biological imaging applications, they require proper surface functionalization. Particle surface interactions with the environment affect their stability and potentially their physicochemical properties. Therefore, by deliberate surface modifications the particles can be imparted stability and possibly targeting specificity [41]. Synthesis of nanoparticles usually involves stabilizing ligands that bind to the particle surface, stabilizing them from aggregation and aiding in the control of the growth rate and the morphology of the particle, which can be achieved by a addition of ligands with a greater affinity for a particular crystal facet of the nanoparticle. Preferential binding of ligands to the crystal facets that leads to a variety of geometrical shapes of the ZnO nanocrystals has been demonstrated [42].

However, the bonds between the inorganic nanoparticle surface and the ligand

end groups undergo dynamic binding and unbinding processes [43]. As a consequence of the unbinding of the surface ligands, by either extensive washing or competitive binding with another ligand exhibiting stronger binding affinity, the particle stability can be altered, resulting in aggregation of the nanoparticles. Therefore, the selection of the ligand molecule is dependent on the composition of the inorganic probe, its size, and the solvent it is dispersed in [44].

In aqueous solutions, strongly charged ligand molecules are found to stabilize the particles for a long time, but ligand molecules that provide steric stabilization to the nanoparticle are found to be much more resistant to high salt concentrations than electrostatically stabilized nanoparticles [45]. One example of such steric stabilization in aqueous solutions, which is commonly used for the application in biological samples, is the coating of nanoparticle surfaces with amphiphilic PEG polymer [46]. Owing to its chemical stability, PEG is an inert, biocompatible polymer which has numerous applications in medicine and biotechnology. PEGylation of nanoparticles improves their cytoplasmic transport by minimizing the attractive forces to cytoskeletal elements [47]. A variety of PEG reagents are commercially available, both monofunctional, with a methoxy group at the free end, of bifunctional varieties, which can be used for the introduction of desired functional groups to the particle surface.

Apart from surface coating with PEG polymers, other ligands that have been used in well establishes protocols [48] are DNA, RNA, proteins, lipids, vitamins, sugars and enzymes [44]. Conjugation of biomolecules to inorganic nanoparticles generates biocompatible hybrid materials, that allow the introduction of inorganic probes into the biological specimen with targeted specificity.

In addition, the surface of inorganic particles can be coated with silane reagents. Silanes are silicon compounds with functional or nonfunctional alkyl chains, and are applied for adhesion enhancement, improvement of particle dispersion, crosslinking, derivatization of functional groups, and modification of surface hydrophilicity [49]. Another common surface modification method is the use of click-chemistry, with the use of a spontaneously occurring chemical reaction with high yield and selectivity between the functional groups at mild conditions. These click reactions are most

commonly performed by reacting an azide with an alkyne [50].

Regardless of the functionalization method, all chemical surface modification schemes are dependent on the ligand shell or surface coating, and not on the actual inorganic core material [44]. Therefore, the surface of inorganic nanoparticles can be modified with a variety of ligands that impart nanoparticle stability by either electrostatic interaction or steric hindrance, as well as desired functionality. In addition, surfaces of nanoparticles can be coated with a number of functional groups, by varying the concentration of the coating ligands [51].

1.6 Research Objectives

The objectives of the research presented in this dissertation are twofold. First, in Chapter 2, the work that has been submitted for publication to Nature Protocols Journal and coauthored by W. Dempsey, Dr.P. Pantazis and Dr.S. Fraser on the novel functionalization pathways on commercial tetragonal barium titanate ($BaTiO_3$, referred to as BT) nanocrystals for use in a plethora of different applications is reported. Commercial barium titanate crystals are polydisperse materials that have a large second-order susceptibility, generating strong SHG signals even at low illumination intensities, and are utilized for a proof-of-principle investigation on the variety of functionalization schemes. The model biological system used for *in vivo* imaging are zebrafish due to their transparency, which allows easy optical access to cells and tissues and for the zebrafish embryo being a well-established organism in cell biological analyses of vertebrate development [52]. In addition, sensitive early embryonic zebrafish embryos provide a subtle test of the health of the cells during rapid division, as any slowing in their development would indicate toxicity of the barium titanate [21]. The polydisperse nature of BT SHG probes has been a limiting factor in their application, and an investigation on the synthesis of monodisperse non-centrosymmetric nanocrystals was attempted. Chapter 3 describes the efforts utilized in the synthesis of monodisperse, spherical, hexagonal zinc oxide nanocrystals, which has been shown

to have a strong dependence on the capping agent composition and method of coating. In the final chapter, the future direction of the functionalization of SHG nanoprobes is proposed that should address some of the current limitations of SHG nanoprobes—mainly their signal enhancement and the wavelength of generated light.

Chapter 2

Functionalization of Barium Titanate Nanocrystals and Applications in Biological Systems

2.1 Introduction

Barium titanate is a perovskite with excellent dielectric, piezoelectric and ferroelectric properties. Bulk BT crystals exhibit noncentrosymmetric tetragonal structure at room temperature and have been reported to elicit no toxicity in biological organisms [21, 38], making them potential SHG probes for biological imaging. Indeed, tetragonal BT is a strong SHG emitter [53, 54] and can be obtained commercially as 200 nm tetragonal particles in powder form. Since pristine dry samples of BT nanoparticles are strongly aggregated, surface modifications need to be performed to help disperse and impart greater stability by overcoming the various surface interactions between them. Surface modification of oxides can be achieved by either electrostatic interaction, chemisorption or hydrophobic interaction of ligands, which provide desired functionality, to the surface [44].

Electrostatic interactions can occur between hydrophilic particles due to the repulsion of equally charged ligands on particle surfaces. These repulsive interactions are not very stable in high ionic strength solutions due to the shielding of the electric field, ultimately enabling attractive forces between the particles to dominate, causing

particle aggregation. Chemisorption involves a chemical reaction between the ligand and the surface and is characterized by a more stable bond under a variety of chemical conditions. Various chemical functional groups possess a certain affinity to inorganic surfaces [44] and can be utilized for both targeted and nontargeted functionalization. Previously, barium titanate surfaces have been coated with phosphonic acid conjugated PEG [55] and polycarboxylic polymers (PAA) [56] for nontargeted biocompatible functionalization. Targeted functionalizations of biological relevance have also been reported for BT coated with glycol-chitosan and doxorubicin [57], and immunoglobulin G (IgG) antibody via silane coupling [38, 21].

Applications for SHG nanoprobes in biology are wide-ranging and dependent on the surface functionality. In general, SHG nanoprobes may be used in conjunction with traditional exogenous and endogenous fluorescent labels as an additional unique spectral label for multimarker imaging, such as is necessary for long-term stem cell tracking at the level of a single cell in culture and *in vivo* [58]. Other applications include the use of a bolus of dispersed SHG nanoprobes as indelible markers for lineage tracing experiments within living organisms [22], since these probes should redistribute within some number of subsequent daughter cells after successive divisions during development or regeneration, replacing or acting in conjunction with traditional dye-injection or cell transplantation strategies [59]. The benefit of the SHG nanoprobes is that they may be especially attractive for higher-order vertebrate (e.g., mouse) lineage tracing or cell-tracking experiments, as their bright, high SNR signal will be of particular interest, since these embryos become more absorptive and scattering as development proceeds past the gastrula period. The streptavidin conjugation after biotinylation of the surface of BT will allow selective attachment to biotinylated molecules for specific cell targeting—such as receptor ligands or antibodies—as was described previously for quantum dots [60]. The direct conjugation of antibodies to the surface through covalent means would also enable specific cell labeling for immunostaining as well as live cell targeting.

To functionalize the surface of barium titanate, we opted for the covalent attachment of a linker to the surface utilizing the naturally occurring hydroxyl groups ex-

posed on the surface of oxides. The linker of choice was N-aminoethyl-2,2,4-trimethyl-1-aza-2-silacyclopentane for three reasons: (a) the reagent has exposed amine groups that are readily utilized in bioconjugation with well-established reaction procedures [48] and provide a convenient amine platform for further functionalization with a large variety of biomolecules, (b) the covalent attachment of the linker allows for greater stability in a variety of solvents, and (c) during the synthesis there is no by-product formation which eliminates laborious washing procedures and minimizes toxicity concerns. Utilizing the amine platform, a variety of chemical functionalities have been imparted on the SHG probes and utilized for both specific and nonspecific targeting *in vivo*. Similarly, the hydroxyl groups on the surface of the oxide were utilized for the direct attachment of fluorescent probes to the surface of the BT SHG probe, enabling potentially localized enhancement of the fluorophore signal, providing interesting opportunities in the synthesis of novel NIR exciting and emitting probes.

2.2 Surface Functionalization and Analysis Procedures

2.2.1 Amine Functionalization of Barium Titanate

In order to prepare the SHG nanoprobes for biological imaging, functionalization is necessary to ensure biocompatibility, to achieve sufficient particle separation, and to prevent aggregation before introduction into biological tissues. Commercial 200 nm tetragonal barium titanate nanoparticles, purchased from Nanostructured and Amorphous Materials, with 99.9% purity, were selected as the SHG probe of choice. To ensure the composition and the crystalline structure of the nanoparticles, powder X-ray diffraction (XRD) analysis was performed (figure 2.1) indicating the sample composition to be tetragonal barium titanate with no crystalline impurities present. To prepare the surface of the BT nanoparticles for a silanization reaction with N-aminoethyl-2,2,4-trimethyl-1-aza-2-silacyclopentane, 400 mg of commercial barium

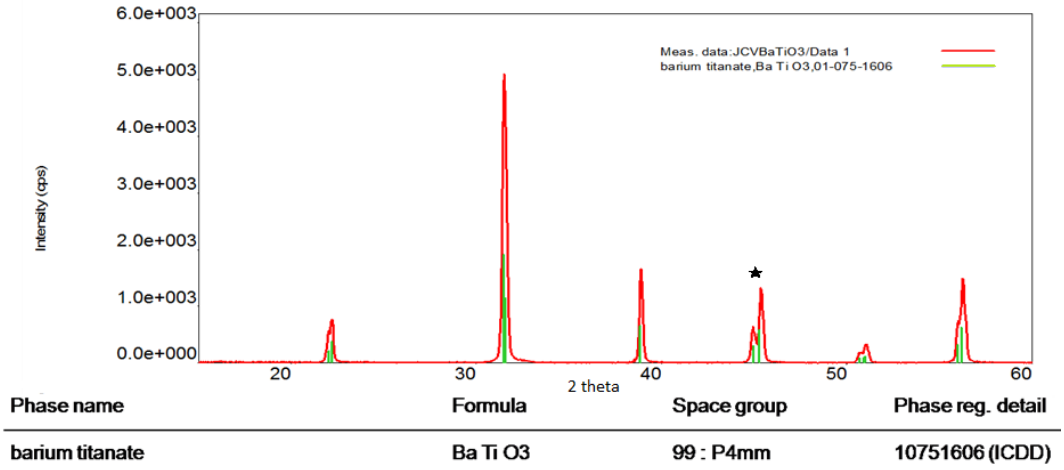

Figure 2.1: Powder X-ray diffraction pattern of commercial barium titanate sample. All of the peaks on the intensity vs. 2-theta graph are assigned to barium titanate (JCPDS 75-1606), indicating no crystalline impurities are present in the sample. The splitting of the (002) peak at ∼44.9 2 theta degrees and (200) peak at ∼45.4 2 theta degrees, indicated with the star, is assigned to the tetragonal P4mm symmetry.

titanate (figure 2.2a) were first sonicated with 25 mL of 30% aqueous solution of hydrogen peroxide (H_2O_2) for 30 min in a Teflon flask to homogenize the dispersion. The solution was then kept for 4 hrs at 110°C under reflux in an inert environment to obtain a BT-OH surface (figure 2.2b). These conditions have been optimized to saturate the surface with hydroxyl (-OH) groups as reported previously [61]. A beneficial consequence of the H_2O_2 treatment is that it will strip any surface adsorbed carbonates layer on the barium titanate, similar to the action of weak aqueous acetic acid solutions [62]. Vacuum drying of the washed BT-OH powder using the Schlenk line will prevent the readsorption of the carbonate layer. After hydroxylation, a 22 hr surface silanization reaction with 1% (v/v) N-aminoethyl-2,2,4-trimethyl-1-aza-2-silacyclopentane was performed at room temperature in anhydrous toluene in an argon filled Teflon flask (figure 2.2c). The particles were washed by centrifugation in ethanol and water. Silane surface functionalization is achieved as a result of a ring-opening reaction made possible by hydroxyl groups on the oxide surface. This reaction, driven by the thermodynamically favorable formation of an oxane bond with silicon, results in a high density monolayer formation without any by-products [63] with amine groups exposed, referred to as the BT-NH_2 surface.

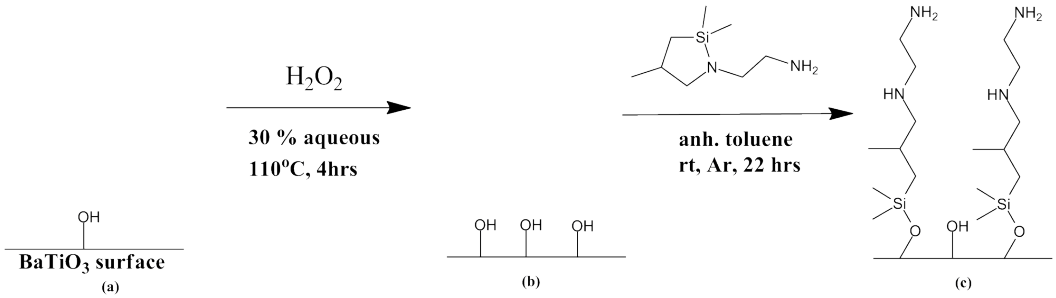

Figure 2.2: Schematic of barium titanate surface functionalization. The BT surface (a) natively has some hydroxyl groups exposed. By exposure to the 30% aqueous hydrogen peroxide solution, the surface of barium titanate is saturated with -OH groups (b). To expose the amine functional groups, the favorable reaction of N-aminoethyl-2,2,4-trimethyl-1-aza-2-silacyclopentane with the surface hydroxyl groups is performed in anhydrous toluene for 22 hours.

To verify the presence of different functional groups on the BT surface by means of a rapid spectroscopic technique, Fourier transform infared (FT-IR) analysis was performed on BT, BT-OH, and BT-NH_2 samples using the KBr pellet method. The powders of BT and BT-OH samples were characterized at a concentration of 2 mg within a 47.5 mg KBr matrix, and a BT-NH_2 sample at a concentration of 3 mg within a 49 mg KBr matrix. A few drops of the N-aminoethyl-2,2,4-trimethyl-1-aza-2-silacyclopentane solution were deposited on an IR polymer film card and used as a hydrolyzed reagent control for referencing the IR absorption peaks in the BT-NH_2 sample (as indicated by the matching arrows in figure 2.3a). The dominant peaks in the three BT spectra correspond to Ti-O stretch (around 550 cm^{-1}) [64] as well as the Ti-O bend (around 425 cm^{-1}) [65]. The wide stretch around 3000 cm^{-1} in the inset of figure 2.3b (blue line) indicates that H_2O_2 treatment hydroxylates the BT surface—and in conjunction with subsequent vacuum drying—is successful in eliminating the adsorbed carbonate layer that is present in the commercial BT powder spectrum (figure 2.3b, asterisk, the weak peak at $\sim$1435 cm^{-1} disappears after hydroxylation). The BT-NH_2 sample spectrum (figure 2.3b, red line) has Si-CH_3 bands at 1260 cm^{-1} and 800 cm^{-1} from the -O-Si$(CH_3)_2$- group, along with the overlapping bands at 1130-1000 cm^{-1} that are characteristic of Si-O-Si groups introduced in the surface silanization reaction [66].

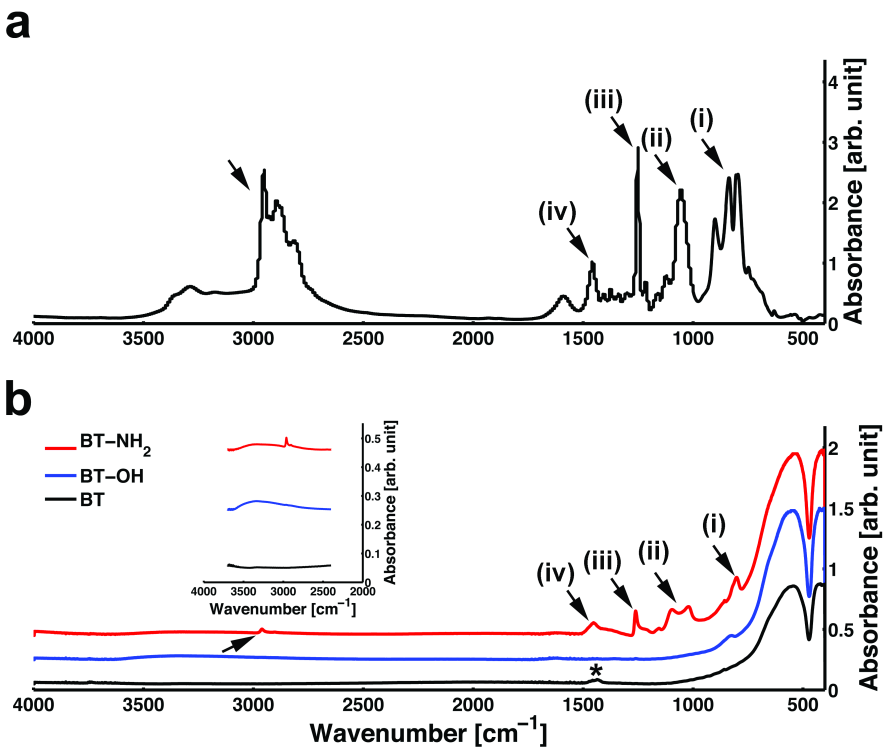

Figure 2.3: (a) As a standard for comparison to BT-NH_2 an IR spectrum was taken of a few drops of N-aminoethyl-2,2,4-trimethyl-1-aza-2-silacyclopentane coating the surface of an IR film card. The spectrum shows the common peaks for the hydrolyzed silane material as a control. (b) IR spectra for bare commercial BT (black line), BT-OH after hydroxylation (blue line) and BT-NH_2 (red line). Note that the stretch for Ti-O (around 550 cm^{-1}) and the Ti-O bend (around 425 cm^{-1}) dominate the spectra. Focusing on the region of the spectrum between 780 and 1500 cm^{-1} enables appreciation of the peaks representing proper silane coating of the surface of BT-NH_2 (red line) including the 800 cm^{-1} (i) and 1260 cm^{-1} (iii) stretches corresponding to Si-CH_3 bands in –$Si(CH_3)_2O$– group within the silane chemical structure as well as the double-overlapping peak between 1100 and 1300 cm^{-1} (ii) corresponding to Si-O-Si absorption. The peak in the BT-NH_2 data (red line) near ∼1450 cm^{-1} (iv) corresponds to contributions from the alkane groups in the chemical structure. In addition, the 1435 cm^{-1} stretch (asterisk, black line) that corresponds to to the adsorbed carbonate groups is eliminated after surface hydroxylation with H_2O_2 (blue line). The inset graph shows a zoom of the graphed data to better appreciate the –OH stretch, which appears after hydroxylation of the BT (blue and red lines, around 3450 cm^{-1}). In the BT-NH_2 data (red line), a weak peak near 2960 cm^{-1} can also be seen, which is also present in the silane control spectrum in panel a and is due to the alkane groups stretching. Note that in order to better appreciate the nuances of each graph, a global offset factor of 0.05 was added to all absorbance data and an offset factor of 0.2 and 0.4 was added to the absorbance values of the BT-OH and BT-NH_2 data, respectively.

In addition to the FT-IR analysis, transmission electron microscopy (TEM, 300 kV) images of the BT and BT-NH_2 samples are shown in figure 2.4 along with the respective energy dispersive X-ray spectroscopy (EDS) analysis for each. The TEM samples have been prepared by a deposition of a small aliquot of the dilute solution ($\sim$20 μL) onto a carbon-coated Cu 200 mesh grid. The aliquot was allowed to rest for a minute, and the excess solution was wicked away, and the grid stored aside for drying. Differing surface morphology is apparent when comparing the bare commercial BT (figure 2.4a) and the silane functionalized BT surface (figure 2.4b). The surface of BT-NH_2 is characterized by the presence of an amorphous layer around tetragonal-crystalline functionalized BT (inset in figure 2.4b, dotted yellow line). Additionally, control BT tends to cluster more tightly than the functionalized BT-NH_2, where there are clear gaps in between nearby particles. Thus, functionalization of the BT surface reduces aggregation of the particles, achieving a more disperse solution that can be used for introduction into biological samples. In addition, the EDS analysis of the samples (figure 2.4c) clearly indicates the presence of silicon atoms only in the silanated sample.

2.2.2 Biotinylation of Amine Functionalized Barium Titanate

The terminal ends of the silane layer are exposed amine functional groups (figure 2.5a) that are convenient for use in a variety of bioconjugation reactions. One such reaction is the addition of an azide functionalized surface via 1-ethyl-3-(3-dimethylaminopropyl) carbodiimide (EDC)/N-hydroxysuccinimide (NHS) coupling of 6-azido-hexanoic acid. Amine-coated BT (30 mg) was dispersed in 1 mL anhydrous dichloromethane (DCM) and reacted with excess EDC (10 mg), NHS (10 mg) and 6-azido-hexanoic acid (75 mg) for 4 hrs at room temperature [48]. The azido modified BT (BT-N_3, figure 2.5b) was washed by centrifugation with ethanol and water. A small aliquot of the BT-N_3 sample was dispersed by sonication in 1xPBS and reacted overnight at room temperature in a copper-free click chemistry reac-

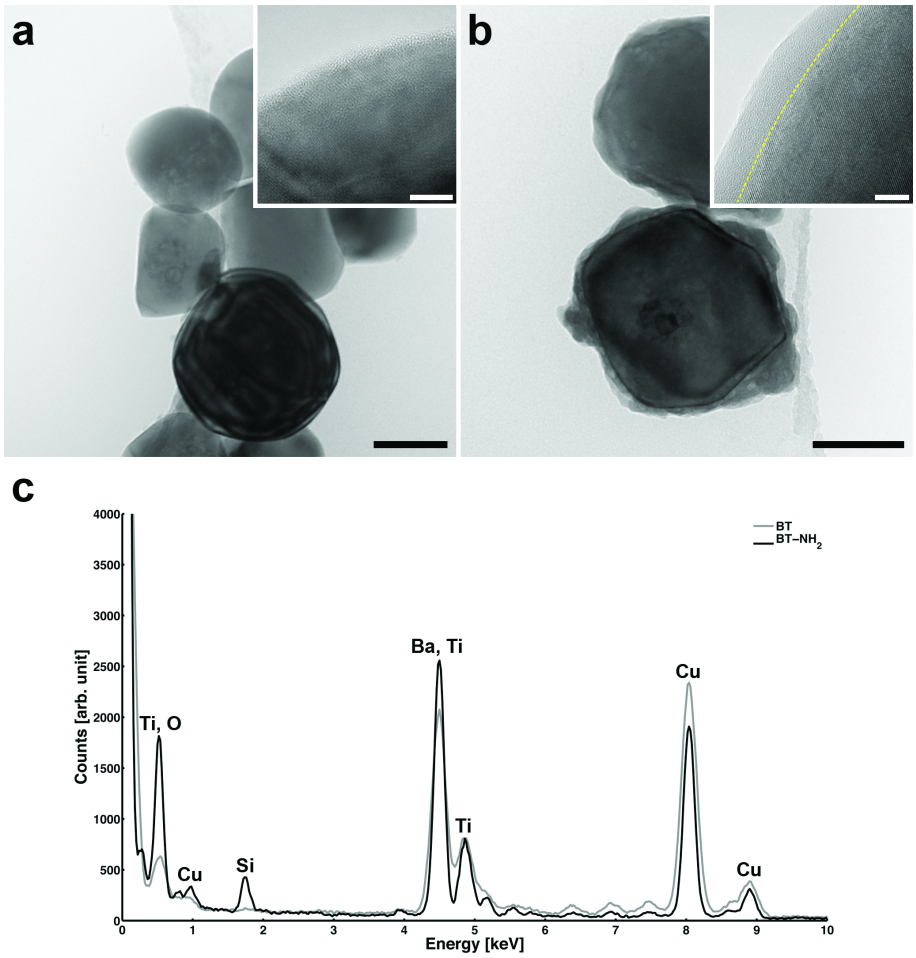

Figure 2.4: TEM images and EDS analyses confirming surface coating of BT. (a) TEM image of nonfunctionalized BT control at 178,600x magnification as well as at 4,753,000x magnification (inset). Note the lattices representing the crystallinity of the material, which is an essential requirement to be met for SHG. (b) BT-NH_2 at 136 300x magnification and at 3,724,000x magnification (inset) showing the presence of an amorphous layer (of variable thickness, usually ∼5nm) around the crystal particle. Note that the N-aminoethyl-2,2,4-trimethyl-1-aza-2-silacyclopentane coating is a single layer at the outermost edge of the amorphous coat and that the thickness of the amorphous coating may be attributed to barium leaching during hydroxylation. (c) EDS spectra indicating the atomic composition of nonfunctionalized BT nanocrystals (gray line) and functionalized BT-NH_2 (black line). In addition to the characteristic peaks for BT, there is a new peak in the BT-NH_2 data that is specific to the presence of Si atoms in the sample. Note that the Cu that is detected in each of the atomic composition histograms arises from the TEM grid itself. Scale bars: 100nm (main figures) and 5nm (insets).

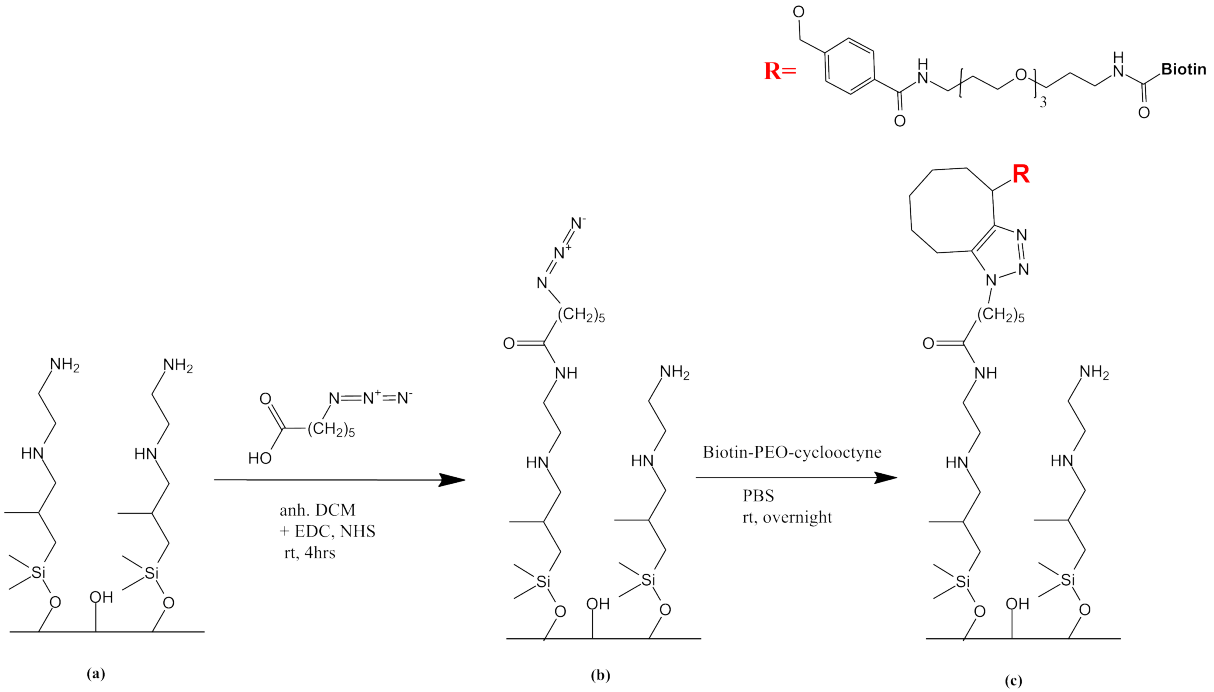

Figure 2.5: Schematic representation of the functionalization procedures to modify the amine-coated barium titanate surface (a) with 6-azido-hexanoic acid via EDC/NHS coupling and expose azide functional groups on the BT surface (b). Further functionalization to exposed biotin on the surface (c) can be achieved utilizing a high yield, copper-free click chemistry reaction of azide functional groups with cyclooctyne-PEO-biotin.

tion with 3 µL of 10 mM biotin-PEO-cyclooctyne [50], producing biotin-coated BT nanoparticles (referred to as biotin-BT, figure 2.5c). The product was washed 3 times in 1x PBS by centrifugation, and the sediment was collected.

To test for successful functionalization using the amine-coated BT surface as a platform, it is desirable to have a straightforward method of comparison using, e.g., confocal and SHG imaging. The biotin-BT generated by this procedure is a reasonable functionalization routine that can accomplish this goal, when conjugated to fluorescent AF488-conjugated streptavidin. Bare BT and biotin-BT solutions in 1x PBS were incubated in separate vials with 10 µL of 2 mg/mL AF488-conjugated streptavidin for 1 hr in the dark at room temperature before being washed three times by centrifugation. Aliquots of the solutions (200 µL) were placed in separate wells of an 8-well coverslip chamber and the solution was allowed to sediment for several minutes. Using a Zeiss C-apochromat 40x/1.2NA W Corr M27 objective and the 34 channel spectral detector on an LSM 710 microscope in lambda mode, signal was obtained from particle clusters—from 421 to 587 nm in ∼10 nm increments—at the surface of the coverslip upon illumination with 965 nm light from a two-photon laser source. Using an automated script, the SHG nanoprobe clusters from each well were segmented using the SHG signal channel, since these crystals will have this characteristic signal at 482.5 nm regardless of whether AF488-conjugated streptavidin coating exists or not. A mask was created from segmented crystal data that had an area between 6 and 10 pixels (characteristic of larger than diffraction limited particles, which would have greater nonsaturated AF488 signal, if the signal is present), and the mask was used to obtain the average intensity for each wavelength increment within the spectral band (421 to 587 nm). This value for average intensity for a given SHG nanoprobe cluster was then normalized to its respective area in pixels. From a single spectral scan at the coverslip after significant sedimentation, 465 SHG nanoprobe clusters in the functionalized well and over 53 SHG nanoprobe clusters in the control well of an 8-well coverslip imaging chamber were segmented using the SHG channel data with a simple Matlab script. The average intensity for photons collected within each wavelength band (10 nm increments in this case) was normalized to the size of each

of the SHG nanoprobe clusters and was plotted in figure 2.6.

In each case, SHG signal occurs within the 480 nm wavelength bin for both non-functionalized and functionalized BT. However, unlike the spectra for control BT, which is negligible other than the SHG peak, signal from the BT-streptavidin-AF488 spectrum has SHG signal that colocalizes with the characteristic spectra of AF488 (emission at 521 nm). A paired T-test with unequal sample size and unequal variance confirms that the BT and BT-streptavidin-AF488 have different spectra for the wavelength range from 489 to 587 nm ($\sim$10 nm increments) with high confidence (p-value $< 10^{-4}$). Thus, this is a reasonable imaging-based method to judge proper surface functionalization of the BT surface. The multistep functinalization of BT-NH_2 indicates that the stable amine surface coating will be a successful platform for further functionalization methods that generate well-dispersed BT nanoprobes for long-term *in vivo* imaging, such as with PEG-BT.

2.2.3 PEGylation of Amine Functionalized Barium Titanate

Taking the functionalization a step further to enable nonreactive surface coating of SHG nanoprobes, amine functionalized BT can be coated with carboxylic acid monofunctional poly(ethylene glycol) (PEG-COOH, average molecular weight of 2,000 Da) in anhydrous DCM with a similar EDC/NHS coupling reaction (figure 2.7) used for biotin-BT synthesis. Excess PEG-COOH (30mg) was reacted with 10 mg BT-NH_2 dispersed in 1 mL DCM by sonication, with 10 mg of EDC and 10 mg of NHS added. The reaction was allowed to proceed for 4 hrs at room temperature, and the final product was washed in ethanol and water by centrifugation, and the liquid supernatant was discarded. PEG is a biocompatible polymer that effectively suppresses nonspecific binding of proteins to nanoparticles [67]. Similarly, any molecular weight of PEG can be used for the surface modification, with the most suitable molecular weights of PEG reported in the range of 1.5–5 kDa [67].

To confirm the PEG functionalization of the BT nanoparticles, salt stability size

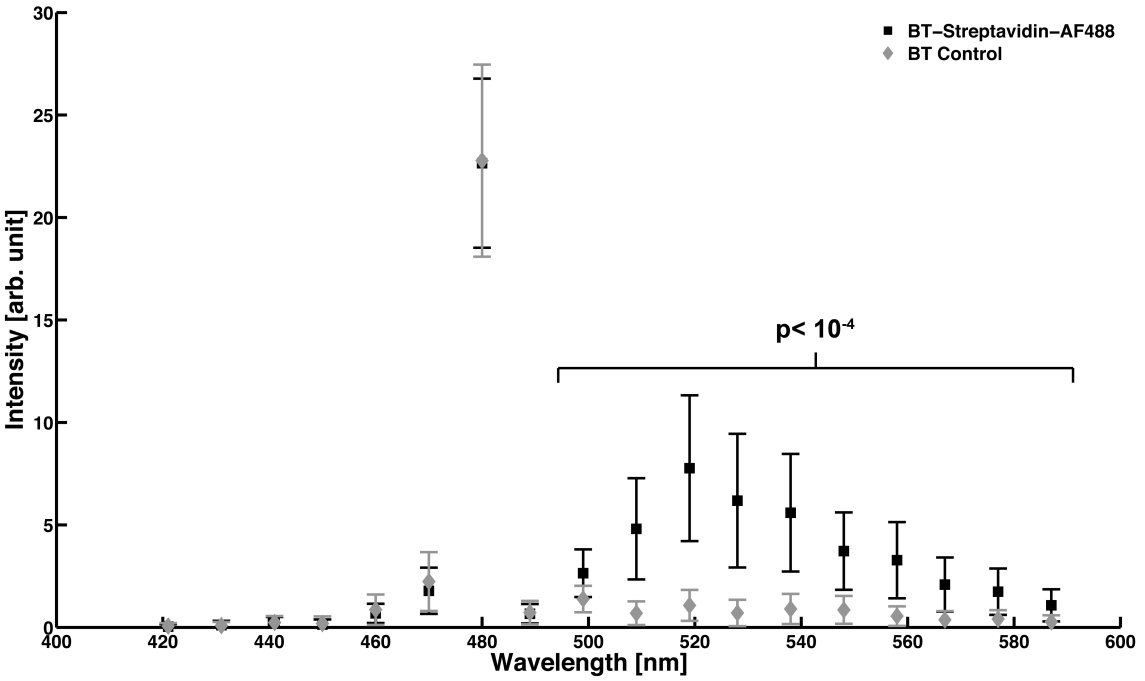

Figure 2.6: Bare BT and biotin-BT were incubated in separate vials with AF488-conjugated streptavidin for 1 hr before being washed three times by centrifugation. Samples were illuminated with 965 nm two-photon light and analyzed at the surface of the coverslip for the SHG signal at 482.5 nm and the emission from the AF488 dye. Average normalized intensity and standard deviation (error bars) from 53 BT (gray diamonds) and 465 BT-streptavidin-AF488 (black squares) SHG nanoprobe clusters at each wavelength increment was plotted using Matlab. In each case, SHG signal occurs within the 480 nm wavelength bin for both nonfunctionalized and functionalized BT. However, unlike the spectra for bare BT, which is negligible other than the SHG peak, signal from the BT-streptavidin-AF488 spectrum has SHG signal that colocalizes with the characteristic spectra of AF488. A pairwise T-test with unequal sample size and unequal variance confirms that the BT and BT-streptavidin-AF488 have different spectra for the wavelength range from 489 to 587 nm ($\sim$10nm increments) with high confidence (p-value $< 10^{-4}$).

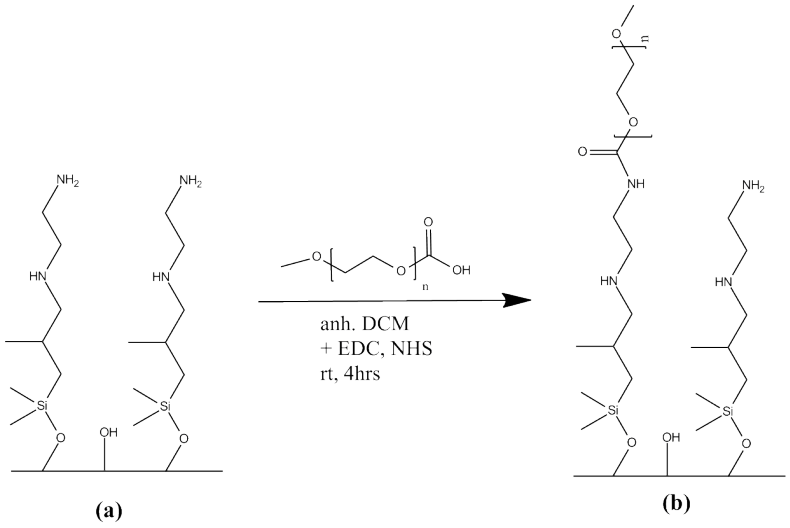

Figure 2.7: Schematic representation of the PEGylation of amine-coated barium titanate surface via EDC/NHS coupling.

measurements were performed at room temperature by dynamic light scattering. For this analysis, the hydrodynamic radius of the nanoparticles is measured in UltraPure water for 10 min (data collected at 1 min time intervals), as well as in 1x PBS solution for ten 1 min intervals (figure 2.8). Particles not properly polymer-coated should display an increase in nanoparticle size when in salt solution due to the shielding of the surface charge by the buffer ions. Dynamic light scattering analysis shows that the PEG-BT samples have no appreciable increase in the particle hydrodynamic diameter upon the addition of 11 μL of 10x PBS in 100 μL of solution of PEG-BT in water at the 10 min time point, as compared to the BT control sample. Average hydrodynamic radius of the PEG-BT sample increases from 191 to 211 nm, while the nonfucntionalized BT samples hydrodynamic radius increases from 184 nm to 8.30 μm. Importantly, nonfunctionalized BT has widely varying size ranges when performing dynamic light scattering analysis even in water, indicating a much wider range of particle aggregate sizes, which is in sharp contrast to the more consistent cluster sizes of PEG-BT samples. Therefore, from the salt stability study, where the nanoparticles were exposed to effectively 1x PBS solution, only the PEG-BT solution was stable as opposed to the BT control solution, as expected.

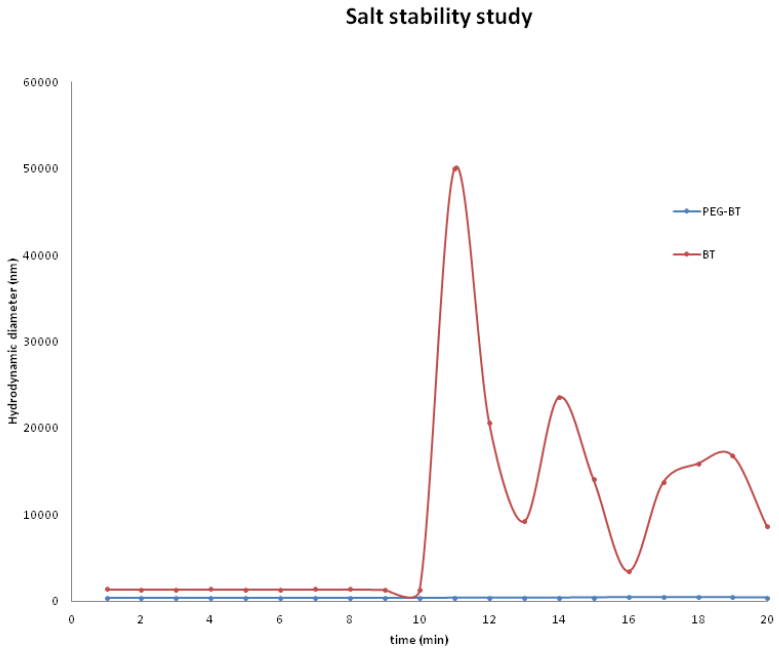

Figure 2.8: Salt stability study on the BT and PEG-BT samples dispersed in 100 μL Ultrapure water by the measurement of the hydrodynamic diameter as a function of time. At the 10 min time point, 11 μL of 10xPBS solution was added, to obtain a 1xPBS solution, effectively. The average hydrodynamic diameter of the PEG-BT particles in water is 382 nm, and in 1xPBS solution is 420 nm (corresponding to a 10% increase in size). In contrast, the average hydrodynamic diameter of BT particles in water is 376 nm, and in 1xPBS is 16.6 μm (corresponding to a 4421% increase in size). Note the vertical offset of 1000 nm applied to the BT graph to better appreciate the nuances of the graphs.

2.2.4 Antibody Functionalization of Amine Functionalized Barium Titanate

Functionalization of barium titanate with antibodies allows for specific targeting of structures of interest within the organism. Procedures for the bioconjugation of antibodies are well established [48] and vary by the chemistry and location of antibody targeting. Glycoproteins, biological molecules that contain polysaccharides, can be modified specifically at the sugar residues to produce reactive functional groups. One subset of glycoproteins are immunological molecules, immunoglobulin G (IgG) antibodies, which have a Y shape and can be divided into two regions. The first region, comprised of the arms of the Y, is the fragment of the antibody that specifically binds to the antigen and is called Fab (fragment, antigen binding) region. The second region, comprised of the base of the Y, plays a role in the immune response and is entitled the Fc (fragment, crystallizable) region. The polysaccharide chains in the IgG are only found in the Fc region of the antibody, far from the active binding sites. Therefore, by oxidizing the sugar residues on the Fc region, one can produce reactive aldehyde groups and utilize them for site-specific conjugation of SHG probes to the antibody, as schematically described in figure 2.9.

The general procedure used for antibody targeting is to disperse 10 mg of BT-NH_2 in 0.1 M sodium phosphate 0.15 M sodium chloride buffer, pH 7.14 by sonication for 30min. The nanoparticles are reacted with 2 mg of succinimidyl 2-hydrazinonicotinate hydrochloride (SHNH) in 100 µL anhydrous DMF for 1 hr at room temperature. The powder was washed by centrifugation in buffer 3 times. Alexa Fluor 488 conjugated IgG goat anti-rabbit secondary antibody was oxidized for 25 minutes with sodium periodate $NaIO_4$ (2.5 mg in 100 µL water, kept in the dark). Sodium sulfite was used to quench the reaction for 5 minutes. The antibody was washed with centrifuge membrane (3 kDa) against 0.1 M sodium phosphate buffer, 0.15 M NaCl, pH 7.14. Hydrazine modified BT-NH_2 was dispersed in 300 µL of water by sonication to which 100 µL of antibody solution was added and stirred in the dark for 2 hrs at room

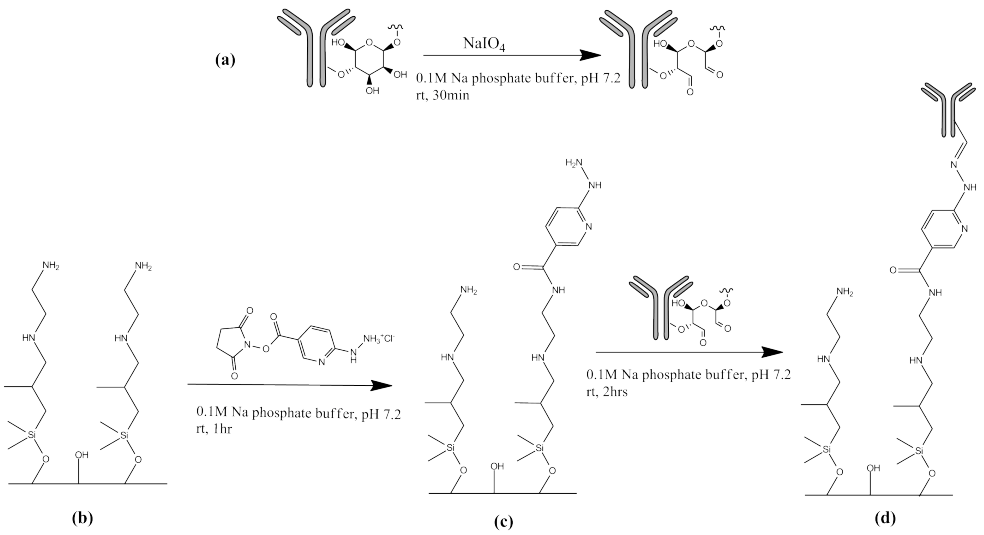

Figure 2.9: Schematic representation of the BT surface functionalization with specifically targeting glycosylated IgG antibody. (a) The sugar residues on the Fc region of the antibody are oxidized with sodium periodate. The surface BT-NH2 (b) is modified with SHNH reagent, exposing hydrazine functional groups on the barium titanate surface (c). The aldehyde functional groups react with hydrazine moeities forming a specifically targeted coating on the barium titanate surface (d).

temperature. To stabilize Schifft's bases, 10 µL/mL of 5 M sodium cyanoborohydride solution was added and stirred in the dark for 30 min at room temperature. To block the unreacted aldehyde sites on the antibody, 50 µL/mL 1 M ethanolamine solution was added and stirred in dark for another 30 min at room temperature. The powder was finally washed with a centrifuge membrane (300 kDa) against buffer.

Antibody-coated BT nanoparticles were analyzed for the colocalization of SHG signal by confocal and SHG microscopy. figure 2.10 indicates the colocalization of fluorescent dye and SHG probe signal for all the different concentrations of AlexaFluor conjugated IgG antibodies that were oxidized by sodium periodate and reacted with hydrazine-coated BT. The colocalization of the SHG and fluorescent signal is stable over the course of weeks upon storage at 4°C in 1x PBS.

2.2.5 Corrole Functionalization of Hydroxylated Barium Titanate

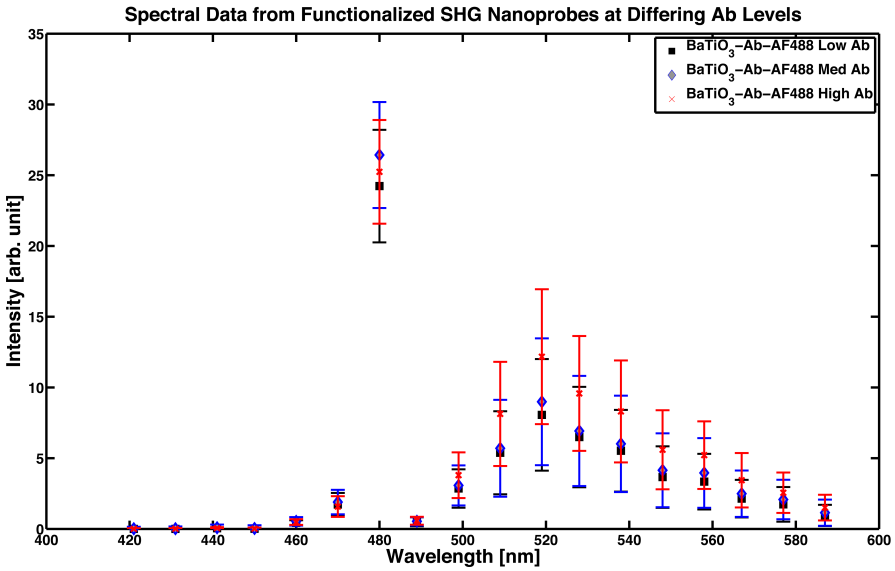

Figure 2.10: Barium titanate surface was coated with AF488-conjugated IgG antibody with varying concentrations of oxidized antibody. The samples were illuminated with 965 nm two-photon pulsed laser. The colocalization of the SHG signal at 482.5 nm and the AF488 emitted signal at 521 nm indicate that the antibody functionalization was successful.

The use of illumination light in the NIR region has the benefit of being less absorbed and scattered by the biological tissues. With the use of SHG probes alone, the SHG signal detected is always one half of the input wavelength-producing light in the visible range (anti-Stokes shift). By coating the surface of SHG nanoprobes with dyes that are excited in the visible range and emit in the NIR range, one can create an imaging probe capable of interacting with and emitting light in the NIR range. This would lead to minimal losses of signal, from to the tissue interaction with the light, for both excitation and emission. A novel imaging probe was designed by functionalizing the barium titanate surface with corroles, a novel imaging probe was designed.

Corroles are tetrapyrrolic molecules that are able to stabilize metal ions in higher oxidation states and easily participate in substitution and metallation reactions, allowing for synthesis of numerous corroles with varying solubility properties, making them useful in many different applications [68]. The photophysical properties of corroles are dependent on their structure as well as the chemical environment that they

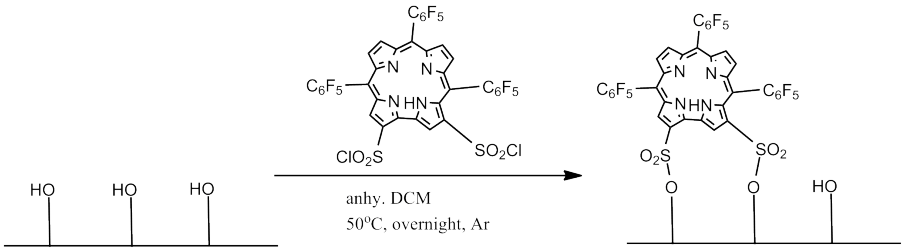

Figure 2.11: The schematic representation of the chemical reaction between the surface hydroxyl groups on the barium titanate and the chlorosulfonyl groups on the corrole in anhydrous DCM in an inert Ar environment.

are in. In general, corroles have a skeletal structure of corrin and can be modified with a variety of chemical groups for different chemical applications and fluorescent properties [69].

The method of functionalization of chlorosulfonated corroles with BT-OH nanoprobes as shown in figure 2.11 was by the reaction of the chlorosulfonyl group with the surface hydroxyl group, with the elimination of HCl. To achieve this, 18 mg of BT-OH was first dried at 150°C and under a pressure of 2 mbar to eliminate any residual water on the barium titanate surface. Upon cooling down to room temperature with inert gas (Ar) flushing, a solution of 2,17-bis-chlorosulfonated-5,10,15(trispentafluorophenyl)corrole in anhydrous DCM was added to the flask via cannule. The solution was refluxed overnight under inert gas at 50°C. The sample was collected and washed three times with DCM, once with acetone and once in water. A control experiment was performed with 15 mg of BT-OH mixed with 5,10,15-(trispentafluorophenyl)corrole under the same experimental conditions. Samples were analyzed for colocalization of fluorescence signal and SHG signal in 1xPBS. As demonstrated in figure 2.12a, the corroles on the surface of the BT-corrole sample emit light at 670 nm when excited by two-photon laser at 780 nm, and SHG signal is generated by the BT nanoparticle when illuminated by 940 nm light. This colocalization of SHG and fluorescent signal was not observed in the control sample (figure 2.12b).

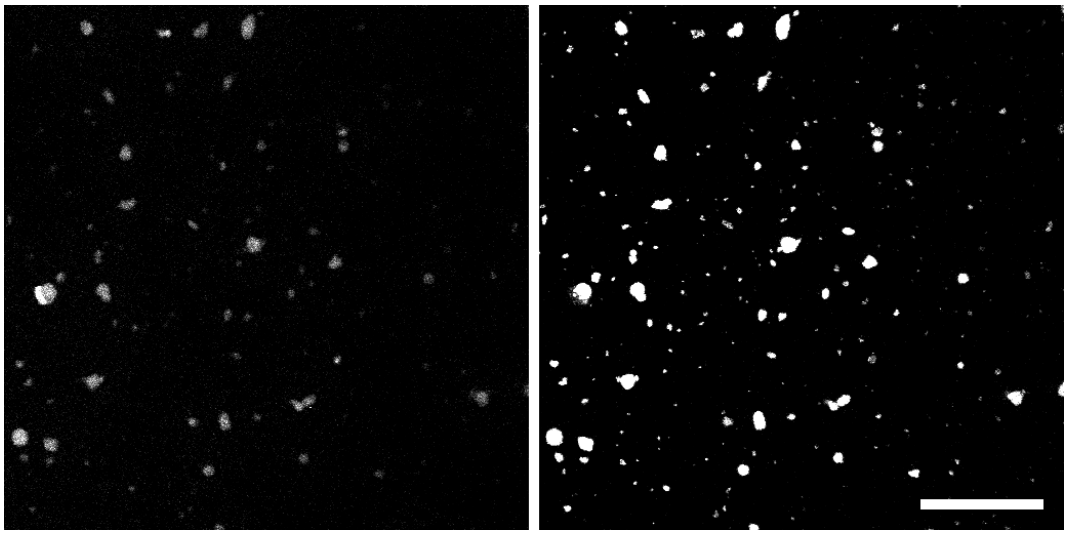

(a) BT sample functionalized with 2,17-bis-chlorosulfonated-5,10,15(trispentafluorophenyl)corrole

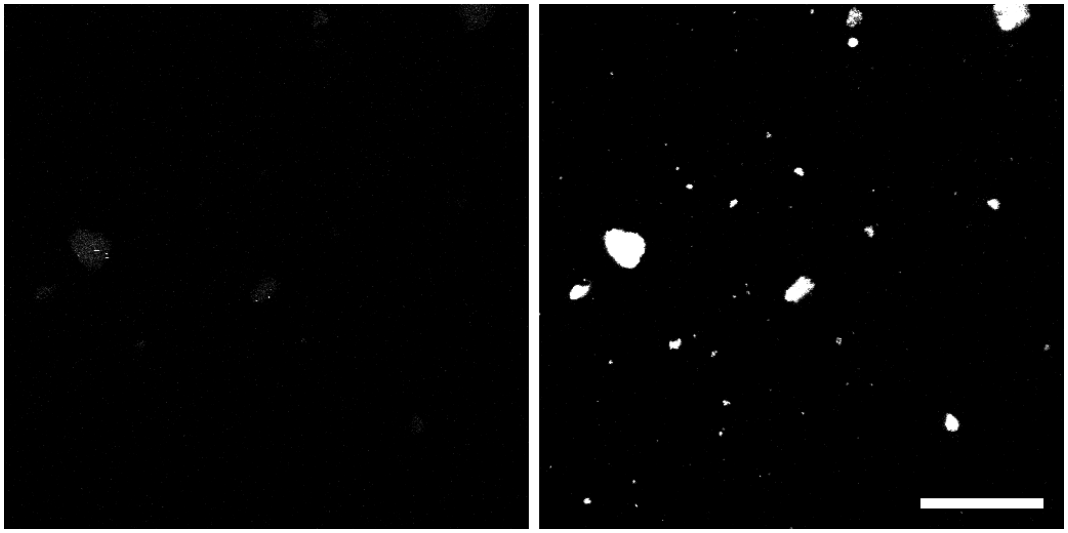

(b) BT sample mixed with 5,10,15(trispentafluorophenyl)corrole

Figure 2.12: The fluorescent corrole emission utilizing two-photon pulsed laser at 780 nm (left panel) is colocalized with the SHG barium titanate nanoprobe signal from 940 nm two-photon pulsed laser illumination. Scale bar: 100 μm.

2.3 Application in Biological Systems

The SHG probes can be incorporated in an *in vivo* setting using a simple method of zygote stage injection of dispersed, PEG functionalized SHG nanoprobes. Over time, the dramatic cell divisions and migration, that are hallmarks of early development, cause the SHG nanoprobes to distribute within a large number of cells, and these nanoparticles can be imaged within the developing embryo. The *in vivo* example presented below illustrates the utility of the SHG nanoprobes: because of the high signal-to-noise ratio (SNR), superior brightness, and absence of bleaching/blinking, SHG nanoprobe labeling of cells within a biological tissue of interest will allow for long-term imaging even within challenging (i.e., highly scattering and absorbing) tissue environments.

In addition, barium titanate nanoparticles were conjugated with goat anti-mouse secondary IgG antibody with an AlexaFluor488 tag and used for indirect staining of whole zebrafish embryos that were permeabilized with Triton X detergent. The main advantage of the indirect staining method is the flexibility in the use of the primary antibody—which in this instance was the anti-dystrophin mouse host antibody. Staining of the dystrophin protein is observed at both the transverse and horizontal myosepta, which form the anterior and posterior borders of the muscle segments (myotomes), and divides the muscle into dorsal and ventral compartments, respectively [70].

Barium titanate nanoparticles conjugated to rat anti-mouse CD117 (cKit) primary antibody were used in the mouse hematopoetic stem cell uptake study. The CD117 protein is a transmembrane tyrosine-kinase receptor encoded by *Kit* gene which is expressed in the stem cells and can be directly targeted by the cKit antibody or cKit antibody conjugated BT nanoparticles (BT-cKit).

2.3.1 Imaging SHG Nanoprobes within Living Zebrafish Embryos

In order to incorporate SHG nanoprobes in vivo, a diluted dispersion of PEG-BT was sonicated in deionized water for 30 min within a bath sonicator for greater nanoparticle homogenization before injection. Several examples of BT imaging within living zebrafish embryos can be seen in figure 2.13 and figure 2.14. In each of these cases, within 5 min of sonication, zebrafish embryos are injected with 2.3 nL of PEG-BT solution by inserting a borosilicate needle into the yolk cell of the embryo near to or inside of the zygote cell. Though direct cell injection may be preferable to ensure that a large number of particles is distributed into the organism, yolk cell injection has a decreased chance of embryo lethality due to imperfect use of the injector. After yolk cell injection, cytoplasmic streaming and cell cytoplasmic connections maintained with the yolk during cleavage stages [71] allows the nanoparticles to be taken into the embryonic cells. After allowing the embryo to develop at 28°C for as many as 24 hrs–depending on the desired stage of development–embryos are embedded in 0.1%-1% low melting point agarose within LabTek 2-well plates with #1 coverslip bottomscoverslip chambers. To show that SHG nanoprobes are localized within cells of the zebrafish after yolk cell injection, various dye markers can be used to label the cells within the embryo. 10,000 MW Dextran-AFlexa546 is a dye that can be coinjected with the PEG-BT during the zygote injections. This is an effective troubleshooting tool to ensure that zygote injections are successful before attempting to image on the laser scanning microscope: after injection, embryos that have been properly manipulated will have blastomeres that fluoresce under a mercury lamp when using an appropriate filter cube (e.g., Zeiss filter set 43 Cy 3). Additionally, Bodipy TR Methyl Ester or Bodipy FL C5 ceramide dyes can be incubated with a dechorionated zebrafish embryo prior to imaging to label the cell interior or cell membranes, respectively. Alternative methods that can also provide cellular context to PEG-BT localization include ubiquitous or tissue-specific fluorescent protein ex-

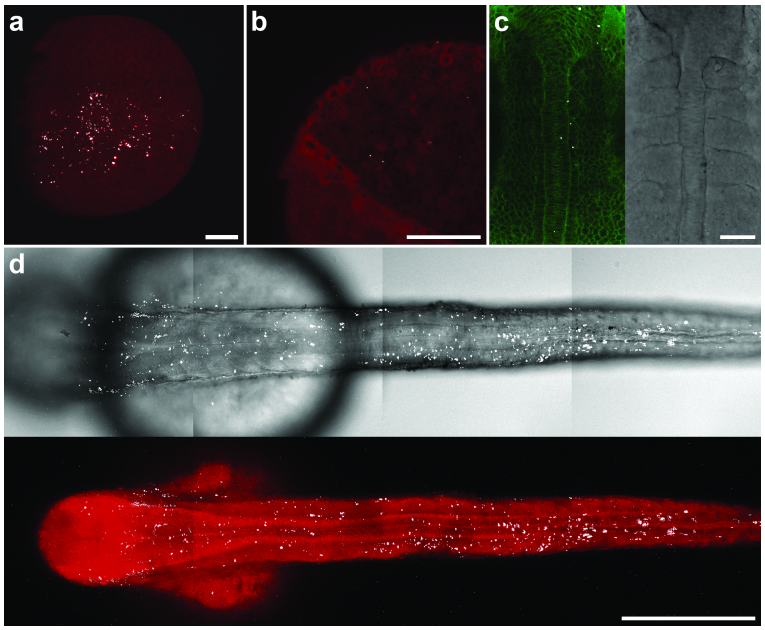

Figure 2.13: PEG-BT localizes and persists within cells of the developing zebrafish embryo after zygote stage microinjection. (a) By the sphere stage of development, scattered PEG-BT (white) can be seen within a great number of cells in the blastodisc in this surface reconstruction projection (∼88 µm in depth) of a slightly tilted animal pole mounted zebrafish embryo. In this case, 10,000 MW Dextran-AF546 was coinjected with the PEG-BT at the zygote stage to act as an injection control: properly injected embryo cells fluoresce when illuminated with a laser around the peak excitation of the AF546 dye (red channel in the surface reconstruction). (b) In a single optical slice image of a laterally mounted sphere stage zebrafish embryo (animal pole is toward the top right, ∼40 µm into the embryo in depth), PEG-BT (white) can be seen within 6 Bodipy TR methyl-ester labeled cells. Note that Bodipy TR methyl-ester was incubated with dechorionated embryos at a concentration of 100µM for 1 hr before washing three times in egg water followed by imaging. (c) Staining with 100 µM Bodipy FL C5 ceramide for 1 hr followed by 3 washes in egg water during the early segmentation period allows visualization of cell membrane boundaries within the embryo to better appreciate the intracellular localization of the PEG-BT. Here, the zebrafish was imaged at the 5 somite stage (∼12 hrs postfertilization) in a dorsal orientation (anterior toward the top), which can be best appreciated in the bright field channel (right image). In the left image, PEG-BT (white) can be seen within the Bodipy-labeled membrane boundaries (green) of 9 cells in various tissue compartments (notochord, somites, and neural territories of the developing brain) within a single optical slice ∼72 µm deep within the embryo with respect to the dorsal surface. (d) In this panel, a PEG-BT injected zebrafish was transferred from egg water to egg water containing 1x PTU at ∼16 hrs postfertilization to prevent pigment formation. Before imaging, the embryo was anesthetized with 0.015% Tricaine methanesulfonate and dorsally mounted (anterior to the left, bright field in top image) using forceps in 1% agarose with 0.015% tricaine methanesulfonate and 1x PTU. PEG-BT (white, top and bottom images) persists within cells throughout the body of the zebrafish even after 24 hr of development, as can be seen in this ∼48 µm maximum intensity (starting ∼50µm in depth from the dorsal surface) projection of a 100 µM Bodipy TR methyl-ester stained zebrafish embryo (red, bottom image). Scale bars: a-b, 100 µm; c, 50 µm; d, 300 µm.

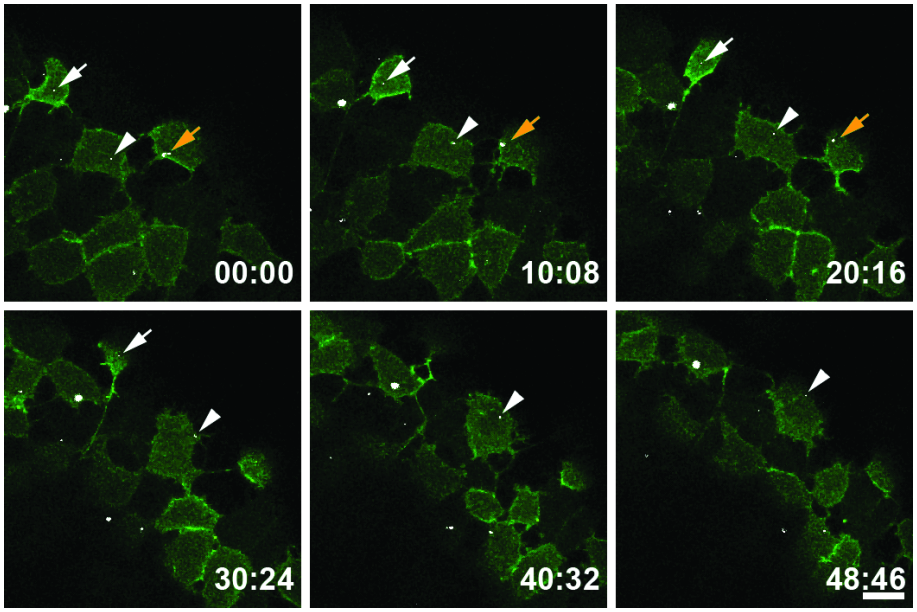

Figure 2.14: *in vivo* time-lapse imaging of PEG-BT within a zebrafish gastrula embryo. The following are images from a time-lapse movie of a mid-gastrula period zebrafish embryo mounted in an animal pole orientation using a Zeiss C-Apochromat 40x/1.20 W Korr M27 objective. First, 20 ng/µL plasmid membrane-targeted photoconvertible fluorescent protein Dendra2 DNA and 80 ng/µL Tol2 transposase mRNA were injected along with PEG-BT nanoprobes at the zygote stage. This DNA/mRNA injection enables the embryo to be labeled in a mosaic manner—that is, only a subset of the total cells in the embryo will have a proper insertion of the plasmid DNA into the genome by the expressed transposase protein, enabling expression of the membrane-targetted Dendra2 protein. Three images ∼2.5 µm apart in the z-direction were taken of the embryo for each time-point with no delay between frames, and approximately 38 sec were needed to capture each time-point. The resulting image stacks were maximum intensity projected in the z-direction. PEG-BT (white) nanoprobes can be seen in several Dendra2-labeled (green) as well as unlabeled cells. One diffraction limited SHG nanoprobe can be seen within one Dendra2-labeled cell throughout the time-lapse during epiboly migration (arrowhead), while other cells containing single SHG nanoprobe clusters move out of the plane of view over time (white and yellow arrows). Note that the varying sizes of the nanoprobes within the video presumably stem from anomalous subdiffusion and molecular crowding within cell compartments (e.g., endocytic compartments). Time-stamps: min:sec. Scale bar: 20 µm.

pression by means of either simultaneous nucleic acid (e.g., mRNA DNA encoding a fluorescent protein of interest) injection with the PEG-BT at the zygote stage or by using a fluorescent transgenic zebrafish line.

By the late blastula period into early gastrulation, a number of SHG nanoprobes are scattered within the blastodisc, the pile of cells sitting atop the yolk cell that will eventually form the body of the zebrafish (figure 2.13a). In this case, 10,000 MW Dextran-AlexaF546 was coinjected with PEG-BT at the zygote stage at a concentration of ∼0.02 mg/ml to give contrast to the cells sitting atop the yolk. On separate occasion, PEG-BT was injected into zebrafish zygote stage embryos once again, this time without the addition of Dextran-AF-546 (figure 2.13b). figure 2.13b depicts a zoomed in single optical section of one of the embryos at blastula stage after a 1 hr incubation in 100 µM Bodipy TR, showing the clear intracellular localization of the SHG nanoprobes. A second PEG-BT injected embryo was allowed to develop into the early segmentation period before staining with 100 µM Bodipy FL C5 ceramide for 1 hr to visualize SHG nanoprobes inside membrane boundaries within the developing somites and notochord (figure 2.13c). Even after ∼12 hrs of development, the SHG nanoprobes are still localized and visible inside of cells of the embryo. Note too that imaging after gastrulation is a particularly sensitive test for toxicity. Any deleterious effect that could occur from introducing a compound that perturbs necessary cell behaviors—rapid cell divisions, directed cell motion and rearrangements (e.g., convergence and extension [71])—for body formation would be magnified, possibly forestalling proper development of the organism. Though many PEG-BT clusters can be seen in cells within the embryo, gastrulation still proceeds to completion. SHG nanoprobes can be seen throughout the zebrafish embryo even ∼24 hrs after injection at the zygote stage (figure 2.13d). Importantly, any or all of the numerous SHG nanoprobes within the zebrafish cells may be used to track cells in time and space throughout any stage early development without loss of signal due to photobleaching or blinking. To demonstrate in vivo time-lapse imaging of the SHG nanoprobes within living zebrafish embryos, fluorescent protein and SHG nanoprobe imaging were employed in tandem (figure 2.14). At the zygote stage, simultaneous in-

jections of 20 ng/µL plasmid membrane-targeted photoconvertible fluorescent protein Dendra2 DNA with 80 ng/µL Tol2 transposase mRNA were performed to label the embryo in a mosaic manner as previously described [72, 73] along with PEG-BT. figure 2.14 shows snapshots from an ∼48 min time lapse during late-stage gastrulation, where single SHG nanoprobe clusters can be seen within at least three Dendra2-labeled epiblast as the cells migrate across the surface of the embryo. Note that the two labels work well together—mosaic Dendra2 fluorescence allows visualization of membrane dynamics and morphology, while SHG from the SHG nanoprobes enables interrogation of intracellular dynamics and cytosolic fluidity. Additionally, several nonfluorescent cells are presumably labeled with SHG nanoprobes and can be seen during the time lapse, since these SHG nanoprobes move across the surface of the embryo at similar rates similar to the other labeled cells in the image. Perhaps most importantly, these SHG nanoprobes are high contrast labels that will not overlap in space when labeling even adjacent cells (unlike untargeted ubiquitous cytosolic fluorescence, for example), so they will be especially useful for tracking colabeled cells in time in three dimensions as the embryo develops, as well. Note that even at illumination wavelengths below the tissue damage threshold (∼10 mW for cell culture [74]), SHG nanoprobes can be seen in time with high contrast without the limitation of bleaching or blinking.

2.3.2 Specificity of Antibody Targeting

For indirect staining of the whole ∼2.5 day post-fertilization zebrafish embryos, goat anti-mouse secondary IgG antibody with an AlexaFluor488 tag was conjugated to the BT surface. First, the whole mounts were fixed in 4% paraformaldehyde or methanol-free formaldehyde (for either 1 hr at room temperature, or overnight at 4°C), followed by blocking nonspecific binding in 1x PBS (without Ca^{2+}/Mg^{2+}) with the addition of 0.1%-1% Triton X-100, 0.5%-1% bovine serum albumin (BSA) overnight at 4°C. Additionally, the whole mounts were added 1% DMSO for greater tissue pene-

tration. The tissue sections were reacted with a 1:1000 dilution of primary monoclonal mouse Anti-Dystrophin (MANDRA1, Developmental Studies Hybridoma Bank) antibody concentrate for 90 min at room temperature. Upon washing, the tissue sections were exposed to the IgG antibody conjugated barium titanate nanoparticles at a 1:3 dilution in the blocking solution for a 3 day incubation at 4°C. The whole mounts were washed thrice and imaged within an hour of washing (figure 2.15a). As a control for the targeted staining, the secondary antibody (AF488 tagged goat anti-mouse secondary IgG) solution was exposed to the tissue sections at a dilution of 2:500 in the blocking solution for 2 hrs at room temperature (figure 2.15b).

The observed SHG and AF488 signal colocalization, left panels in 2.15a, indicates that the secondary antibody is conjugated to the surface of barium titanate. The emitted signals are located along the myosepta, as is clearly visible from the control experiment (figure 2.15b). In addition, a large population of BT-Ab nanoparticles remain stuck in the yolk, due to the lipids present (which is an unfortunate, but expected result, since the particle size is large).

For the mouse hematopoetic stem cell uptake study of directly targeted BT-Ab nanoparticles, first bone marrow cells were harvested from humerus and tibia bones of two freshly killed mice. The cells were purified by affinity purification, where anti-cKit coated magnetic beads were incubated with the cells and then run through a magnetic column. The purified cells were split into two equal volumes, incubated in 1x Hanks balanced salt solution: one containing a control solution of dispersed BT-OH particles, and the other with the solution of dispersed BT-cKit nanoparticles. The cells were incubated for 15 min on ice and spun down in a density gradient of lymphocyte separation medium (Cellgro) to separate the cells from the BT nanoparticles that sediment at the bottom in the Cellgro medium. The cells remain at the interface between the Hanks balanced salt solution and the separation medium. Cells were then fixed in 4% formalin and imaged in 8-well coverslip chambers. Eleven independent regions on the plate for each of the two conditions (control BT-OH and functionalized BT-Ab) were analyzed. From these 11 regions, the total number of cells on the plate was counted by hand, as well as the total number of cells that seemed to have crystals

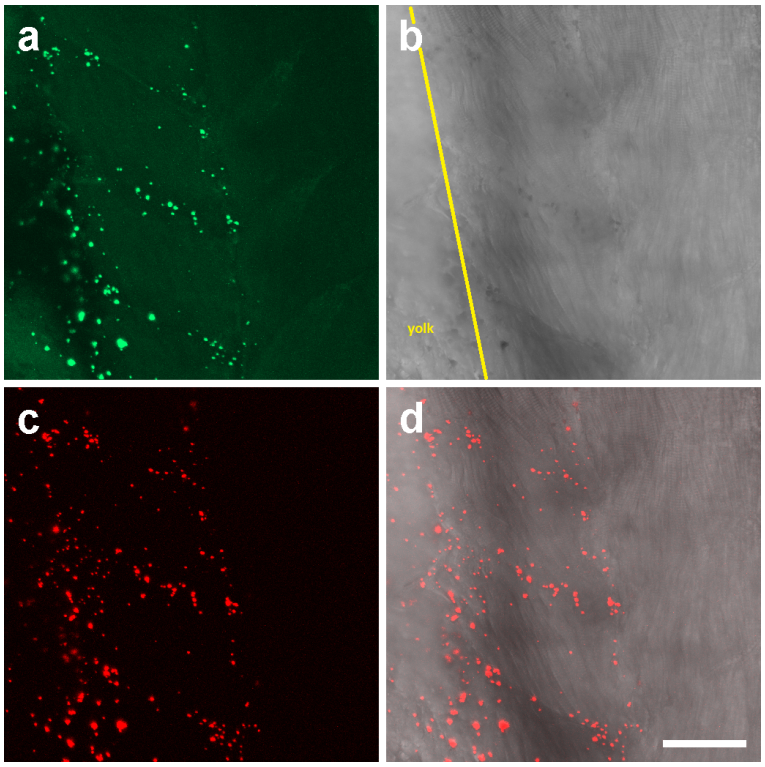

(a) Specific targeting of the zebrafish myosepta with barium titanate nanoparticles conjugated with IgG- AF488 secondary antibody

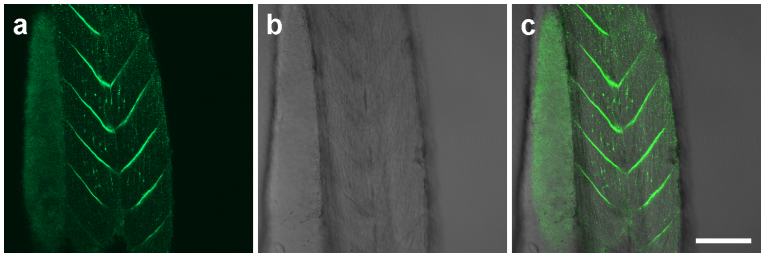

(b) Control staining of zebrafish with non-conjugated secondary antibody

Figure 2.15: (a) Functionalized BT nanoprobes exposed over zebrafish tissue sections incubated prior with 1% TritonX100 solution. Signal can be seen from the AlexaFluor488 tag on the secondary antibody (top left), as well as with the SHG signal from the BT nanoprobe (bottom left) in regions along the myosepta. Bright field image (top right) and merge of the bright field and SHG signal (bottom right). Note the SHG nanoprobes alignment, for the most part, is along the vertical myosepta, with a large portion of the nanoparticles getting stuck to the lipids present in the yolk (on the left-hand side of the bright-field image). Scale bar: 50 µm. (b) Control zebrafish targeting of dystrophin. The AlexaFluor488 fluorescence signal from the secondary antibody not conjugated to the SHG nanoparticles (left). Bright-field image (middle) merged with the fluorescent signal (right) with the yolk clearly visible. Note that the puncta originate from the muscle-muscle junctions where dystrophin is also expressed. The whole mount embryos are facing anterior down, ventral left in both panels (a) and (b). Scale bar: 100 µm.

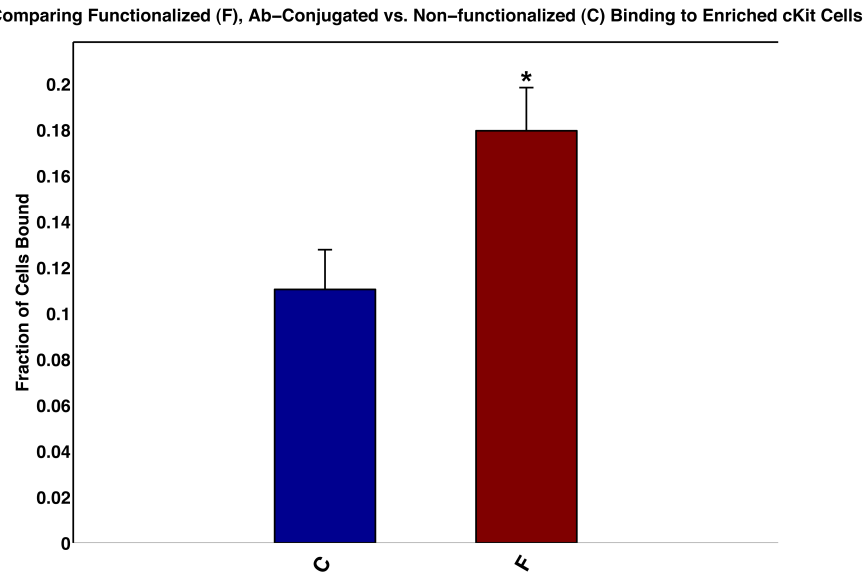

Figure 2.16: Comparing the mouse hematopoetic stem cell uptake of cKit conjugated barium titanate nanoprobes (denoted as F) to the control BT-OH nanoprobes (denoted as C), enhancement in the uptake is observed. The cell surface coverage of 18% as compared to the 11% for the control BT-OH probes. A two-tailed T-test with unequal variance confirms that the BT-cKit and BT-OH are differently uptaken by the cells with high confidence (p-value $< 10^{-4}$).

attached: 4008 cells counted total in the control BT-OH case and 6756 cells total for the surface functionalized BT-cKit case. Two-tailed T-test with unequal variance, determined a significant p-value that is $<<10^{-4}$ with an enhanced cell surface coverage of 18% in the case of BT-cKit, as opposed to the 11% nonspecific cell surface coverage for the control (figure 2.16).

2.4 Conclusion

The protocols presented in this chapter outline the general methods of BT SHG nanoprobe functionalization, their introduction *in vivo*, and their imaging in tissues and cells of a model organism—zebrafish. As a platform for a plethora of possible further chemical modifications, amine-coated barium titanate nanoparticles were generated by silanization of hydroxylated oxide surfaces with cyclic azasilane. Further

functionalization steps, including EDC/NHS coupling to carboxylic acid functional groups and hydrazine linkage to aldehyde groups on oxidized sugar residues on antibodies, allowed barium titanate SHG nanoprobes to be coated with a variety of ligands for both nontargeted and targeted functionalizations. The covalently bound ligands were stable over a course of weeks and in different environments, as confirmed by repeated colocalization of SHG and fluorescent signal, when appropriate, or by FT-IR analysis for BT-NH_2 samples. The use of BT SHG probes in *in vivo* allows for long-term imaging of stable, nontoxic, biocompatible probes that are not limited by dye saturation, dye bleaching or blinking.

The procedures presented in this chapter are not exhaustive and can be modified for alternative functionalities or model organisms. Use of alternative biocompatible polymers—such as the poly(acrylic acid) (PAA) polymer [56]—can provide an even more widespread binding to the BT surface than monofunctional PEG, enabling greater surface coverage. Additionally, utilizing commercially available heterofunctional PEG reagents, which contain different functional groups on their ends, SHG nanoprobe surfaces could be specifically targeted. This could be achieved by careful selection of functional groups that posses a high affinity to the surface and surface exposed functional, while the other functional end on the PEG polymer would be utilized for specific targeting of biological sructures.

The biotin functionalization presented here served as a straightforward means of gauging the success of the modification procedure by means of colocalization of AlexaFluor488 fluorescent and BT SHG signal. However, the same biotin-BT probe can be directly used for targeted imaging. Biotin has a high affinity for avidin and steptavidin ($K_D \sim 10^{-15}$) proteins and the biotin-BT probes could be used for sensing applications, among others [75, 76].

Barium titanate SHG nanoprobes have also been functionalized with fluorescent dyes, corroles. Corroles are small molecules which can be synthesized with a variety of functional groups attached, and thus tuned for different photophysical properties. Corroles are especially interesting for the synthesis of novel imaging probes that can interact with NIR light and emit photons in the NIR range as well. By careful design,

the SHG nanoprobes will supply the visible light, needed for the corrole fluorescence excitation. The relationship of this SHG enhanced fluorescence with respect to the distance between the BT nanoparticle and the corrole can be investigated as a function of the length of the intermediate linker between the two imaging probes. Therefore, utilizing corroles with different functionalities, one can investigate the SHG enhancement of the fluorescent signal as well as the photophysical properties of a variety of different BT-corrole probes.

In general, the major limitation of the SHG nanoprobes in biological imaging applications is straightforward: in contrast to fluorescent proteins, these probes cannot be used in applications requiring genetically encoded labeling. Additionally, since commercially available ∼100-200 nm BT nanocrystals are the starting material for functionalization in this protocol, applications for single molecule analysis or efficient cell or protein targeting are limited, even when extending the protocol to targeted labeling such as with the biotin linking chemistry. This restriction will be lifted once efficient synthesis of monodisperse, tetragonal BT SHG nanoprobes is accomplished with sizes comparable to currently used fluorescent probes (less than 10 nm). Current established BT synthesis protocols in the desired size range only result in cubic (i.e. centrosymmetric) crystal structures due to quantum confinement effects [77].

Monodispersity of SHG nanoprobes is desired for a number of reasons. Polydisperse nanoparticles have a wide distribution of sizes which in general limits their application in biological systems. It has been demonstrated that the distribution of nanoparticles in the body and their interaction with cells is greatly influenced by the size of the nanoparticles, as well as their targeting ligand content [51]. In addition, monodisperse particles posses uniform physical and chemical properties, which enables their easier characterization, functionalization, and ultimately application. By controlling the size, and thus the properties of the particles, many interesting studies can be conducted, such as determining the dependence of the SHG signal on the size of the probe. Currently reported values of the second order susceptibilities for different SHG nanoprobes, have been normalization over the average nanoparticle volumes, introducing calculation errors due to the broad size distributions [78].

Therefore, a fundamental study on the SHG efficiency in monodisperse nanoparticle samples would allow greater understanding of their nonlinear optical properties. This would allow for more sensitive multispectral imaging with SHG nanoprobes, as the intensity of the SHG signal would be better resolved [21].

Chapter 3

Synthesis of Zinc Oxide Nanoparticles

3.1 Introduction

Zinc oxide, ZnO, is a semiconductor material with unique catalytic, electronic, magnetic and photonic properties [79]. Zinc oxide has been intensely utilized in solar cells [80], sensors [81], photocatalysis [82], cosmetics and pharmaceuticals [83], UV-light emitting devices, and textiles [84]. In addition, ZnO nanoparticles have been utilized as imaging probes due to the broad, defect-related photoluminescence emission in the range of approximately 500-540 nm with narrow 380 nm excitation [85, 86]. Hexagonal zinc oxide nanoparticles, which is the thermodynamically stable phase of ZnO at ambient conditions, have been used in SHG imaging [39, 86]. Hexagonal ZnO is a good SHG probe for biological imaging, as it is a biocompatible, nontoxic material with strong second-order susceptibility [85, 83, 87]. For high-quality imaging applications, the synthesis of uniform, monodisperse nanocrystals is of utmost importance. There have been a variety of reported methods of synthesis of zinc oxide: solvothermal [88, 89, 90, 91], hydrothermal [92, 93, 94], microwave-assisted polyol [95, 96], chemical vapor deposition [97], precipitation [98], and organometallic synthesis [99].

Many successful zinc oxide synthesis protocols have been developed for preparing stable colloidal solutions. One particularly successful and widely used method is the hydrolysis of Zn^{+2} salts in a basic alcoholic solution [89]. The size and morphology of the nanoparticles were effectively controlled by the choice of solvent and stabilizing

ligands. Zinc oxide nanocrystals exhibit preferential growth along the c-axis and have polar surfaces (slightly positively charged (0001) Zn surface and negatively charged $(000\bar{1})$ O surface) and nonpolar, energetically more favorable and stable $(10\bar{1}0)$ and $(11\bar{2}0)$ surfaces [100]. Due to the energetic differences between differently charged surfaces, to which polar solvent and ligand molecules could attach to, a variety of morphologies were observed for zinc oxide particles [42, 101].

The objective of the work presented in this chapter was the synthesis of monodisperse ZnO particles with sizes less than 10 nm, which is comparable to the biological macromolecules and fluorescent probes. The formation of monodisperse, colloidal nanoparticle suspensions is governed by either degradation of bulk particles or by aggregation of small ions into nanoparticles. Generally, the dispersion of bulk material, by either mechanical grinding in colloidal mills or by ultrasonication does not lead to extensive subdivisions, as small particles tend to reunite under the influence of the attractive forces between the particles as well as the mechanical forces. A higher degree of dispersion is generally obtained by an aggregation method, which involves a supersaturated solution of precursor that precipitates into particles of desired size. The formation of a new phase involves distinct stages: nucleation, particle growth and termination.

3.2 Classical Nucleation Theory

In classical nucleation theory, a new phase formation occurs when the concentration of the solute in the solvent exceeds the equilibrium solubility or when the temperature is decreased below the phase transformation point. Since the Gibbs free energy (ΔG) is high in solutions with solute concentration exceeding the solubility, in order to reduce the overall energy a new phase is formed. Therefore, the driving force for the processes of homogeneous nucleation and growth is the reduction in ΔG. If the nucleation process leads to spherical particle formation, the change in the Gibbs

free energy of formation of a new volume is

$$\Delta\mu_v = k_B T ln S, \tag{3.1}$$

where S is the supersaturation, T the temperature, and k_B Boltzman's constant. The reduction in the overall energy, due to the formation of a new phase, is balanced by the energy of introduction of a new surface. The energy of the new surface is described by

$$\Delta\mu_s = 4\pi r^2\gamma, \tag{3.2}$$

where γ is the surface energy per unit area, and r the radius. The overall energy of the cluster is the sum of the energy contribution from the volume and the surface, $\Delta\mu_v$ and $\Delta\mu_s$:

$$\Delta G_n = -\frac{V}{v_c}\Delta\mu_v + \Delta\mu_s = -\frac{4\pi r^3}{3v_c}\Delta\mu_v + 4\pi r^2\gamma, \tag{3.3}$$

where V is the volume of the nuclei and v_c is the molar volume of the cluster. Therefore, as the precursor molecules (monomers) form the cluster by successful collisions, the cluster grows. However, the process of cluster growth is in equilibrium with its dissolution. There exists a critical size of the cluster that leads to formation of stable particles (nuclei), which will continue to grow. This critical size, r^*, is determined thermodynamically as the radius of the cluster when $\Delta G_n$is at its maximum:

$$\frac{d\Delta G_n}{dr} = 0 = \frac{-4\pi r^{*2}}{3v_c}\Delta\mu_v + 8\pi r^*\gamma \Rightarrow r^* = \frac{2\gamma v_c}{\Delta\mu_v}. \tag{3.4}$$

The energy barrier that needs to be overcome for the formation of stable nuclei is then $\Delta G_n^* = \frac{16\pi\gamma^3}{3}\left(\frac{v_c}{\Delta\mu_v}\right)^2$. The rate of nucleation (I) can be determined by assuming that only monomers are attached to the growing cluster and that the processes of attachment and dissolution of the monomer from the cluster are at a pseudo-steady state. The rate of nucleation is dependent on the Gibbs free energy of formation of a critical nuclei as described by

$$I = I_{max} e^{\left(\frac{-\Delta G_n^*}{k_B T}\right)}. \tag{3.5}$$

Therefore, the nucleation rate increases as the supersaturation and temperature is increased. In heterogeneous nucleation, which takes place in the presence of a foreign substrate, the energy barrier (ΔG_n) for nucleation is effectively lowered and is dependent on the contact angle between the foreign substrate and the solution.

Ideally, for the synthesis of monodisperse particles, the nucleation and the growth processes are separated, such that the nucleation takes place abruptly followed by a quick decrease in the solute concentration, preventing new nuclei from forming. Thus, the solute present contribute to the growth of the nanoparticles until the concentration of the monomers is reduced to the equilibrium concentration. The size distribution of the particles is dependent on the growth kinetics. Particles grow as monomers successfully collide and attached to the nuclei, where they can stay at the initial point of contact, diffuse across the surface to a more energetically favorable position, or detach back into the solution. The growth process, referred to as Ostwald ripening, is governed either by the diffusion of the monomers to the particle surface or by the surface reaction [102, 103].

The local concentration of the monomer at the surface of the particle (C_s) is smaller than the bulk concentration of monomer in the solution (C_b) at a distance δ from the particle surface. The concentration difference is the driving force for the flux (J) of monomer to the growing particle surface and is described by Fick's first law in spherical geometry:

$$J = 4\pi r^2 D \frac{dC}{dr} = \frac{4\pi D r(r+\delta)}{\delta}(C_b - C_s), \tag{3.6}$$

where D is the diffusion coefficient of the monomer and is governed by the Stokes-Einstein equation ($D = \frac{k_b T}{6\pi\eta r}$, where η is the viscosity of the solvent), r is the radius of the particle and δ the diffusion layer thickness. At the particle surface, the consumption rate of monomers is described by a first-order reaction with the flux:

$$J = 4\pi r^2 k_d (C_s - C_r), \tag{3.7}$$

where k_d is the first-order decomposition rate, C_r is the solubility of the particle with radius r. The flux, J, is defined as the change in number of monomers per time, and since the number of monomers in a spherical particle of radius r is expressed as ratio of particle volume over the molar volume v_c:

$$J = \frac{dN}{dt} = \frac{d}{dt}\left(\frac{4\pi r^3}{3v_c}\right) = \frac{4\pi r^2}{v_c}\frac{dr}{dt}. \tag{3.8}$$

Then the linear growth rate of the particle is

$$\frac{dr}{dt} = \frac{Jv_c}{4\pi r^2}. \tag{3.9}$$

At steady state the diffusion flux (equation (3.6)) equals the reaction flux (equation (3.7)), which enables the flux to be expressed in terms of measurable parameters as

$$J = \frac{4\pi D r^2 (r+\delta)}{r\delta + \frac{D(r+\delta)}{k_d}}(C_b - C_r). \tag{3.10}$$

Therefore, the growth rate of the particle is expressed as

$$\frac{dr}{dt} = \frac{\frac{D}{r}(1+\frac{r}{\delta})v_c}{1+\frac{D}{rk_d}(1+\frac{r}{\delta})}(C_b - C_r). \tag{3.11}$$

The thickness of the diffusion layer is much greater than the radius of a nanoparticle, therefore the ratio of r/δ is close to zero. For a diffusion limited growth, where the diffusion of monomer to the surface is the rate controlling step, the growth rate (equation (3.11)) can be simplified as

$$\frac{dr}{dt} = \frac{Dv_c}{r}(C_b - C_r), \tag{3.12}$$

while for reaction-limited growth, the reaction rate is

$$\frac{dr}{dt} = k_d v_c (C_b - C_r). \tag{3.13}$$

The growth rate law is diffusion limited for many nanoparticle synthesis procedures. Since the chemical potential of a particle increases with decreasing particle size, the equilibrium solute concentration for a small particle is much higher than for a large particle, as described by the Gibbs-Thompson equation [104].

The growth rate can be obtained by the application of the Gibbs-Thomson equation (considering only first-order terms) which relates the equilibrium concentration of the particle with radius r_i (C_i) with the equilibrium concentration at the flat surface or bulk solubility (C_∞):

$$C_i = C_\infty exp(\frac{2\gamma v_c}{RTr_i}) \approx C_\infty(1 + \frac{2\gamma v_c}{RTr_i}), \tag{3.14}$$

and solving equations (3.12) and (3.14) with appropriate boundary conditions. The solution for the growth rate law for the mean particle radius, r, is then

$$r^3 = r_o^3 + \frac{8\gamma D v_c^2 C_\infty}{9RT} t. \tag{3.15}$$

The last step in the particle synthesis is the termination of the particle growth. This can be achieved either by the presence of a net charge on the surface of the nanoparticles, or by capping the particle surface with ligands that would prevent the successful addition of monomers [104]. Electrostatic repulsion between particles that carry the same charge or are surrounded by an electric double layer is frequent in polar solvents, where the ionic species in the solution can adsorb onto the particle surface, or by dissociation of the surface ions into the medium. This method of particle stabilization is only effective in low ionic strength solutions. An alternative method of particle stabilization, which also imparts desired functionality, is by use of capping ligands. The particles are capped with protective ligands by adsorption or covalent attachment. These ligands show a physical or chemical affinity for the nanoparticle

surface, providing a protective shell which can prevent the nanoparticle aggregation or precursor incorporation by steric repulsion. This method of stabilization is in general insensitive to the presence of electrolytes, and thus very desirable for use in biologically relevant environments.

3.3 Parameters Affecting ZnO Synthesis

A widely used method of zinc oxide synthesis is the hydrolysis of Zn^{+2} salts in a basic alcoholic solution. In general, the overall reaction for the nucleation of a zinc salt can be described by the reaction: $ZnX_2 + 2YOH \rightarrow ZnO_{(s)} + 2Y^+ + 2X^- + H_2O$, where X represents the anion, and Y the base cation [90]. To gain a better understanding of the parameters that influence the physicochemical properties of zinc oxide nanocrystals, many studies have been reported analyzing the effects of solvent, anion composition, zinc ion concentration, water content, synthesis temperature and capping agent on the size, morphology, and optical properties of nanocrystals. In general, hydrothermal synthesis of ZnO, where water hydrolyzes the zinc salts, results in rapid formation of large particles. The rate of ZnO growth is slowed down, in solvothermal synthesis, performed usually in an n-alkanol or polyol solution. Hu et al. have reported the importance of solvent choice in the synthesis of stable, size-tuned, colloidal zinc oxide nanocrystals. For a series of n-alkanols, they demonstrate that the nucleation mechanisms is independent on the solvent, while the diffusion-limited growth rate of nanoparticles increases with increasing temperature and longer solvent chain length, due to the influence of solvent viscosity, surface energy, and bulk solubility of zinc oxide [90]. Similarly, Ayudhya et al. observed the effect of the alcohol chain length on the size and morphology of nanocrystals, while the same effect was not observed in glycol, n-alkane or aromatic solutions [101].

Li et al. have reported that the particle size of ZnO in ethylene glycol solutions scales proportionally with water content [105], while Ratkovich et al. have demonstrated that increase in the Zn^{+2}:OH^- ratio, increases the growth rate and

the nanoparticle size [106]. The influence of anion on the Ostwald ripening of ZnO nanocrystals was investigated by Hu et al., reporting that the growth rate (equation (3.15)) is decreased dependent on the anion adsorption tendency toward the ZnO surface [107].

Appropriate choice of the capping ligand is necessary for control of the nanoparticle dispersity and stability. One of the major limitations of zinc oxide nanoparticles is their poor stability in aqueous solutions, due to a high equilibrium concentration of zinc ions in water over a wide pH range [108]. Therefore, unprotected or low binding affinity ligand-coated zinc oxide nanoparticles tend to aggregate or undergo Ostwald ripening in water [89]. To address the limitations of the ZnO stability, a variety of binding ligands have been reported to enable stable aqueous dispersions of zinc oxide nanocrystals. These include ZnO surface attachment of ester compounds [108], oleic acid [109, 110], and polymers (polyether [111], poly(ethylene glycol) methyl ether methacrylate (PEG-MEMA) [87], polystyrene and polymethylmethacrylate [112]).

In the following sections, the effects of temperature, Zn^{+2}:OH^{-} ratio and the capping agent on the properties of synthesized ZnO nanoparticles are described.

3.3.1 Temperature Effects

Following the widely used Meulenkamp synthesis of zinc oxide quantum dots by hydrolysis of zinc acetate salt [89], zinc oxide nanoparticles were synthesized and analyzed as SHG nanoprobes. The schematic of the hydrolysis, condensation and nucleation processes from the zinc acetate salt is shown in figure 3.1. Zinc oxide nuclei are formed from successive hydrolysis of zinc acetate salt in the presence of lithium hydroxide monohydrate, and condensation of the hydrolyzed zinc ion complexes ($Zn(OH)_x(CH_3COOH)_{2-x}$). Ultimately, as the nuclei grow past the critical nuclei radius, they become stable nanoparticles that can continue to grow. The strong dissociative adsorption of the acetate ions to the surface of the ZnO nanoparticles [113] stabilizes the ZnO nanoparticles through electrostatic interactions.

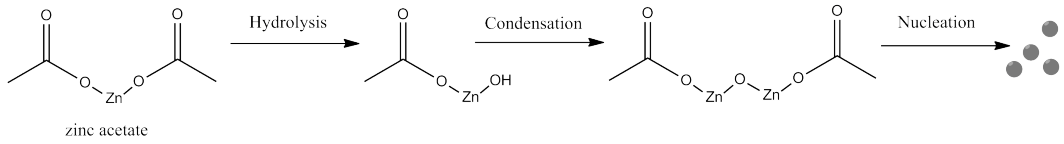

Figure 3.1: Schematic showing the hydrolysis and condensation reactions that lead to the synthesis of the ZnO nuclei. Acetate ions strongly chelate to the Zn^{+2} ions and are hydrolyzed by the LiOH base present in the solution. Successive condensation of hydrolyzed zinc complexes leads to formation of ZnO nuclei and ultimately stable ZnO nanoparticles.

According to the Meulenkamp synthesis of zinc oxide quantum dots, 5 mmol zinc acetate dihydrate was dissolved in 50 mL boiling absolute ethanol. Upon dissolution, the solution was cooled to 0°C in an ice bath. The 0°C cooled 7 mmol of lithium hydroxide monohydrate in 50 mL of ethanol, which was fully dissolved under sonication at room temperature, was added dropwise to the zinc acetate solution and stored at 4°C overnight. To eliminate the excess ions, the solution of ZnO was washed with heptane in a 2:1 (v/v) ratio. The solution was decanted and washed further with a series of heptane/hexane washes. The washed product was resuspended in 50 mL of ethanol by sonication.

Size and morphology of the nanoparticles was analyzed by TEM imaging, with the deposition of an aliquot of the ZnO solution onto a 200 mesh carbon-coated Cu grid. Excess solution from the grid was wicked away, and the TEM grid was set to dry at room temperature. TEM analysis shows the synthesis of spherical ZnO nanocrystals in the size range of 3 $\pm$ 1 nm (figure 3.2), which were prone to aggregation. The crystal structure of 104°C oven-dried ZnO particles was characterized using an X-ray diffractometer with Cu Kα (λ = 15418 Å) radiation (figure 3.3). The X-ray data showed peaks that were assigned to the hexagonal wurzite crystal structure (JCPDS 35-1451, $P6_3mc$ space group). The size of the ZnO crystals obtained by the TEM micrographs was in good accordance with the size estimated by the Debye-Scherrer formula of the powder XRD pattern. Taking into account the instrument line broadening of $\sim$0.04 2Θ, the crystallite size was estimated at 4.3 nm by Debye-Scherrer formula.

To investigate the synthesis temperature effects on the ZnO nanoparticles, Meu-

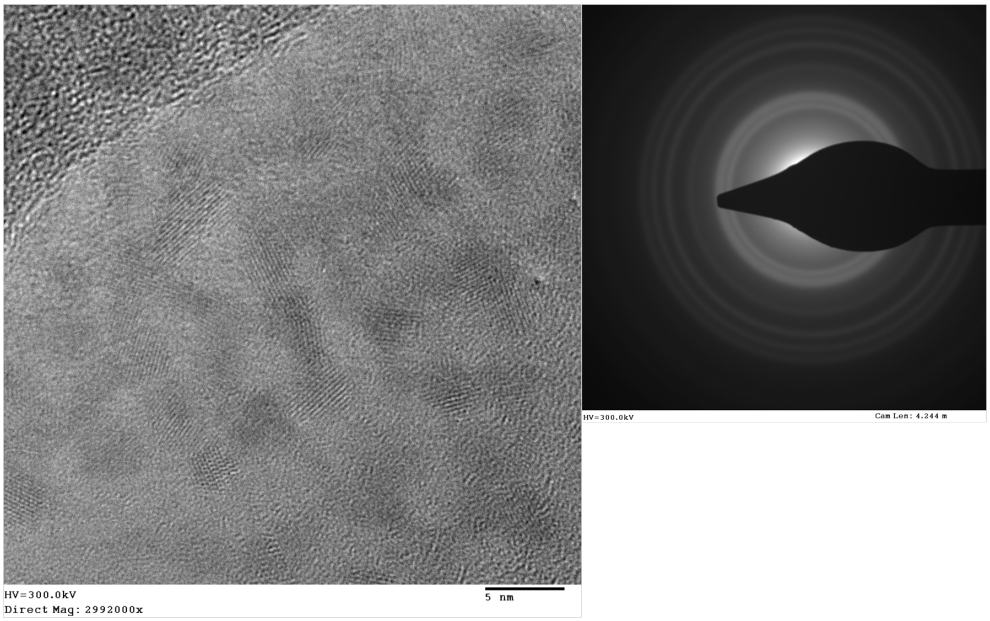

Figure 3.2: A sample of ZnO nanoparticles, syntesized according to the Meulenkamp method [89], was analyzed with TEM operated at 300kV. The particles are randomly oriented and crystalline with diameters of 3 ± 1 nm and have the hexagonal wurtzite structure. Particles are very aggregated.

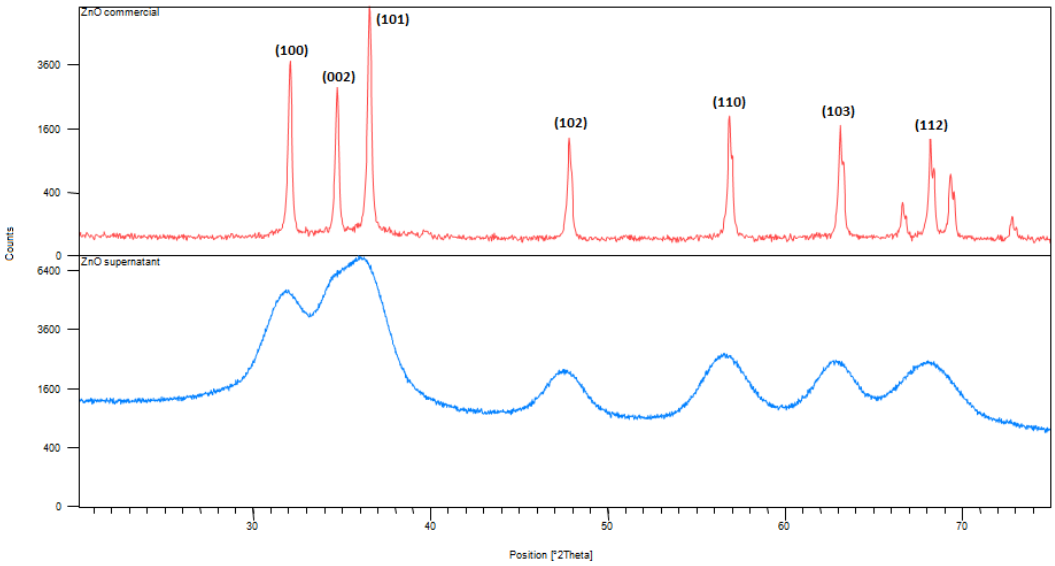

Figure 3.3: X-ray diffraction pattern recorded at room temperature of commercial ZnO particles (top), and the ZnO nanoparticles synthesized by Meleunkamp method at 0°C (bottom). The supernatant of the zinc oxide synthesis was 104°C oven dried prior to XRD analysis. Both patterns correspond to the hexagonal zincite phase (space group $P6_3mc$, JCPDS 35-1451).

lenkamp's synthesis procedure was modified, such that upon the dissolution of the zinc acetate dihydrate salt in boiling absolute ethanol, the solution was cooled either to 25°C or 50°C. Solutions were washed of excess ions, and deposited onto TEM grids for analysis. Selected area electron diffraction (SAED) analysis (figure 3.4) indicated that the crystallinity of nanoparticles synthesized at higher temperatures is improved, similar to the findings previously reported [108]. ZnO nanoparticles were dried at room temperature under vacuum in preparation for powder XRD analysis (figure 3.5). The size of the crystallites was estimated by the Debye-Scherrer formula, showing that the size of the nanoparticles slightly increases with synthesis temperature, with average crystallite size of 4.4 nm for 25°C synthesis temperature and 4.6 nm at 50°C. These observations are in accordance to previously reported temperature effects on the crystallite average size [108].

3.3.2 Capping Agent Influence

Efforts to synthesize monodisperse ZnO nanoparticles, were not achieved by the modified Meulenkamp method. Acetate stabilized zinc oxide nanoparticles were in the desired size range, but very aggregated, as demonstrated in figures 3.2 and 3.4. In an attempt to synthesize well dispersed ZnO, oleic acid, a common surfactant for dispersion of nanoparticles, was utilized. Modifications to the procedure reported by Ge et al. [114] were made, raising the synthesis temperature to 50°C in order to enhanced the nanoparticle crystallinity. The zinc acetate dihydrate (50 mM) was dissolved in 80 mL of ethanol heated to 70°C to which 50 mM solution of lithium hydroxide monohydrate in 80 mL of ethanol at room temperature was added. The solution was stirred for 1 hr at 50°C in an oil bath. Upon sonication, 0.25 mL of oleic acid was added dropwise and sonicated for an additional 2 min. The solid sediment, ZnO-OA, was washed by centrifugation with ethanol, acetone and water. Samples of the solution were deposited on 200 mesh carbon-coated Cu TEM grids. As expected, ZnO nanoparticles did exhibit a greater dispersity when capped with a longer chain

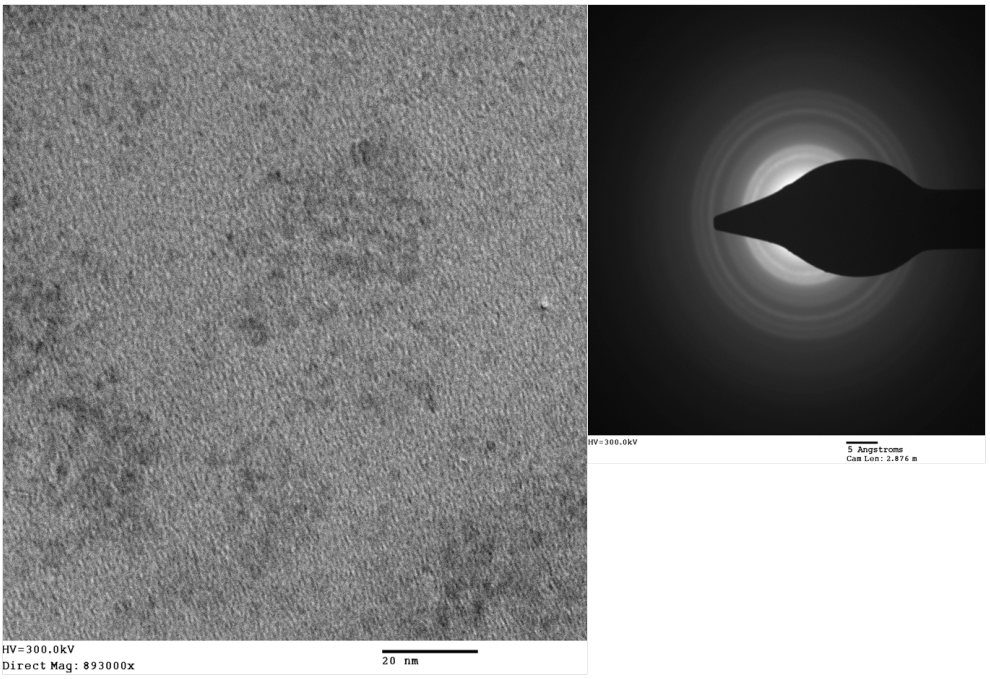

(a) Synthesis temperature 25°C

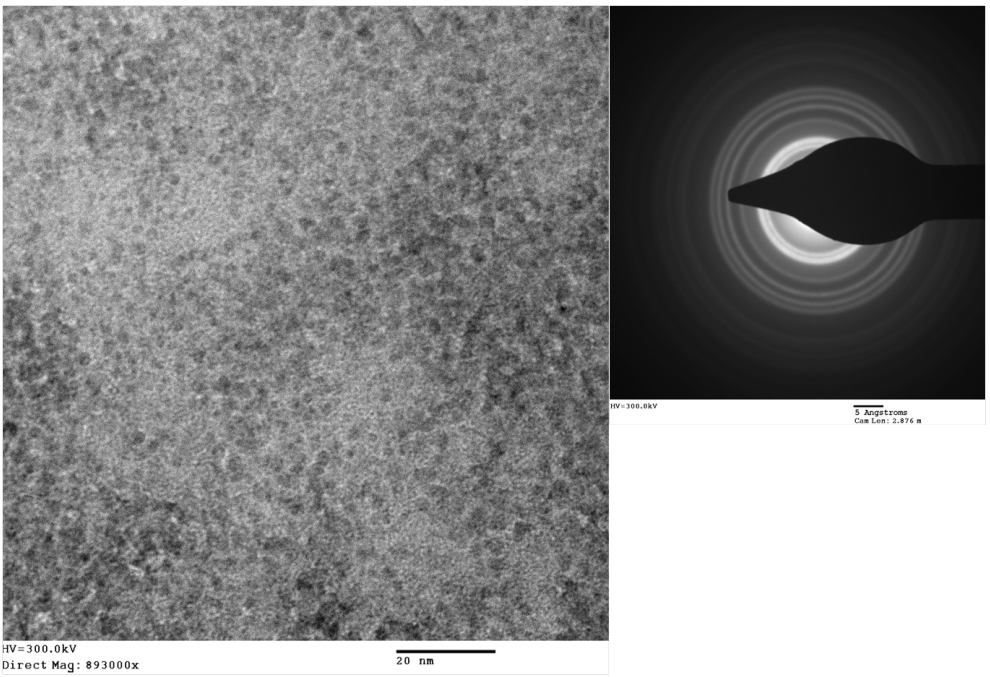

(b) Synthesis temperature 50°C

Figure 3.4: TEM images (left) of the sub-5nm ZnO nanoparticles synthesized at a) 25°C and b) 50°C. The respective SAED patterns (right), indicate improved crystallinity of nanoparticles synthesized at higher temperature. The TEM was operated at 300 kV by C. Garland.

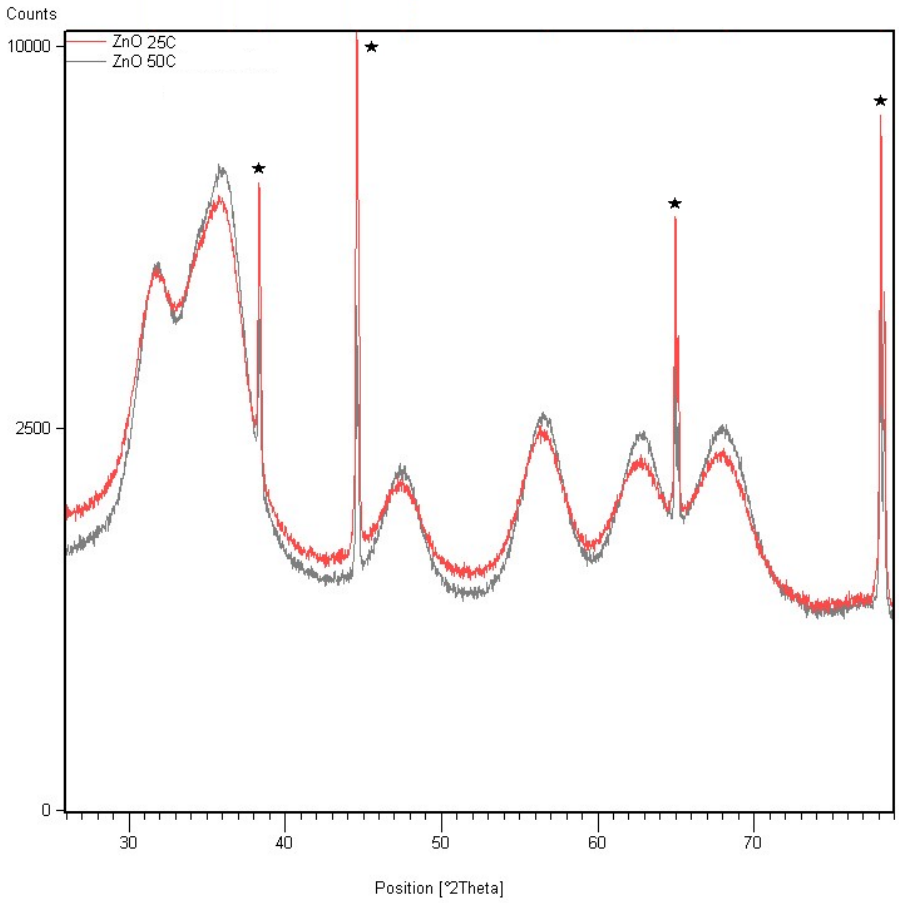

Figure 3.5: Powder XRD patterns of dried ZnO samples synthesized at 25°C (red) and 50°C (gray) temperatures. Most of the 2ϑ peaks were assigned to the hexagonal zincite phase (P63mc space group), while the sharp peaks, indicated with the star, correspond to the unwashed excess zinc acetate (JCPDS 33-1464, C2/c space group).

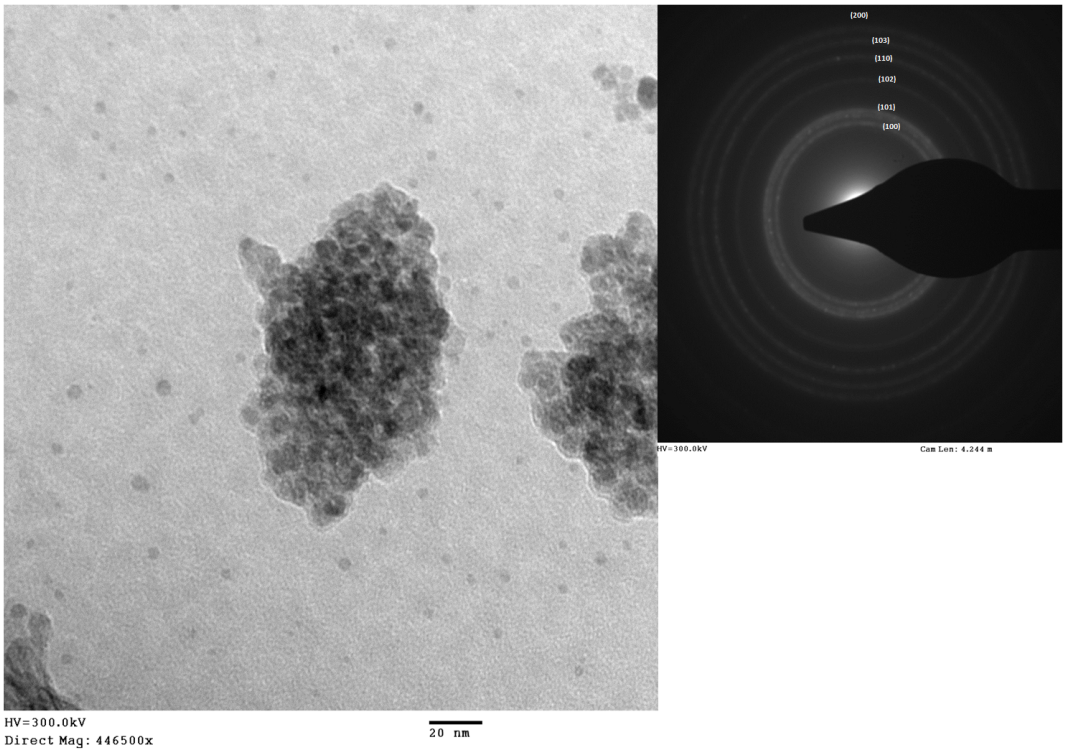

Figure 3.6: TEM images of oleic acid-coated ZnO nanocrystals raging in size from 3 to 7 nm. Oleic acid-coated ZnO nanoparticles exhibit improved dispersion as compated to the acetic acid-coated ZnO nnocrystals, but large aggregates of primary crystallites are still present in the solution. From the SAED pattern, the assignment of the ZnO (200), (103), (110), (102), (101), (100) of hexagonal wurzite structure is determined.

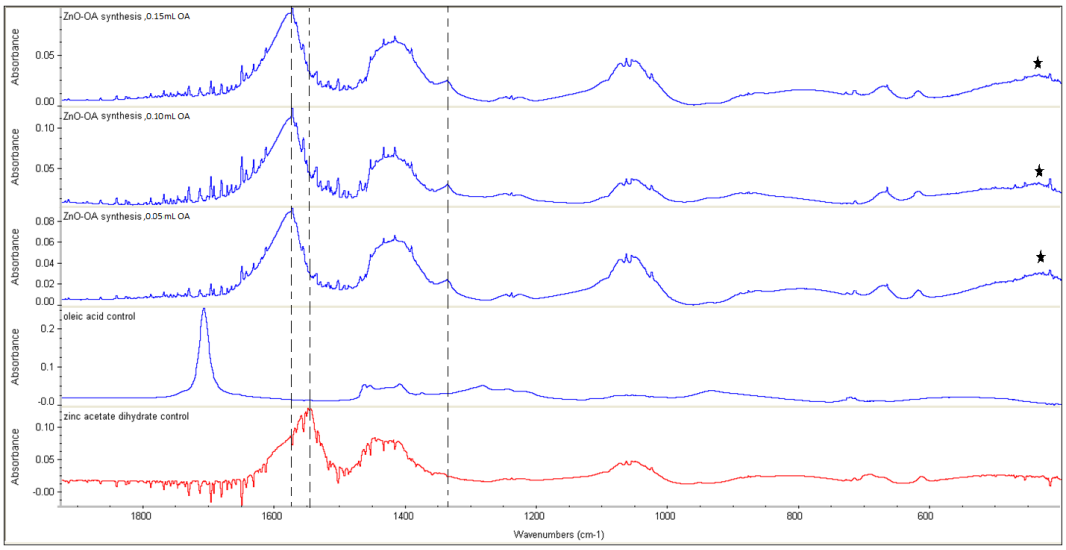

Figure 3.7: FT-IR spectra of ZnO-OA nanoparticles (top 3 spectra) with varying amounts of oleic acid used during the synthesis (0.15, 0.10 and 0.05 mL, respectively). Comparing the FT-IR spectra of the reagents, oleic acid and zinc acetate dihydrate salt (bottom 2 spectra, respectively), the differences in the absorption frequencies between the ZnO-OA samples and precursor reagents are assisted by visualizing the dotted lines. The Zn-O vibrations, indicated by *, at 450 cm^{-1} are only present in the ZnO-OA samples. The free oleic acid C=O peak at 1700 cm^{-1} is not detected in the oleic acid capped samples, indicating that the presence of the C=O stretching peak at 1575 cm^{-1} is due to the oleic acid being bound to the ZnO surface.

capping agent (figure 3.6), as compared with the acetate stabilized ZnO. However, both samples contained large aggregate structures of primary ZnO crystallites. The crystallites were assigned hexagonal wurzite structure from the d-spacings in the SAED pattern of 2.83, 2.51, 1.92, 1.62, 1.49 and 1.39 Å, which are consistent with the (100), (101), (102), (110), (103) and (200) reflections.

FT-IR analysis on the washed, and 50°C, vacuum dried ZnO-OA particles, indicates that the oleic acid is bonded to the ZnO surface. As seen from the FT-IR spectra (figure 3.7) of washed and dried ZnO-OA samples, with varying amounts of oleic acid added (0.15, 0.10 and 0.05 mL respectively from the top down), the peaks are attributed to: Zn-O vibrations (450 cm^{-1}), COO-Zn stretching (1575 cm^{-1}) [115], while the C=O stretching of free oleic acid (1700 cm^{-1})[109, 110] was not detected. Despite the improved dispersity of ZnO-OA nanoparticles, as compared to the acetate ion stabilized zinc oxide (figure 3.2), the dispersion of such capped particles is limited

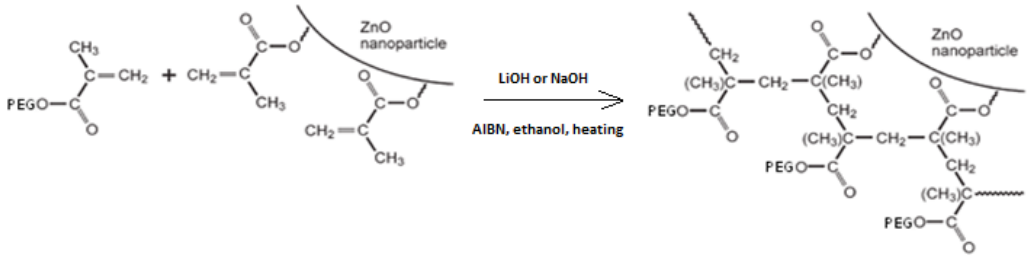

Figure 3.8: Schematic representation of the radical living polymerization of PEG-MEMA monomers on the surface of ZnO nanoparticle capped with MMA in the presence of AIBN initiator. (The source of the image is [112].)

to hydrophobic environments, which is not desirable for most biological applications.

To address the need for a water soluble capping agent which would strongly bind to the ZnO surface, a synthesis reported by Xiong et al. [87, 116] by utilizing a biocompatible, FDA approved, PEG polymers was applied. The general method of the synthesis of PEG-coated ZnO nanoparticles (PEG-ZnO) is by hydrolysis of zinc methacrylate with lithium hydroxide in the presence of 2,2-azobisisobutyronitrile (AIBN) and PEG methyl ether methacrylate (PEG-MEMA, $M_n = 475$). The schematic of the surface reaction is illustrated in figure 3.8.

Experimentally, 0.1 M zinc methacrylate (Zn-MAA) solution in 10 mL of ethanol, and 0.14 M lithium hydroxide monohydrate solution with 27 mg AIBN in 10 mL ethanol were prepared. To the Zn-MAA solution, 27 mg of AIBN and 1.5 mL PEG-MEMA were added and vigorously stirred for 2 min at 80°C in an oil bath. The hydroxide solution was added to the flask and allowed to stir under reflux for 1 hr. The solution was then allowed to cool to room temperature and dialyzed against water for a number of days using a 12-14 kDa regenerated cellulose membranes. Modifications to the synthesis were also made by increasing the concentration of Zn^{+2} ions with the addition of zinc chloride or by reduction of the PEG-MEMA that was introduced into the solution. Samples were imaged by TEM, by depositing an aliquot of the solution onto a 200 mesh carbon-coated Cu TEM grids. The solutions were transparent and no visible precipitate was observed. figure 3.9 demonstrates that the method proposed by Xiong et al. is a reproducible method for the synthesis of well-dispersed zinc oxide nanoparticles with a narrow size distribution.

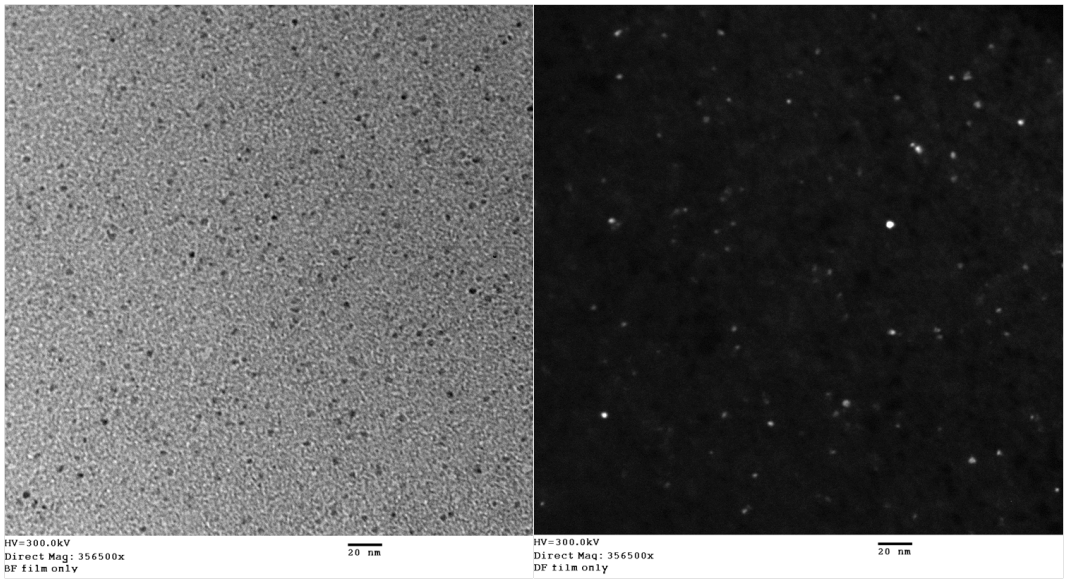

(a) Bright field (left) and dark field (right) TEM images of ZnO-PEG nanoparticles

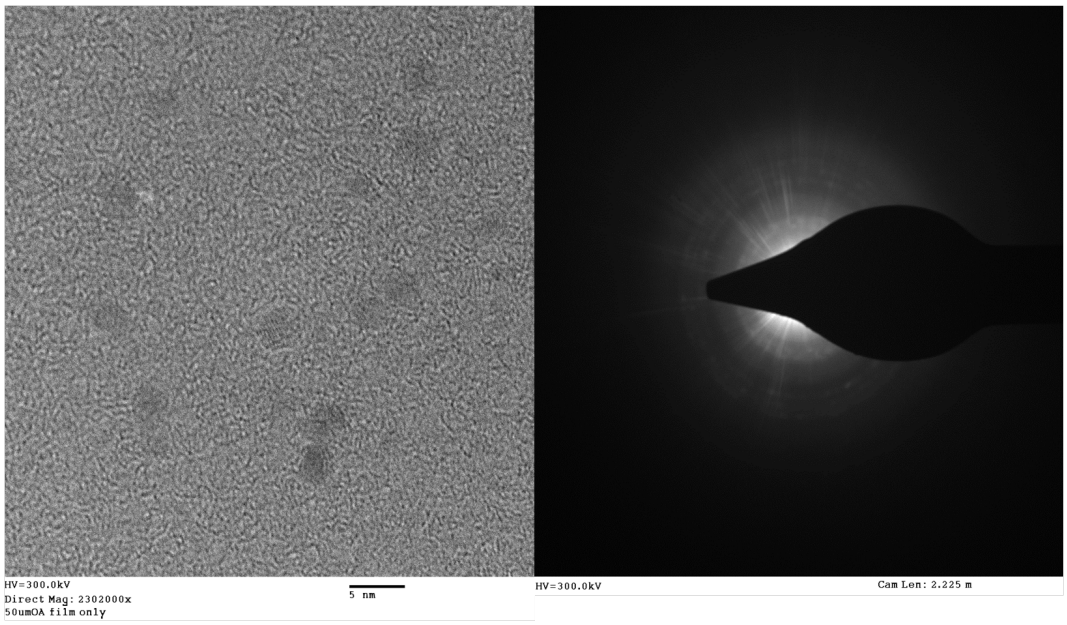

(b) HR-TEM image of the ZnO-PEG nanoparticles and SAED pattern

Figure 3.9: a) Bright-field and dark-field images of ZnO-PEG sample (with 0.1 M $ZnCl_2$ added) show that the particles are well dispersed and with a narrow size distribution range from 2 to 4 nm. b) The HR-TEM image and the SAED pattern demonstrate that the nanoparticles are crystalline in with hexagonal crystal structure.

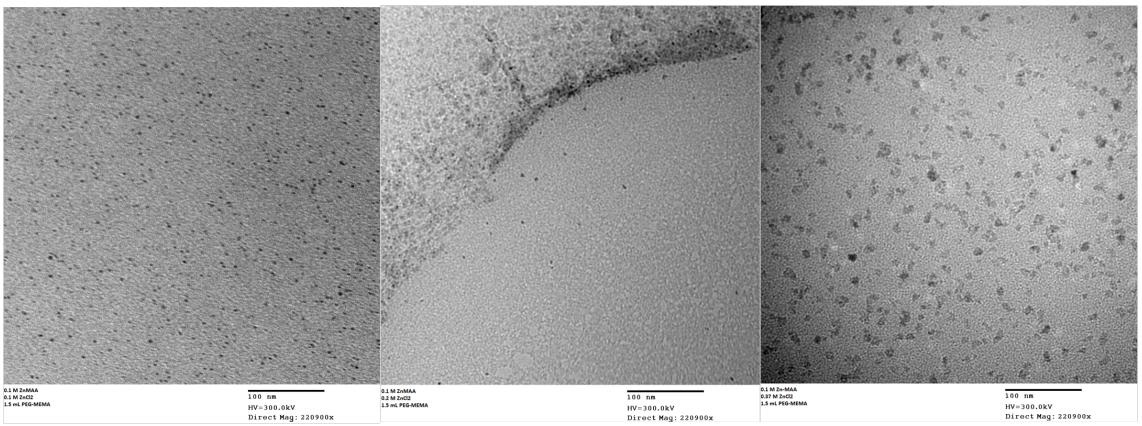

Figure 3.10: TEM micrographs of ZnO solutions with varying concentrations of zinc chloride added: 0.1 (left), 0.2 (middle) and 0.37 M (right). As the ratio of Zn^{+2}:OH^{-} increases, so does the particle size.

3.3.3 Concentration of Zinc Ions and PEG-MEMA Monomer Effects

Expanding on the Xiong et al.method of synthesis of water stable ZnO-PEG nanoparticles [112], the effects of the concentration of zinc ions and the amount of PEG-MEMA monomer on the properties of ZnO nanoparicles were investigated by TEM. In general, the size of the nanocrystals increases with increasing amounts of zinc ions present in the solution, and with the decreasing amount of PEG-MEMA monomer added. All the samples were synthesized according to the method described in the previous section, with the modification only in the amounts of precursors that were added.

Zinc chloride salt was chosen as the source of zinc ions, as it has a higher solubility as compared to zinc acetate or zinc nitrate salts. In separate experiments, 0.1, 0.2, and 0.37 M of zinc chloride were added to the 0.1 M zinc methacrylate salt solutions with 1.5 mL of PEG-MEMA added. Analyzing the solutions on the TEM, an increase in the size of the nanoparticles is observed as the Zn^{+2} concentration is increased to 0.47 M Zn^{+2}. Additionally, the morphology of the particles with the highest concentration of Zn^{+2} ions present in the solution changes to a less spherical shape.

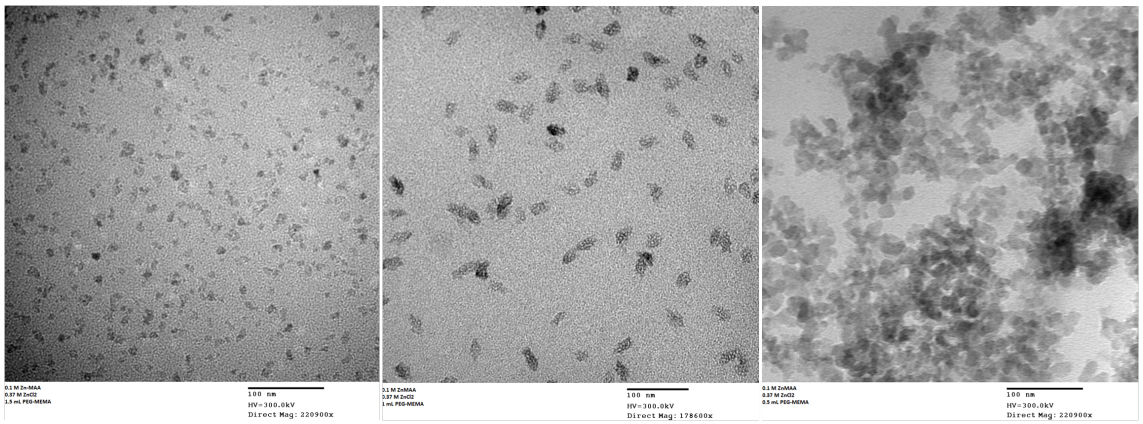

Figure 3.11: TEM micrographs of the ZnO ethanolic solutions, where 0.1 M Zn-MAA and 0.37 M $ZnCl_2$ are reacted in the presence of 0.14 M LiOH in the presence of AIBN at 80°C with decreasing amounts of PEG-MEMA monomer added: 1.5 mL (left panel), 1.0 mL (middle panel) and 0.5 mL (right panel).

In order to investigate the effect that decrease in the amount of added PEG-MEMA has on the size and morphology of the nanoparticles, three experimental conditions were analyzed. The total concentration of Zn^{+2} ions was kept constant at 0.47 M, and varying amounts of PEG-MEMA monomer were added, ranging from 1.5, 1 and 0.5 mL. Investigation by TEM indicates that the size and the morphology of the crystals changes (figure 3.11). The size of the primary crystallites was similar ($\sim$10 nm), but the occurrence of aggregated, secondary structures increased with decreasing amount of the PEG-MEMA. In the sample with the least amount of PEG monomer added, in addition to well dispersed ZnO-PEG particles some aggregation of particles was observed (figure 3.11 right panel), similar to the results obtained for ZnO nanocrystals synthesized by the Meulenkamp method.

This can be explained by the mechanism of growth of the ZnO-PEG nanoparticles as reported by Xiong [32] in comparison with the classical sol-gel method reported by Meulenkamp [89] (figure 3.12). The mechanism of ZnO nanoparticle formation by the Meulenkamp's method is by the hydrolysis of zinc salt precursor and their subsequent condensation into nuclei large enough to be stable for continued growth. As the stabilizing ligand on the surface of ZnO are acetate ions, over the course of time, they dynamically bind and unbind from the nanoparticle surface, allowing the

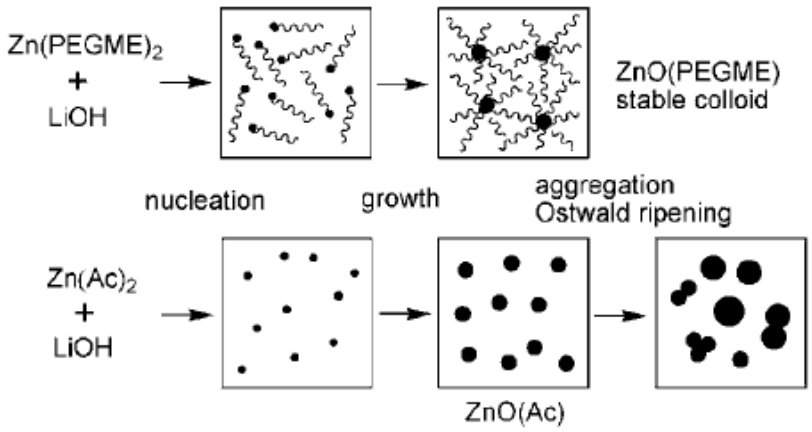

Figure 3.12: Schematic representation of the difference in the mechanisms of ZnO nanoparticle formation by the Xiong method (top) and the Meulenkamp method (bottom). (Source of the schematic is [32].)

nanoparticles to continually grow/aggregate at the expense of the smaller particles following the Ostwald ripening law.

In contrast, the mechanism of ZnO nanoparticle formation by the Xiong method involves nucleation of PEG-MEMA polymerized ZnO. Subsequent growth of these PEG-ZnO nuclei leads to a formation of tightly polymer bound ZnO-PEG nanoparticles. Therefore, in systems where the amount of zinc methacrylate and PEG-MEMA monomer are optimized, the tightly bound polymer shell will prevent the from particle aggregation. However, if the PEG-MEMA and ZnO-MAA amounts are not balanced, particles will aggregate and precipitate out.

Therefore, decrease in the amount of PEG-MEMA monomer in the presence of zinc chloride and zinc methacrylate salts leads to a smaller amount of PEG- ZnO nuclei that ultimately leads to fewer and smaller ZnO-PEG particles. However, the zinc chloride can also hydrolyze in the presence of lithium hydroxide (similar to the Meulenkamp method) and potentially interact with the properly polymerized PEG-ZnO nuclei to form well-dispersed, polymer bound, irregular shaped aggregates of zinc oxide. And example of this aggregation is see in the HR-TEM micrograph (figure 3.13) of an aggregated particle that is well dispersed (no other crystalline particles surround it). The orientation of the primary crystallites can be see from the lattice fringes,

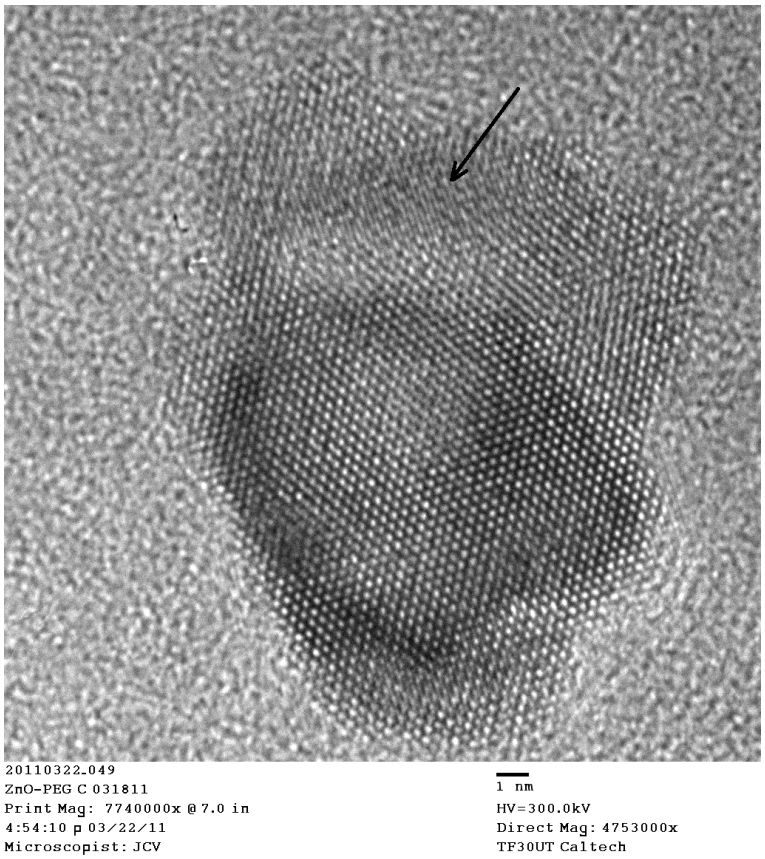

Figure 3.13: HR-TEM micrograph of a well-coated ZnO-PEG nanoparticle, which is an aggegate of differently oriented primary crystallites. Note the arrow pointing to the crystal that is differently oriented than the crystal in the foreground.

where the area marked with the arrow indicates the crystal oriented differently from the crystal seen in the foreground. Similarly, a series of dark-field images (figure 3.14) were collected at different diffraction conditions, such that the diffraction intensity is obtained coming from only a select diffraction plane, providing insight into the crystal orientation.

Therefore, the monodispersity of the PEG-coated ZnO nanoparticles is a a function of both the concentration of the Zn-MAA precursor, as well as the amount of PEG-MEMA. If the concentration of the zinc methacrylate salt is increased, the polymerization between the adjacent precursor molecules can lead to the formation of an network of ZnO particles crosslinked together, as seen on figure 3.15, where 0.3 M zinc methacrylate concentration was reacted with 1.5 mL PEG-MEMA, without the

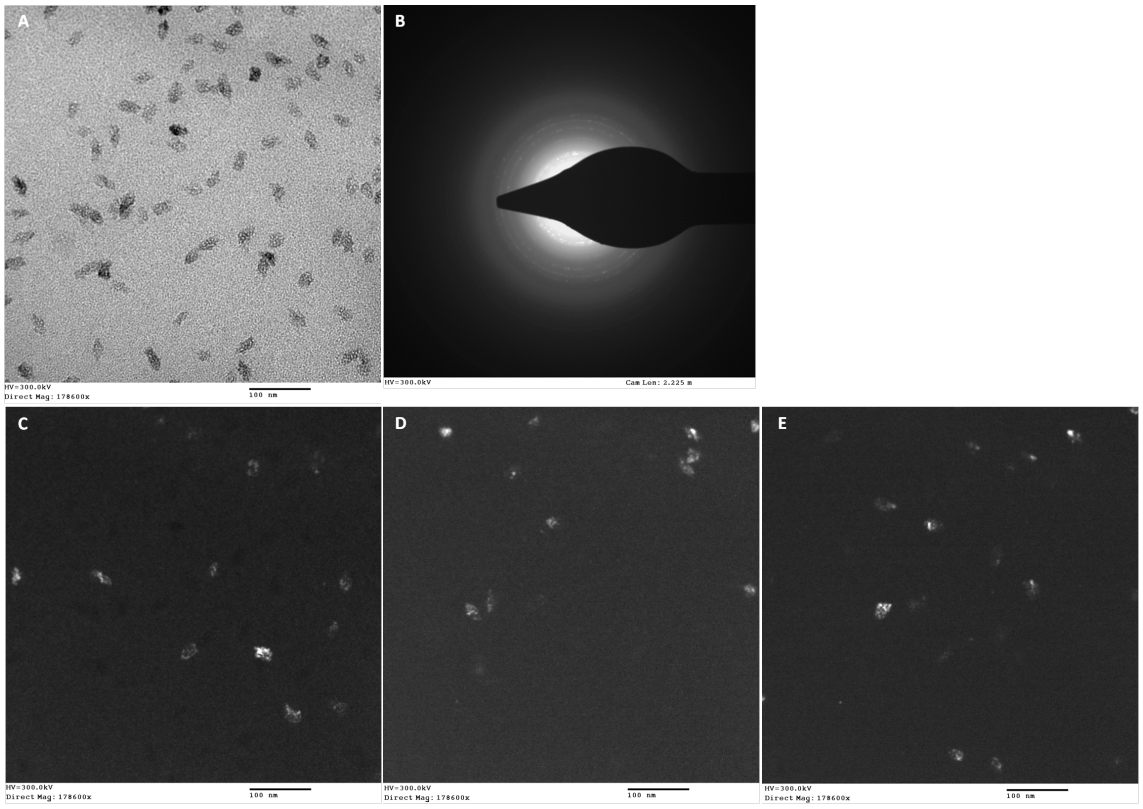

Figure 3.14: TEM micrographs comparing the diffraction intensity at select diffraction planes of the particles inaged in bright field (A). The SAED pattern confirms crystal wurzite structure (B), darf field images with: the $1^{st}$and 2^{nd} diffraction rings (C), 3^{rd} and 4^{th} diffraction ring (D), and 5^{th} and 6^{th} diffraction rings selected (E).

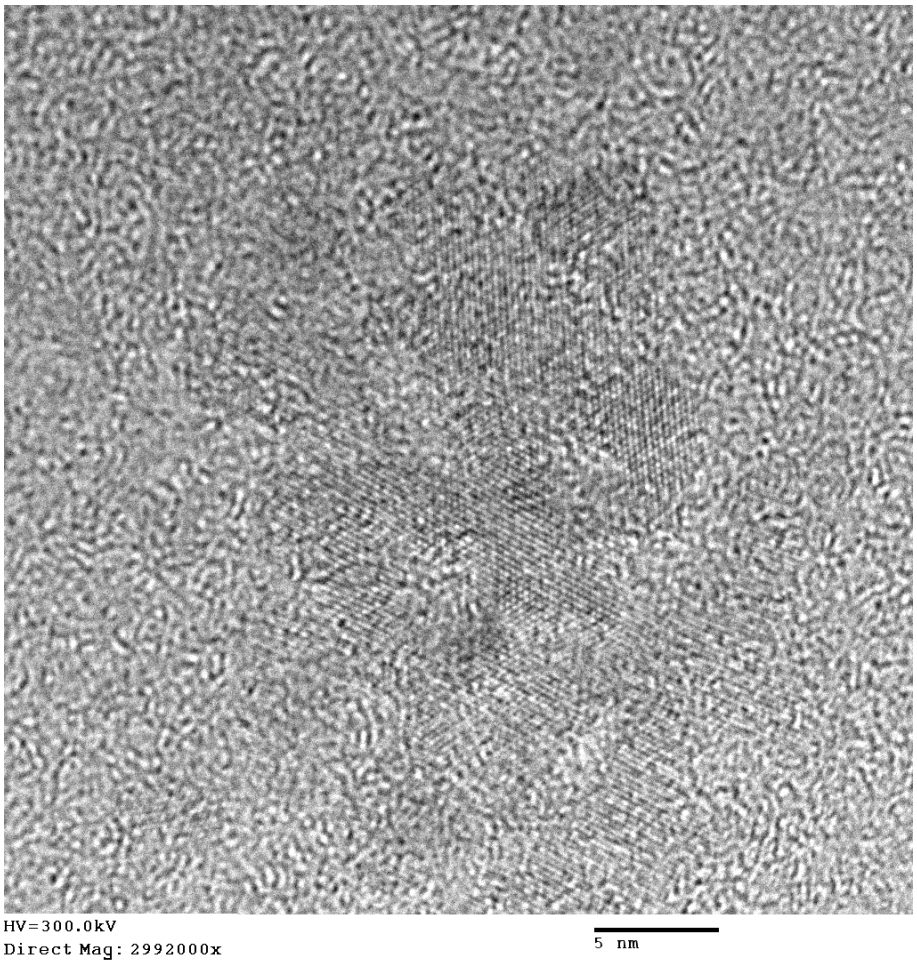

Figure 3.15: HR-TEM micrograph of the intercrosslinking ZnO nanoparticles.

addition of any zinc chloride.

The size of the crystals is dependent on the rate of nucleation, which can be controlled by the Zn^{+2}:OH^{-} ratio. For smaller Zn^{+2}:OH^{-} ratios, the crystal sizes will be even smaller as the hydrolysis of the precursor would take place at a greater rate [117]. However, for larger Zn^{+2}:OH^{-} ratios, the amount of PEG-MEMA monomer needs to be optimized, to avoid particle cross-linking by the polymerization of the methacrylate ligands on the surface of ZnO.

3.4 SHG Signal Efficiency

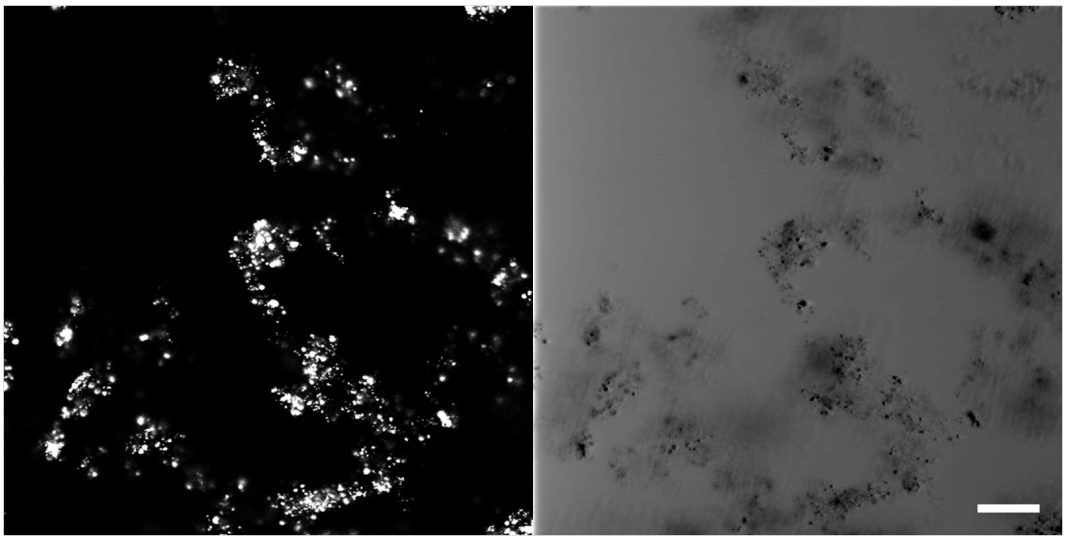

Figure 3.16: ZnO-PEG nanoparticles, synthesized by Xiong method (0.1 M Zn-MAA in presence of 1 mL PEG-MEMA and 0.37 M of zinc chloride), were imaged by LSM 710 microscope with 800 nm laser light. At the bottom of the coverslip, only aggregated particles show SHG signal (left). Merge of the bright field and SHG signal (right). Scale bar: 50 μm.

The main objective of this work, was the synthesis of monodisperse ZnO nanoparticles with sizes less than 10 nm, such that they are comparable in size to the biological structures and fluorescent probes. The solutions of ZnO nanoparticles were analyzed for the presence of SHG signal, using the LSM 710 (Carl Zeiss AG) microscope with 2-photon capabilities (Chameleon Ultra II, Coherent). As the size of the nanoparticles is very small, it was expected that the SHG signal sensitivity would be decreased from those of bulk crystals. Unfortunately, from the current setup of the LSM 710 microscope that was used, only the signals of aggregated samples at the coverslip were detectable.

3.5 Conclusion

For imaging of highly absorbing and scattering biological samples, second harmonic generation is utilized, due to enhanced signal properties compared to fluorescent probes or quantum dots. Currently, the biological imaging applications of SHG

nanoprobes have been limited to commercially available nanopowders with wide size distributions. Such samples do not have uniform chemical and physical properties, and are limited in their application for single molecule analysis of protein targeting. Therefore, to address these limitations, the synthesis of sub-10 nm SHG nanoprobes of hexagonal zinc oxide SHG nanoprobes of was attempted.

Zinc oxide is a cheap, widely used, nontoxic material, with established synthesis procedures as quantum dots. Most commonly, these procedures are performed by solvothermal methods, where a zinc salt is hydrolyzed by a basic solution, and upon condensation of the hydrolyzed precursor, ZnO nuclei are formed and continue to grow. Particle growth is terminated upon either efficient capping of the surface of the particle with strongly bound ligands or when the equilibrium solubility concentration is achieved. Without the strongly bound capping ligands, particles will continue to grow, at the expense of smaller particles, according to the Ostwald ripening rate law [89, 32].

In order to control the size and morphology of nanoparticles, it is important to understand the parameters that govern their growth. In this work, a variety of chemical synthesis procedures were investigated and evaluated based on the properties of the synthesized zinc oxide nanoparticles. An increase in the synthesis temperature leads to greater crystallinity of the nanoparticles, due to the monomers having more energy to attach or migrate to energetically more favorable positions. Synthesis temperature increase also lead to larger primary crystallite sizes, due to the effects of solvent viscosity and solubility of zinc oxide. At higher temperatures, the viscosity of the solvent decreases and the diffusion constant of the monomer increases. Thus, it takes less time for the monomer to diffuse to the particle surface. In addition, the solubility of zinc oxide increases at higher temperatures and the rate of dissolution of smaller particles is greater. Thus, larger particles will grow at the expense of smaller ones.

A very important parameter for the synthesis of zinc oxide nanoparticles is the ratio of the base to the zinc salts. At lower Zn^{+2}:OH^{-} ratios, the hydrolysis rate is increased, which leads to formation of smaller particles. As the Zn^{+2}:OH^{-} ratios

increases, larger particles can be formed as more zinc precursor is available for the continued growth of the particles. However, the main distinction between the synthesis procedures that were investigated was the capping agent. Small ligand molecules (i.e., acetate) have a strong affinity for the polar surface of ZnO, but due to the electrostatic nature of the interaction, they are not an effective ligand to use for long-term stability in biological aqueous solutions which have a higher ionic strength. Oleic acid has a longer hydrophobic chain, as compared to acetate, leads to the formation of particles that are better dispersed that the acetate-capped ZnO nanoparticles are, but in addition from not being able to completely eliminate the aggregation of particles, they also are not easily dispersed in aqueous solutions.

Therefore, for a well-dispersed solution of zinc oxide nanoparticles, one should use longer chain ligands that are amphiphilic and provide long-term stability to the particles. One such system was the synthesis of PEG-coated ZnO nanoparticles [32], where the protective PEG shell is achieved by poymerization of PEG-MEMA monomers with the zinc methacrylate salts and their subsequent hydrolysis in a basic solution to form ZnO-PEG nanocrystals. The PEG coating is tightly bound to the surface of nanoparticles and provides a biocompatible shell that sterically shields the surface of ZnO from aggregation.

However, aggregation can still be detected when the PEG coating is not complete, which would be the case if insufficient amounts of PEG-MEMA are reacted with zinc methacrylates. Similar effects are observed if the concentration of zinc methacrylates is increased, leading to a network of crosslinked of zinc methacrylate species. Aggregate formation, as well as nonspherical morphology of the particles, was also observed when the concentration of zinc species was increased by the addition of zinc chloride. Therefore, careful control of the synthesis conditions and optimization of the amount and type of capping ligand to the zinc precursor are paramount for the synthesis of monodisperse, size-controlled nanoparticles.

Chapter 4

Conclusion and Future Outlook

To understand the way organisms develop, to see how they are organized at the cellular level, to track the progress of therapeutics or the location of a specific biological target in a noninvasive manner, light microscopy is a powerful tool. However, imaging of biological samples is a challenging task, as biological tissues absorb and scatter light, especially in the visible range. Therefore, by exciting imaging probes with low energy NIR light, the signal loss is minimized, due to minimal absorption and scattering of tissues in the 650-900 nm range, allowing for deeper penetration. Many imaging probes are available, with fluorescent probes being some of the most commonly used. Unfortunately, fluorescent probes are limited in the scope of their application, due to the phenomena of dye bleaching, blinking, phototoxicity and signal saturation.

To address the limitations of fluorescent probes, second harmonic generation can be utilized. As SHG is dependent on the scattering of the illuminating light, the SHG signal is stable over time, allowing for long-term imaging, and is easily utilized with NIR two-photon light to generate strong signal. However, only noncentrosymmetric materials are able to generate SHG signal. Endogenous SHG signal can be obtained from macroscopic structures in the organism (e.g., collagen, etc.), but for imaging on the cellular level, or for tracking of a single molecule, exogenous SHG probes need to be used. Exogenous SHG probes are nanocrystals that have a very strong SHG signal (large second-order susceptibility value), some of of which are barium titanate

and zinc oxide.

In order to utilize these inorganic crystals in biological applications, they need to be made biocompatible, stable in aqueous solutions, and functionalized for desired application. To achieve this, these SHG nanocrystals can be functionalized with a variety of biological molecules, imparting them with the desired properties. In this dissertation, was demonstrated, on the example of commercial barium titanate nanoparticles, the potential routes of chemically modifying the surface of SHG nanoprobes for biological applications. First, the surface hydroxyl groups were reacted with N-aminoethyl-2,2,4-trimethyl-1-aza-2-silacyclopentane to exposed amine functional groups along the surface. This amine platform allows for a variety of further chemical modifications to take place, some of which have been demonstrated here: nonfunctional coating amphiphilic PEG polymer, attachment of biotin moieties, attachment with antibodies for specific targeting of receptors, and attachment of fluorescent probes for a novel NIR imaging tool. These protocols should be adaptable to other SHG nanoprobes that have exposed hydroxyl groups on their surface.

However, one limitation of the use of commercial powders of SHG nanoprobes is their inherent polydispersity and aggregation. To address these issue, a synthesis of monodisperse, sub-10 nm zinc oxide particles was investigated. Utilizing solvothermal methods of zinc oxide synthesis, it was demonstrated that for monodisperse nanoparticle synthesis, the choice of the capping agent is paramount. Utilizing the long chain poly(ethylene glycol) methyl ether methacrylate polymer to polymerize with the methacrylate ligands present on the surface of ZnO nanoparticles, a protective amphiphilic shell was formed. This protective coating makes the particle stable in biological aqueous solutions and has the potential to prolong their circulation *in vivo* applications.

The detection of SHG signal from such small nanoparticles, utilizing the available microscope setups, was challenging. The SHG signal was clearly visible in aggregate formations, which were formed under the conditions of less-than-optimal precursor concentrations. However, SHG signal was not readily detectable in monodisperse ZnO nanoparticles with diameters less than 10 nm. To address this limitation, a possible

method of resonance enhancement of the SHG signal, by gold capping of the surface should be considered. Resonance enhancement of the SHG signal can be achieved by formation of a thin shell of gold around the ZnO nanoparticles [118, 40]. The outside gold shell coating could easily be functionalized with thiol functional molecules for a desired target. The application of such small nanoparticles that exhibit detectable SHG signal, would be ideal for many applications, for cellular and protein tracking, membrane voltage-sensitive SHG imaging, etc.

Coating of the SHG nanoprobe surface with fluorescent dyes, as demonstrated for commercial barium titanate nanoparticles with corroles, would enable energy transfer from the SHG probe to the fluorescent dye. The advantage of this novel imaging probe is that both the illuminating and emitted light are in the NIR range, allowing for minimal signal loss and deeper penetration of the signal. The specificity of the donor role of the SHG nanoprobe lies in the fact that as a scattering process, the illumination light frequency can be tuned easily. Thus, SHG probes can be coated with corroles that exhibit different photophysical properties, to obtain a whole range of "colors". In addition to the corrole coating, the surface of the nanoprobe could be coated with targeting molecules. Therefore, easier recognition of the probe localization could be achieved by simple color comparison, when a mixture of SHG probes, each functionalized with a different corrole and functional moiety, is introduced in the system. The parameter space that could be explored is vast, from the investigation of the photophysical properties of different corroles, or the excitation efficiency as a function of linker lengths (the distance between the probe and the corrole), to their applications in biological systems. Similarly, SHG probes can be functionalized with a variety of other linkers, specifically providing multifunctionality to the nanoparticles for desired applications, as was demonstrated with transferritin and PEG coating on Au nanoparticles [51].

Noncentrosymmetric, monodisperse, inorganic nanocrystals with high second-order susceptibilities and adequate surface functionalizations have the potential for a plethora of applications in biological imaging. As this field has only recently started to develop, the SHG nanoprobes have a bright future ahead of them.

Appendix A

Materials and Methods for Barium Titanate Application in Biological Systems

A.1 Materials

• Nanoject II nanoliter injector (Drummond Scientific Company) for embryo injections

• 3.5 inch borosilicate glass capillary tubes (Drummond Scientific Company)

• Needle puller (Sutter Instrument, P-2000 Laser Based Micropipette Puller)

• Intertek Listed ultrasonic cleaner (Model: CD-4800) for nanoparticle dispersion before zygote injection

• LSM 510/710 (Carl Zeiss AG) with 2-photon capabilities (Chameleon Ultra II, Coherent) for SHG microscopy

• Equipment for raising zebrafish and maintaining zebrafish

• Zebrafish breeding tanks and equipment for collecting zebrafish embryos. Breeding tanks are plastic chambers that either have a divider that allows eggs to settle to the bottom or have marbles at the bottom of the tank to prevent fish from eating their embryos before collection

• Labtek multiwell chambered coverglass/coverslip chambers (Nunc International, #1 coverslip thickness, 2- and 8-well)

• Forceps (Student Dumont #5: Fine Science Tools)

• Hair loop (piece of hair looped and taped or glued to the end of a 2-3 mm diameter plastic or metal rod) to orient embryos

• Glass transfer pipettes/disposable Pasteur pipets (Corning)

• Petri dishes of varying size (35x10 mm Falcon Easy Grip Petri dishes: Becton, Dickinson and Company and 100x15 mm polystyrene disposable Petri dishes: VWR International LLC)

• Microscope objectives with sufficient transmittance (>80%) in the UV-VIS-IR range (Carl Zeiss AG objectives: Plan-Apochromat 20x/0.8 M27 for lower magnification applications, LD LCI Plan-Apochromat 25x/0.8 Imm Korr DIC, C-apochromat 40x/1.2NA W Corr M27 for superficial SHG imaging within the sample, or LD C-Apochromat 40x/1.1 W Korr UV-VIS-IR M27 for deeper imaging within the sample). CRITICAL STEP: The microscope objective used in experiments with SHG nanoprobes should have a wide transmittance range to allow for efficient illumination of the sample and collection of the resulting SHG signal.

• Fluorescence dissection stereomicroscope with appropriate filter sets to visualize any fluorescent labels that were introduced along with the SHG nanoprobes (Olympus America, MVX10 Macroview)

• Dissecting Microscope (Leica Microsystems, MZ9.5 modular high-performance stereomicroscope)

A.2 Methods

A.2.1 Imaging Based Confirmation of Proper Functionalization

1. Prepare a control BT solution (5 mg of BT-OH) to compare to BT-streptavidin-AF488 following the reaction of biotin-BT with streptavidin-AF488. This will act as a control for the extent of nonspecific binding of streptavidin-AF488 on nonfunction-

alized particles.

2. Flick the 1.5 mL tubes several times to redisperse any sedimented BT-streptavidin-AF488 and BT-control. Each of the solutions should be rather concentrated, so remove 10–100 µL of the supernatant from each and dilute 1:10–1:100 in 1x PBS so that the solution is milky but not completely opaque when the particles are dispersed.

3. Pipette 200–400 µL of each solution into separate wells of an 8-well coverslip chamber (#1 coverslip bottom). Note that 200 µL will be just enough for a droplet within the well, which may make focusing to the sample easier by focusing to the edge of the droplet, while 400 µL will fill the entire bottom of the well in solution.

4. Place the coverslip chamber on the stage of a confocal laser scanning microscope with 2P capabilities and a spectral scanning capability (e.g., the lambda mode in the Zeiss Zen 2009/2010 software).

5. Focus to the coverslip surface with a high numerical aperture water (since the sample is in PBS) objective at 40x magnification.

6. Using the two-photon laser (set at 820 nm, for example) at low power (∼1% in the software), scan single optical sections of the sample continuously—using a band-pass emission filter that contains the SHG peak (peak at 410 nm, in this case)—focusing up and down in the z direction until a plane is found with the most SHG signal (especially from the smallest SHG nanoprobes). CRITICAL STEP: SHG signal is narrow in spectrum, so for confocal microscopes that allow direct selection of emission wavelength ranges, choose a narrow band (5–10 nm) centered around the peak of SHG emission (e.g., 405–415 nm or 400–420 nm, when the illuminating beam is 820 nm). The choice of a narrow bandwidth filter is critical to minimize autofluorescence, especially when imaging in biological tissues.

7. Choose a 2P wavelength that will excite the dye conjugated to streptavidin. Note that regardless of the wavelength, SHG signal should be visible from the nanoprobes. For BT-streptavidin-AF488, ∼965 nm is a reasonable choice to excite the AF488 dye.

8. Prepare an appropriate light path on the microscope software to detect a wide-band of spectral information from each pixel within the image (e.g., lambda scan of a 34 channel detector in the Zeiss Zen software). Breaking up the spectral data into 10

nm increments is sufficient, since the SHG signal will be blue-shifted and spectrally separated with respect to the dye emission.

9. Take a single spectral scan of the plane of maximal SHG signal in the BT-control and the BT-streptavidin-AF488 well.

10. Observe the intensity profile of the spectral data surrounding each nanoprobe cluster within the well. The BT-streptavidin-AF488 nanoprobes should have peaks for both SHG and AF488 emission, while the BT-control will only have the SHG peak.

A.2.2 Zebrafish Zygote Stage Injections with PEG-BT

11. The night before embryo injections, set up male/female crosses in breeding tanks. Separate males from females by dividers so that the fish will not breed before the injection setup is prepared the next day.

12. Use a needle puller to prepare several injection needles made from borosilicate glass capillary tubes. Break the end of the tip off on a bias using forceps when viewing the tip of the needle under a dissection microscope. CAUTION: The glass pipettes should not have an internal fiber.

13. On the day of injection (one day after step 11), prepare PEG-BT solution for injection into zebrafish embryos. Note that depending on the application, several preparations can be attempted: PEG-BT alone (option A), PEG-BT coinjected with dye (option B), or PEG-BT coinjected with DNA encoding a fluorescent protein along with transposase mRNA (option C). PEG-BT localizes within cells of the embryo and can be tracked for any extended period of time alone. Often, it is desirable to have cell context to the localization of PEG-BT within zebrafish cells, which can be achieved by colabeling with PEG-BT using options B or C. Note that mRNA encoding a fluorescent protein may be coinjected instead of fluorescent protein DNA plus transposase mRNA, though this will not be discussed in this protocol.

(A) PEG-BT alone

(i) Sonicate PEG-BT for 1 min in a bath sonicator. Allow sedimentation of largest clusters for 2 min.

(ii) Dilute 10–50 µL supernatant of the PEG-BT in water (UltraPure) such that it is milky but not completely opaque (between 1:50 and 1:100).

(iii) Sonicate for 1 min in a bath sonicator.

(iv) Wait 2 minutes and then proceed with injections as described below.

(B) PEG-BT coinjected with dye

(i) Prepare PEG-BT as in steps (i)–(iii) in option A.

(ii) Dilute dye to proper stock concentration using manufacturer's instructions. For the case of 10,000 MW Dextran conjugated to an AF (in this case, AF546), dilute to a 0.1 mg/mL injection solution in 1x PBS.

(iii) Add 1 µL of dye injection solution into 4 µL prepared PEG-BT solution and proceed with injections as described below.

(C) PEG-BT coinjected with fluorescent protein DNA

(i) Prepare PEG-BT as in steps (i)–(iii) in option A.

(ii) Prepare a plasmid by cloning the cDNA encoding a fluorescent protein of interest into an appropriate vector containing transposable elements flanking the coding region of the plasmid (e.g., pMTB vector). CRITICAL STEP: DNA injection will allow mosaic fluorescent protein expression within a zebrafish embryo. Tissue-specific promoter-driven expression may be used, if labeling of particular tissue types with fluorescence is of interest. Additionally, ubiquitous promoters (e.g., β-actin promoter) may be employed if cell-specific labeling is not needed.

(iii) Generate mRNA encoding the sequence for the transposase that recognizes the transposable elements in the plasmid (e.g., Tol234 for the pMTB vector) by following the manufacturers instructions on an mRNA expression kit (e.g., mMESSAGE mMACHINE from Ambion).

(iv) Combine the mRNA and DNA into a single stock solution for preparation for injection. The fluorescent protein DNA concentration should be ∼100 ng/µL and the transposase mRNA concentration should be ∼400–500 ng/µL.

(v) Add 1 µL of DNA/mRNA stock to 4 µL prepared PEG-BT solution on ice

and proceed with injections as described below.

14. It is often useful to visualize the injection into the embryo. If this is desired, ensure that the 5 µL injection solution contains 0.1%–0.3% (W/V) phenol red. A red-colored bolus of liquid containing the injection solution should be seen in the injected embryos when phenol red is used.

15. Remove dividers from the fish crosses that were set up the previous day so that they will mate. Wait 15–30 min for fish to mate before collecting embryos.

16. Prepare the injector setup (e.g., Nanoject II) so that the injection needle will be within the viewing platform of a dissection microscope, and fill pipette needle with embryo tested mineral oil before placing it on the injector itself.

17. Collect the embryos and transfer to a Petri dish filled with egg water.

18. Using a plastic transfer pipette, move the zebrafish embryos over to an agarose injection chamber. Orient the zygote stage embryos into the grooves of the injection chamber using a forceps. Note that the chamber may be made by pouring hot 1%–1.5% agarose into a Petri dish and dropping a plastic injection chamber mold (as described in the Zebrafish book) into the center of the hot agarose until the agarose solidifies. Remove as much liquid as possible from around the embryos.

19. Eject some mineral oil from the injector onto a small piece of parafilm under a dissection microscope. Pipette the 5 µL of PEG-BT solution nearby on the parafilm. Fill the needle with ∼2–5 µL of solution (depending on the number of embryos). Test that the injector ejects even (2.3 nL) amounts by injecting into the mineral oil on top of the parafilm.

20. Move the injection chamber with mounted embryos under the dissection microscope. Inject 2.3 nL of PEG-BT solution into each of the zygote stage embryos, piercing the chorion with the needle and inserting the needle into the yolk cell just beneath the developing zygote cell.

21. Transfer the injected embryos back into a Petri dish filled with egg water and move the Petri dish to a 28^0C incubator.

A.2.3 Preparation of Injected Zebrafish for Imaging

22. Zebrafish at different stages must be treated slightly differently to prepare for imaging. It is discussed how to prepare samples for stages before the end of gastrulation (<10 hr postfertilization, option A), stages after gastrulation but before the onset of muscle twitching (∼16 hr post fertilization, option B), and stages after the onset of muscle twitching (>16 hr postfertilization up through early larval stages, option C).

(A) <10 hr postfertilization

(i) Transfer the embryos to a Petri dish that has been coated at the bottom with solidified 1%–2% agarose and filled with egg medium or 30x Danieau solution.

(ii) Using sharp forceps, remove the chorion from the embryos. CRITICAL STEP: To best remove the chorion without destroying the embryo at these early stages, it is best to tear an ever-widening hole from a single spot (using forceps in each hand) without coming near the embryo itself. Once the hole is wide enough, rotate the open chorion until the embryo drops out onto the surface of the agarose. Do not allow any part of the embryo to touch the water surface or else it will be destroyed by the surface tension.

(iii) If the embryos were prepared as in option A of step 13, staining by means of an exogenous dye may be desirable at this stage. Prepare a labeling chamber: coat the bottom of a small Petri dish with 1%–2% agarose and let it solidify. Dilute the desired dye to manufacturers specifications (if Bodipy TR methyl-ester or Bodipy FL C5 ceramide, the concentration should be ∼100 µM) in 30x Danieau solution or egg medium, and fill the labeling chamber with this solution. Carefully transfer the embryos to the labeing Petri dish using a glass transfer pipette, again not letting the embryos touch the water surface at any point. Stain the embryos for ∼1 hr before transferring them back into the large agarose-coated Petri dish filled with egg medium or 30x Danieau solution. Leave them in this solution for at least 10–15 min before the next step.

(iv) Add 1.5 mL 0.1% low melting point agarose in egg medium or 30x Danieau solution into one well of a 2-well coverslip chamber (#1 coverslip thickness).

(v) So that the embryos are not destroyed by the heat, let the agarose cool down within the chamber for ∼1–5 min or until no condensation forms on the side of the coverslip chamber, depending on how it was stored to keep from solidifying.

(vi) Using a glass transfer pipette, carefully transfer the embryos into the imaging chamber, ejecting as little medium as possible along with the embryos. Under a dissection microscope and using a hair loop (or a forceps, if you are careful), orient the embryos so that their animal pole is touching the surface of the coverslip or such that they are laterally mounted and sitting just above the surface of the coverslip. CAUTION: If the yolk cell touches the coverslip, the embryo may be damaged, which could interfere with proper development.

(vii) Let the agarose solidify around the embryos for ∼5 min before imaging.

(B) ∼10–16 hr postfertilization

(i) After bud stage, the embryos are much easier to manipulate without destroying them. Within a Petri dish filled with egg water, dechorionate the injected embryos with sharp forceps.

(ii) If an exogenous counterstain is desired, repeat step (iii) of option A, though this time much less volume is necessary. Just incubate the embryos within a 1.5 mL tube at 28^0C in dye solution for ∼1 hr. Wash the embryos several times in egg water. CRITICAL STEP: Regardless of the stage, once the embryos have been dechorionated, only transfer them to the various solutions using a glass transfer pipette. The embryos will stick to plastic transfer pipettes.

(iii) Add 1.5 mL 0.5%-1% low melting point agarose in 30x Danieau solution or egg medium into one well of a 2-well coverslip chamber (#1 coverslip thickness). Allow the agarose to cool as in step (v) of option A.

(iv) Using a glass transfer pipette, transfer the embryos into the imaging chamber, ejecting as little medium as possible along with the embryos. Under a dissection microscope and using forceps (or hair loop, if desired), orient the embryos in any desired orientation (e.g., dorsal or lateral).

(v) Let the agarose solidify around the embryos for ∼5 min before imaging.

(C) >16 hr postfertilization

(i) If imaging will be performed after 16 hr postfertilization, transfer the embryos to a Petri dish with egg water containing 1x PTU and replace this solution at least once daily to prevent significant pigment formation. CAUTION: PTU is a toxic chemical, so wear appropriate personal protective equipment (gloves, protective eyewear) and handle with caution.

(ii) Dechorionate injected embryos with sharp forceps. Avoid accidental trauma to the embryo as it twitches within the chorion.

(iii) If an exogenous counterstain is desired, repeat option B, step (iii), though make sure there is 1x PTU in the solution to prevent pigment formation during staining. Just incubate the embryos within a 1.5 mL Eppendorf tube at 28^0C in dye solution containing 1x PTU for ∼1 hr. Wash the embryos several times in egg water containing 1x PTU.

(iv) Anesthetize the zebrafish by transferring the embryos to a Petri dish with egg water containing 0.015% tricaine methanesulfonate along with 1x PTU.

(v) Add 1.5 mL 0.5%-1% low melting point agarose—with 0.015% tricaine methanesulfonate and 1x PTU—in 30x Danieau or egg medium solution into one well of a 2-well coverslip chamber (#1 coverslip thickness). Allow the agarose to cool as in step (v) of option A.

(vi) Using a glass transfer pipette, transfer the embryos into the imaging chamber, ejecting as little medium as possible along with the embryos. Under a dissection microscope and using a forceps (or hair loop, if desired), orient the embryos in any desired orientation (e.g., dorsal or lateral).

(vii) Let the agarose solidify around the embryos for ∼5 min before imaging.

A.2.4 Imaging SHG Nanoprobes within Living Zebrafish Embryos

23. Place the coverslip chamber on the stage of a confocal laser scanning microscope with 2P capabilities and a spectral scanning capability (e.g., "lambda mode" in the Zeiss Zen software).

24. Focus into the sample using the oculars of the microscope in visual mode using an objective of appropriate magnification and—preferably to maximize SHG signal collection—high numerical aperture ($\geq$0.8).

25. Prepare imaging settings for SHG signal collection, referred to as the SHG channel. Prepare the emission filter band as in step 20.

26. Depending on the counterstain used, prepare imaging settings for those particular dyes/fluorescent probes in a separate channel from the SHG collection. Note that a single channel may be used with the 2P laser alone in certain cases: many newer laser scanning microscopes allow direct selection of emission wavelength ranges (e.g., Zeiss QUASAR detectors), which is ideal for SHG imaging in conjunction with fluorescent markers, since the illuminating beam for SHG can be tuned to a particular wavelength (using a tunable 2P laser), allowing collection of two-photon fluorescence emission simultaneously with SHG signal in two separate detectors.

27. Using low power ($\sim$1% of maximum in the software), scan an optical section within the tissue using the SHG channel. Larger particle clusters should be saturated even at low power, whereas smaller clusters may require higher illuminating power, especially if the illuminating beam is off resonance (i.e. significantly red-shifted from 800 nm, in the case of BT).

28. Increase the power until the smallest SHG nanoprobe clusters are visible while ensuring that there is no phototoxicity to the tissue. Set up time-lapse imaging settings with sufficient time resolution so that each of the SHG nanoprobes can be tracked in time and space within the embryo. For example, during the gastrula period, cells are very dynamic, so a relatively short time (on the order of a few minutes) between frames will be necessary to track the SHG nanoprobes, assuming they are concentrated within the embryo.

29. If multiple imaging times are desired between different stages of development, the embryo may be removed from the agarose carefully with forceps and kept in a

28^{o}C incubator in egg water until the next imaging period. Note that during the larval stages of development and later, significant pigment formation can occur even in the presence of PTU. Spectral detection (e.g., with the lambda mode software) can be used to separate SHG signal from broad-band emission from different pigments within the fish. Additionally, fish without pigment (e.g., "Casper" zebrafish) may also be considered when designing an experiment using SHG nanoprobe labels.

Bibliography

[1] R. Weissleder. A clearer vision for in vivo imaging. *Nature Biotechnology*, 19(4):316–317, 2001.

[2] V. Ntziachristos. Going deeper than microscopy: The optical imaging frontier in biology. *Nature Methods*, 7(8):603–614, 2010.

[3] P. Sharma, S. Brown, G. Walter, S. Santra, and B. Moudgil. Nanoparticles for bioimaging. *Advances in Colloid and Interface Science*, 123:471–485, 2006.

[4] T. Ueno and T. Nagano. Fluorescent probes for sensing and imaging. *Nature Methods*, 8(8):642–645, 2011.

[5] S. Andersson-Engels, C. Klinteberg, K. Svanberg, and S. Svanberg. In vivo fluorescence imaging for tissue diagnostics. *Physics in Medicine and Biology*, 42:815, 1997.

[6] J. W. Lichtman and J. A. Conchello. Fluorescence microscopy. *Nature Methods*, 2(12):910–919, 2005.

[7] M. Y. Berezin and S. Achilefu. Fluorescence lifetime measurements and biological imaging. *Chemical Reviews*, 110(5):2641, 2010.

[8] J. Rao, A. Dragulescu-Andrasi, and H. Yao. Fluorescence imaging in vivo: recent advances. *Current Opinion in Biotechnology*, 18(1):17–25, 2007.

[9] J. V. Frangioni. In vivo near-infrared fluorescence imaging. *Current Opinion in Chemical Biology*, 7(5):626–634, 2003.

[10] Y. T. Lim, S. Kim, A. Nakayama, N. E. Stott, M. G. Bawendi, J. V. Frangioni, et al. Selection of quantum dot wavelengths for biomedical assays and imaging. *Molecular Imaging*, 2(1):50, 2003.

[11] F. Helmchen and W. Denk. Deep tissue two-photon microscopy. *Nature Methods*, 2(12):932–940, 2005.

[12] W.T. Mason. *Fluorescent and Luminescent Probes For Biological Activity: A Practical Guide to Technology for Quantitative Real-time Analysis*. Academic Pr, 1999.

[13] P. T. C. So, C. Y. Dong, B. R. Masters, and K. M. Berland. Two-photon excitation fluorescence microscopy. *Annual Review of Biomedical Engineering*, 2(1):399–429, 2000.

[14] U. Resch-Genger, M. Grabolle, S. Cavaliere-Jaricot, R. Nitschke, and T. Nann. Quantum dots versus organic dyes as fluorescent labels. *Nature Methods*, 5(9):763–775, 2008.

[15] J. K. Jaiswal and S. M. Simon. Potentials and pitfalls of fluorescent quantum dots for biological imaging. *Trends in Cell Biology*, 14(9):497–504, 2004.

[16] N. C. Shaner, P. A. Steinbach, and R. Y. Tsien. A guide to choosing fluorescent proteins. *Nature Methods*, 2(12):905–909, 2005.

[17] D. Shcherbo, I. I. Shemiakina, A. V. Ryabova, K. E. Luker, B. T. Schmidt, E. A. Souslova, T. V. Gorodnicheva, L. Strukova, K. M. Shidlovskiy, O. V. Britanova, et al. Near-infrared fluorescent proteins. *Nature Methods*, 7(10):827–829, 2010.

[18] G. S. Filonov, K. D. Piatkevich, L. M. Ting, J. Zhang, K. Kim, and V. V. Verkhusha. Bright and stable near-infrared fluorescent protein for in vivo imaging. *Nature Biotechnology*, 29(8):757–761, 2011.

[19] J.B. Pawley. *Handbook of biological confocal microscopy*. 1990.

[20] W. P. Dempsey, S. E. Fraser, and P. Pantazis. SHG nanoprobes: Advancing harmonic imaging in biology. *BioEssays*, 2012.

[21] P. Pantazis, J. Maloney, D. Wu, and S.E. Fraser. Second harmonic generating (SHG) nanoprobes for in vivo imaging. *Proceedings of the National Academy of Sciences*, 107(33):14535–14540, 2010.

[22] B. E. Cohen. Biological imaging: Beyond fluorescence. *Nature*, 467(7314):407–408, 2010.

[23] M. Bruchez Jr, M. Moronne, P. Gin, S. Weiss, and A. P. Alivisatos. Semiconductor nanocrystals as fluorescent biological labels. *Science*, 281(5385):2013–2016, 1998.

[24] T. Jamieson, R. Bakhshi, D. Petrova, R. Pocock, M. Imani, and A. M. Seifalian. Biological applications of quantum dots. *Biomaterials*, 28(31):4717–4732, 2007.

[25] C. Z. Hotz. Applications of quantum dots in biology. *NanoBiotechnology Protocols*, page 1, 2005.

[26] X. Michalet, F. F. Pinaud, L. A. Bentolila, J. M. Tsay, S. Doose, J. J. Li, G. Sundaresan, A. M. Wu, S. S. Gambhir, and S. Weiss. Quantum dots for live cells, in vivo imaging, and diagnostics. *Science*, 307(5709):538, 2005.

[27] P. Reiss, M. Protière, and L. Li. Core/shell semiconductor nanocrystals. *Small*, 5(2):154–168, 2009.

[28] X. Gao, L. Yang, J. A. Petros, F. F. Marshall, J. W. Simons, and S. Nie. In vivo molecular and cellular imaging with quantum dots. *Current Opinion in Biotechnology*, 16(1):63–72, 2005.

[29] J. K. Jaiswal, H. Mattoussi, J. M. Mauro, and S. M. Simon. Long-term multiple color imaging of live cells using quantum dot bioconjugates. *Nature Biotechnology*, 21(1):47–51, 2002.

[30] X. Wang, X. Ren, K. Kahen, M. A. Hahn, M. Rajeswaran, S. Maccagnano-Zacher, J. Silcox, G. E. Cragg, A. L. Efros, and T. D. Krauss. Non-blinking semiconductor nanocrystals. *Nature*, 459(7247):686–689, 2009.

[31] J. A. J. Fitzpatrick, S. K. Andreko, L. A. Ernst, A. S. Waggoner, B. Ballou, and M. P. Bruchez. Long-term persistence and spectral blue shifting of quantum dots in vivo. *Nano Letters*, 9(7):2736–2741, 2009.

[32] H. M. Xiong. Photoluminescent ZnO nanoparticles modified by polymers. *Journal of Materials Chemistry*, 20(21):4251–4262, 2010.

[33] H. S. Choi, W. Liu, P. Misra, E. Tanaka, J. P. Zimmer, B. I. Ipe, M. G. Bawendi, and J. V. Frangioni. Renal clearance of quantum dots. *Nature Biotechnology*, 25(10):1165–1170, 2007.

[34] B. R. Masters and P. T. C. So. *Handbook of biomedical nonlinear optical microscopy*. Oxford University Press, USA, 2008.

[35] P. A. Franken, A. E. Hill, C. W. Peters, and G. Weinreich. Generation of optical harmonics. *Physical Review Letters*, 7(4):118–119, 1961.

[36] I. Freund, M. Deutsch, and A. Sprecher. Connective tissue polarity: Optical second-harmonic microscopy, crossed-beam summation, and small-angle scattering in rat-tail tendon. *Biophysical Journal*, 50(4):693–712, 1986.

[37] P. J. Campagnola, L. M. Loew, et al. Second-harmonic imaging microscopy for visualizing biomolecular arrays in cells, tissues and organisms. *Nature Biotechnology*, 21(11):1356–1360, 2003.

[38] C. L. Hsieh, R. Grange, Y. Pu, and D. Psaltis. Bioconjugation of barium titanate nanocrystals with immunoglobulin G antibody for second harmonic radiation imaging probes. *Biomaterials*, 31(8):2272–2277, 2010.

[39] A. V. Kachynski, A. N. Kuzmin, M. Nyk, I. Roy, and P. N. Prasad. Zinc oxide nanocrystals for nonresonant nonlinear optical microscopy in biology and medicine. *The Journal of Physical Chemistry C*, 112(29):10721–10724, 2008.

[40] Y. Pu, R. Grange, C. L. Hsieh, and D. Psaltis. Nonlinear optical properties of core-shell nanocavities for enhanced second-harmonic generation. *Physical Review Letters*, 104(20):207402, 2010.

[41] A. E. Nel, L. Mädler, D. Velegol, T. Xia, E. M. V. Hoek, P. Somasundaran, F. Klaessig, V. Castranova, and M. Thompson. Understanding biophysicochemical interactions at the nano–bio interface. *Nature Materials*, 8(7):543–557, 2009.

[42] J. Joo, S. G. Kwon, J. H. Yu, and T. Hyeon. Synthesis of ZnO Nanocrystals with Cone, Hexagonal Cone, and Rod Shapes via Non-Hydrolytic Ester Elimination Sol–Gel Reactions. *Advanced Materials*, 17(15):1873–1877, 2005.

[43] X. Ji, D. Copenhaver, C. Sichmeller, and X. Peng. Ligand bonding and dynamics on colloidal nanocrystals at room temperature: The case of alkylamines on CdSe nanocrystals. *Journal of the American Chemical Society*, 130(17):5726–5735, 2008.

[44] R. A. Sperling and W. J. Parak. Surface modification, functionalization and bioconjugation of colloidal inorganic nanoparticles. *Philosophical Transactions of the Royal Society A: Mathematical, Physical and Engineering Sciences*, 368(1915):1333–1383, 2010.

[45] T. Sakura, T. Takahashi, K. Kataoka, and Y. Nagasaki. One-pot preparation of mono-dispersed and physiologically stabilized gold colloid. *Colloid & Polymer Science*, 284(1):97–101, 2005.

[46] H. M. Zareie, C. Boyer, V. Bulmus, E. Nateghi, and T. P. Davis. Temperature-responsive self-assembled monolayers of oligo (ethylene glycol): Control of biomolecular recognition. *Acs Nano*, 2(4):757–765, 2008.

[47] J. Suh, K. L. Choy, S. K. Lai, J. S. Suk, B. C. Tang, S. Prabhu, and J. Hanes. PEGylation of nanoparticles improves their cytoplasmic transport. *International Journal of Nanomedicine*, 2(4):735, 2007.

[48] G. T. Hermanson. *Bioconjugate techniques*. Academic Press, 1996.

[49] Gelest. Silicon Compounds: Silanes and Silicones, 2004.

[50] J. Nicholas, J. A. Prescher, and C. R. Bertozzi. A strain-promoted [3+ 2] azide-alkyne cycloaddition for covalent modification of biomolecules in living systems. *Journal of the American Chemical Society*, 126(46):15046–15047, 2004.

[51] C. H. J. Choi, C. A. Alabi, P. Webster, and M. E. Davis. Mechanism of active targeting in solid tumors with transferrin-containing gold nanoparticles. *Proceedings of the National Academy of Sciences*, 107(3):1235–1240, 2010.

[52] K. Sampath. *Live Imaging in Zebrafish: Insights Into Development and Disease*. World Scientific Publishing Corporation Inc., 2010.

[53] R. W. Boyd. *Nonlinear optics*. Academic Press, 2003.

[54] R. L. Sutherland, D. G. McLean, and S. Kirkpatrick. *Handbook of nonlinear optics*, volume 82. CRC press, 2003.

[55] P. Kim, S. C. Jones, P. J. Hotchkiss, J. N. Haddock, B. Kippelen, S. R. Marder, and J. W. Perry. Phosphonic Acid-Modified Barium Titanate Polymer Nanocomposites with High Permittivity and Dielectric Strength. *Advanced Materials*, 19(7):1001–1005, 2007.

[56] M. Iijima, N. Sato, M. Tsukada, and H. Kamiya. Dispersion behavior of barium titanate nanoparticles prepared by using various polycarboxylic dispersants. *Journal of the American Ceramic Society*, 90(9):2741–2746, 2007.

[57] G. Ciofani, S. Danti, D. D'Alessandro, S. Moscato, M. Petrini, and A. Menciassi. Barium titanate nanoparticles: Highly cytocompatible dispersions in glycol-

chitosan and doxorubicin complexes for cancer therapy. *Nanoscale Research Letters*, 5(7):1093–1101, 2010.

[58] T. Schroeder. Long-term single-cell imaging of mammalian stem cells. *Nature Methods*, 8(4s):S30–S35, 2011.

[59] M. E. Buckingham and S. M. Meilhac. Tracing Cells for Tracking Cell Lineage and Clonal Behavior. *Developmental Cell*, 21(3):394–409, 2011.

[60] J. K. Jaiswal, E. R. Goldman, H. Mattoussi, S. M. Simon, et al. Use of quantum dots for live cell imaging. *Nature Methods*, 1(1):73–78, 2004.

[61] S. J. Chang, W. S. Liao, C. J. Ciou, J. T. Lee, and C. C. Li. An efficient approach to derive hydroxyl groups on the surface of barium titanate nanoparticles to improve its chemical modification ability. *Journal Of Colloid And Interface Science*, 329(2):300–305, 2009.

[62] Y. V. Kolen'ko, K. A. Kovnir, I. S. Neira, T. Taniguchi, T. Ishigaki, T. Watanabe, N. Sakamoto, and M. Yoshimura. A novel, controlled, and high-yield solvothermal drying route to nanosized barium titanate powders. *The Journal of Physical Chemistry C*, 111(20):7306–7318, 2007.

[63] B. Arkles, Y. Pan, G. L. Larson, D. H. Berry, and K. L. Mittal. Cyclic azasilanes: Volatile coupling agents for nanotechnology. *Silanes and Other Coupling Agents*, 3:179r191, 2004.

[64] K. S. Mazdiyasni, R. T. Dolloff, and J. S. Smith II. Preparation of High-Purity Submicron Barium Titanate Powders. *Journal of the American Ceramic Society*, 52(10):523–526, 1969.

[65] J. T. Last. Infrared-absorption studies on barium titanate and related materials. *Physical Review*, 105(6):1740, 1957.

[66] P. J. Launer. Infrared analysis of organosilicon compounds: spectra-structure correlations. *Silicone Compounds Register and Review, Edited by B. Arkles, et al.*, page 100, 1987.

[67] A. S. Karakoti, S. Das, S. Thevuthasan, and S. Seal. PEGylated inorganic nanoparticles. *Angewandte Chemie International Edition*, 50(9):1980–1994, 2011.

[68] J. J. Weaver. *Corroles*. PhD thesis, California Institute of Technology, 2005.

[69] A. Mahammed, I. Goldberg, and Z. Gross. Highly selective chlorosulfonation of tris (pentafluorophenyl) corrole as a synthetic tool for the preparation of amphiphilic corroles and metal complexes of planar chirality. *Organic Letters*, 3(22):3443–3446, 2001.

[70] S. P. Chambers, L. V. B. Anderson, G. M. Maguire, A. Dodd, and D. R. Love. Sarcoglycans of the zebrafish: Orthology and localization to the sarcolemma and myosepta of muscle. *Biochemical and Biophysical Research Communications*, 303(2):488–495, 2003.

[71] C. B. Kimmel, W. W. Ballard, S. R. Kimmel, B. Ullmann, and T. F. Schilling. Stages of embryonic development of the zebrafish. *Developmental Dynamics*, 203(3):253–310, 1995.

[72] L. Caneparo, P. Pantazis, W. Dempsey, and S. E. Fraser. Intercellular Bridges in Vertebrate Gastrulation. *PLoS One*, 6(5):e20230, 2011.

[73] K. Kawakami and A. Shima. Identification of the Tol2 transposase of the medaka fish Oryzias latipes that catalyzes excision of a nonautonomous Tol2 element in zebrafish Danio rerio. *Gene*, 240(1):239–244, 1999.

[74] A. Hopt and E. Neher. Highly nonlinear photodamage in two-photon fluorescence microscopy. *Biophysical Journal*, 80(4):2029–2036, 2001.

[75] E. A. Bayer and M. Wilchek. Application of avidin–biotin technology to affinity-based separations. *Journal of Chromatography A*, 510:3–11, 1990.

[76] E. P. Diamandis and T. K. Christopoulos. The biotin-(strept) avidin system: Principles and applications in biotechnology. *Clinical Chemistry*, 37(5):625–636, 1991.

[77] T. Ould-Ely, M. Luger, L. Kaplan-Reinig, K. Niesz, M. Doherty, and D. E. Morse. Large-scale engineered synthesis of BaTiO3 nanoparticles using low-temperature bioinspired principles. *Nature Protocols*, 6(1):97–104, 2011.

[78] D. Staedler, T. Magouroux, R. Hadji, C. Joulaud, J. Extermann, S. Schwung, S. Passemard, C. Kasparian, G. Clarke, M. Gerrmann, et al. Harmonic Nanocrystals for Bio-Labeling: A Survey of Optical Properties and Biocompatibility. *ACS Nano*, 2012.

[79] Z. L. Wang. Zinc oxide nanostructures: Growth, properties and applications. *Journal of Physics: Condensed Matter*, 16:R829, 2004.

[80] I. Gonzalez-Valls and M. Lira-Cantu. Vertically-aligned nanostructures of ZnO for excitonic solar cells: a review. *Energy and Environmental Science*, 2(1):19–34, 2008.

[81] S. A. Kumar and S. M. Chen. Nanostructured zinc oxide particles in chemically modified electrodes for biosensor applications. *Analytical Letters*, 41(2):141–158, 2008.

[82] D. Beydoun, R. Amal, G. Low, and S. McEvoy. Role of nanoparticles in photocatalysis. *Journal of Nanoparticle Research*, 1(4):439–458, 1999.

[83] K. Schilling, B. Bradford, D. Castelli, E. Dufour, J. F. Nash, W. Pape, S. Schulte, I. Tooley, J. Van Den Bosch, and F. Schellauf. Human safety review of "nano" titanium dioxide and zinc oxide. *Photochemical and Photobiological Sciences*, 9(4):495–509, 2010.

[84] A. Becheri, M. Dürr, P. Lo Nostro, and P. Baglioni. Synthesis and characterization of zinc oxide nanoparticles: Application to textiles as UV-absorbers. *Journal oOf Nanoparticle Research*, 10(4):679–689, 2008.

[85] A. V. Zvyagin, X. Zhao, A. Gierden, W. Sanchez, J. A. Ross, and M. S. Roberts. Imaging of zinc oxide nanoparticle penetration in human skin in vitro and in vivo. *Journal of Biomedical Optics*, 13:064031, 2008.

[86] A.B. Djurišić and Y.H. Leung. Optical properties of ZnO nanostructures. *Small*, 2(8-9):944–961, 2006.

[87] H. M. Xiong, Y. Xu, Q. G. Ren, and Y. Y. Xia. Stable Aqueous ZnO@ Polymer Core-Shell Nanoparticles with Tunable Photoluminescence and Their Application in Cell Imaging. *Journal of the American Chemical Society*, 130(24):7522–7523, 2008.

[88] L. Spanhel and M. A. Anderson. Semiconductor clusters in the sol-gel process: Quantized aggregation, gelation, and crystal growth in concentrated zinc oxide colloids. *Journal of the American Chemical Society*, 113(8):2826–2833, 1991.

[89] E.A. Meulenkamp. Synthesis and growth of ZnO nanoparticles. *The Journal of Physical Chemistry B*, 102(29):5566–5572, 1998.

[90] Z. Hu, G. Oskam, and P.C. Searson. Influence of solvent on the growth of ZnO nanoparticles. *Journal of colloid and interface science*, 263(2):454–460, 2003.

[91] R. Viswanatha, S. Sapra, B. Satpati, P. V. Satyam, B. N. Dev, and D. D. Sarma. Understanding the quantum size effects in ZnO nanocrystals. *Journal of Materials Chemistry*, 14(4):661–668, 2004.

[92] A. N. Tsvigunov. A new modification of zinc oxide synthesized by the hydrothermal method. *Glass and Ceramics*, 58(7):280–282, 2001.

[93] S. Sepulveda-Guzman, B. Reeja-Jayan, E. de la Rosa, A. Torres-Castro, V. Gonzalez-Gonzalez, and M. Jose-Yacaman. Synthesis of assembled ZnO

structures by precipitation method in aqueous media. *Materials Chemistry and Physics*, 115(1):172–178, 2009.

[94] J. J. Richardson and F. F. Lange. Controlling low temperature aqueous synthesis of ZnO. 1. Thermodynamic analysis. *Crystal Growth and Design*, 9(6):2570–2575, 2009.

[95] X. Hu, J. Gong, L. Zhang, and J. C. Yu. Continuous Size Tuning of Monodisperse ZnO Colloidal Nanocrystal Clusters by a Microwave-Polyol Process and Their Application for Humidity Sensing. *Advanced Materials*, 20(24):4845–4850, 2008.

[96] I. Bilecka, I. Djerdj, and M. Niederberger. One-minute synthesis of crystalline binary and ternary metal oxide nanoparticles. *Chemical Communications*, (7):886–888, 2008.

[97] S. T. Tan, B. J. Chen, X. W. Sun, W. J. Fan, H. S. Kwok, X. H. Zhang, and S. J. Chua. Blueshift of optical band gap in ZnO thin films grown by metal-organic chemical-vapor deposition. *Journal of Applied Physics*, 98:013505, 2005.

[98] Z. Siqingaowa and H. Yao. Preparation and characterization of nanocrystalline ZnO by direct precipitation method. *Frontiers of Chemistry in China*, 1(3):277–280, 2006.

[99] M. L. Kahn, M. Monge, V. Collière, F. Senocq, A. Maisonnat, and B. Chaudret. Size-and Shape-Control of Crystalline Zinc Oxide Nanoparticles: A New Organometallic Synthetic Method. *Advanced Functional Materials*, 15(3):458–468, 2005.

[100] J. Tang, X. Cui, Y. Liu, and X. Yang. Morphology-controlled synthesis of monodisperse ZnO troughs at the Air-water interface under mild conditions. *The Journal of Physical Chemistry B*, 109(47):22244–22249, 2005.

[101] S. K. N. Ayudhya, P. Tonto, O. Mekasuwandumrong, V. Pavarajarn, and P. Praserthdam. Solvothermal synthesis of ZnO with various aspect ratios using organic solvents. *Crystal growth & design*, 6(11):2446–2450, 2006.

[102] I. M. Lifshitz and V. V. Slyozov. The kinetics of precipitation from supersaturated solid solutions. *Journal of Physics and Chemistry of Solids*, 19(1):35–50, 1961.

[103] C. Wagner. Theorie der Alterung von Niederschlägen durch Umlösen (Ostwald-Reifung). *Zeitschrift für Elektrochemie, Berichte der Bunsengesellschaft für physikalische Chemie*, 65(7-8):581–591, 1961.

[104] E. M. Wong, P. G. Hoertz, C. J. Liang, B. M. Shi, G. J. Meyer, and P. C. Searson. Influence of organic capping ligands on the growth kinetics of ZnO nanoparticles. *Langmuir*, 17(26):8362–8367, 2001.

[105] S. Li, S. Meierott, and J. M. Köhler. Effect of water content on growth and optical properties of ZnO nanoparticles generated in binary solvent mixtures by micro-continuous flow synthesis. *Chemical Engineering Journal*, 165(3):958–965, 2010.

[106] A. S. Ratkovich and R. L. Penn. Controlling nanosized ZnO growth kinetics using various Zn: OH concentration ratios. *The Journal of Physical Chemistry C*, 111(38):14098–14104, 2007.

[107] Z. Hu, G. Oskam, R. L. Penn, N. Pesika, and P. C. Searson. The influence of anion on the coarsening kinetics of ZnO nanoparticles. *The Journal of Physical Chemistry B*, 107(14):3124–3130, 2003.

[108] X. Tang, E. S. G. Choo, L. Li, J. Ding, and J. Xue. One-pot synthesis of water-stable ZnO nanoparticles via a polyol hydrolysis route and their cell labeling applications. *Langmuir*, 25(9):5271–5275, 2009.

[109] Y. S. Fu, X. W. Du, S. A. Kulinich, J. S. Qiu, W. J. Qin, R. Li, J. Sun, and J. Liu. Stable aqueous dispersion of ZnO quantum dots with strong blue

emission via simple solution route. *Journal of the American Chemical Society*, 129(51):16029–16033, 2007.

[110] L. Chen, J. Xu, J. D. Holmes, and M. A. Morris. A facile route to ZnO nanoparticle superlattices: synthesis, functionalization, and self-assembly. *The Journal of Physical Chemistry C*, 114(5):2003–2011, 2010.

[111] H. M. Xiong, Z. D. Wang, D. P. Liu, J. S. Chen, Y. G. Wang, and Y. Y. Xia. Bonding polyether onto ZnO nanoparticles: An effective method for preparing polymer nanocomposites with tunable luminescence and stable conductivity. *Advanced Functional Materials*, 15(11):1751–1756, 2005.

[112] H. M. Xiong, D. P. Xie, X. Y. Guan, Y. J. Tan, and Y. Y. Xia. Water-stable blue-emitting ZnO@ polymer core–shell microspheres. *Journal of Materials Chemistry*, 17(24):2490–2496, 2007.

[113] R. N. Spitz, J. E. Barton, M. A. Barteau, R. H. Staley, and A. W. Sleight. Characterization of the surface acid-base properties of metal oxides by titration/displacement reactions. *The Journal of Physical Chemistry*, 90(17):4067–4075, 1986.

[114] M. Y. Ge, H. P. Wu, L. Niu, J. F. Liu, S. Y. Chen, P. Y. Shen, Y. W. Zeng, Y. W. Wang, G. Q. Zhang, and J. Z. Jiang. Nanostructured ZnO: From monodisperse nanoparticles to nanorods. *Journal of Crystal Growth*, 305(1):162–166, 2007.

[115] R. Hong, T. Pan, J. Qian, and H. Li. Synthesis and surface modification of ZnO nanoparticles. *Chemical Engineering Journal*, 119(2):71–81, 2006.

[116] H. M. Xiong, Z. D. Wang, and Y. Y. Xia. Polymerization Initiated by Inherent Free Radicals on Nanoparticle Surfaces: A Simple Method of Obtaining Ultrastable (ZnO) Polymer Core–Shell Nanoparticles with Strong Blue Fluorescence. *Advanced Materials*, 18(6):748–751, 2006.

[117] H. M. Xiong, D. P. Liu, Y. Y. Xia, and J. S. Chen. Polyether-grafted ZnO nanoparticles with tunable and stable photoluminescence at room temperature. *Chemistry of Materials*, 17(12):3062–3064, 2005.

[118] M. Ishifuji, M. Mitsuishi, and T. Miyashita. Bottom-up design of hybrid polymer nanoassemblies elucidates plasmon-enhanced second harmonic generation from nonlinear optical dyes. *Journal of the American Chemical Society*, 131(12):4418–4424, 2009.